TECHNISCHE UNIVERSITÄT MÜNCHEN

Lehrstuhl für Aerodynamik und Strömungsmechanik

Numerical Prediction of Erosion and Degassing Effects in Cavitating Flows

Michael Simon Mihatsch

Vollständiger Abdruck der von der Fakultät für Maschinenwesen der Technischen Universität München zur Erlangung des akademischen Grades eines

Doktor-Ingenieurs

genehmigten Dissertation.

Vorsitzender:		Prof. Dr.-Ing. Steffen Marburg
Prüfer der Dissertation:	1.	Prof. Dr.-Ing. Nikolaus A. Adams
	2.	Prof. Manolis Gavaises, Ph.D.

Die Dissertation wurde am 20.06.2016 bei der Technischen Universität München eingereicht und durch die Fakultät für Maschinenwesen am 05.02.2017 angenommen.

Michael Mihatsch
Schmied-Kochel-Straße 2
81371 München
Germany

m.s.mihatsch@gmx.de

Released June 2016

Acknowledgments

The following work was written during my time as a research assistant at the Institute of Aerodynamics and Fluid Mechanics of the Technische Universität München. I would like to thank a number of special people without whose contributions and support this work would never have found completion.

First, I want to thank my supervisor, Prof. Dr. Nikolaus Adams, for giving me the opportunity to undertake this work. He provided a working environment that facilitated individual creativity and encouraged undertaking new unconventional approaches, some of which are found in this thesis.

I would like to thank Prof. Manolis Gavaises for accepting the position as second examiner, which he took on at very short notice.

Prof. Dr. Steffen Marburg accepted the position of chairman of the doctoral examination board and handled all the administrative tasks, for which I am thankful.

At the institute I was part of the research group on gasdynamics, and the nucleus of this group deserves special mention: Steffen – supersonic – Schmidt, Marcus – Gigl – Giglmaier, Freddy – Gefahr, Kuchenparadies – Quaatz, Christian – Cgerer – Egerer, and Matthias – Matze – Thalhamer, all of which were part of the infamous “Büüro”. Throughout my thesis, additional valuable members joined our group, namely Felix Örley, Bernd Budich, Bruno Beban, and Theresa Trummler. There are many things that will remain in my memory: the intense discussions (work related as well as on any other miscellaneous topic), memorable nights at the “Italiener” and later at the “Grieche” (for those who managed to remember them the next day) and traveling to places all over the world. Of course, this list is far from comprehensive and out of necessity (and discretion) leaves out many of our more daring highlights (jet engine). Thank you all for making my time at the institute unique and memorable.

Not limited to this period of my life, my parents have always been a safe haven. Even if their help was only asked for on occasion, their support was always felt to be present and reassuring.

This last paragraph is reserved for a very special person, who endured everything connected to this thesis (including my English spelling and grammar) with patience and never lost faith in me. Johanna – Maus – Schneider, thank you for all your love, support, and motivation.

Abstract

Hydrodynamic cavitation and cavitation erosion are well-known phenomena in many engineering applications. Distinctive examples include marine propulsion and fuel injection devices. The basic mechanisms of hydrodynamic cavitation are flow-induced evaporation due to the pressure drop of an accelerated liquid, and inertia controlled recondensation of liquid-embedded vapor bubbles due to pressure recovery. Cavitation erosion is the consequence of repeated collapse-induced high pressure loads on a material surface. Focus of this thesis is to provide a framework for quantitative erosion prediction via numerical simulation. For flow simulation a density-based finite volume method, which takes into account the compressibility of both phases, and resolves collapse-induced pressure waves is employed.

In a first step the prediction of impact load spectra of cavitating flows, i.e., the rate and intensity distribution of collapse events, is assessed based on a detailed analysis of flow dynamics. As reference configuration we consider the collapse of a vapor cloud in the vicinity of a solid wall and the expansion of a liquid into a radially divergent gap which exhibits unsteady sheet and cloud cavitation. Analysis of simulation data shows that global cavitation dynamics and dominant flow events are well resolved, even if the spatial resolution is too coarse to resolve individual vapor bubbles. The inviscid flow model recovers increasingly fine-scale vapor structures and higher collapse rates with increasing resolution. Frequency and intensity of these collapse events scale with grid resolution. Scaling laws based on two reference lengths are introduced for this purpose. Upon applying these laws impact load spectra recorded on experimental and numerical pressure sensors agree with each other. Furthermore, correlation between experimental pitting rates and collapse-event rates is found. The main finding is that impact load spectra of cavitating flows can be inferred from flow data that captures the main vapor structures and wave dynamics without the need to resolve all flow scales.

In a next step, a model is presented to derive incubation times, i.e., the time solid material can withstand the erosive potential of a cavitating flow until first damage, from numerically determined impact load spectra. The model predicts reasonable incubation times for a variation of different materials and different operating conditions.

Free gas can dampen the collapse of vapor structures and influence inherent dynamics of hydrodynamic cavitation. Interaction of cavitation and free gas content is investigated in the final part of the work. Focus of interest lies on the ability of a cavitating flow to release solved gas form a liquid. For the investigated nozzle flows this interaction is dominated by diffusion, which is promoted by large interfacial areas between fluid phase and vapor-gas mixtures.

Publications

The work of the author was continuously published and presented at scientific meetings. The author contributed to the following journal publications:

- M. S. Mihatsch, S. J. Schmidt, N. A. Adams, "Cavitation Erosion Prediction based on Analysis of Flow Dynamics and Impact Load Spectra," Physics of Fluids, 2015.
- Örley F., Trummler T., Hickel, S., Mihatsch M. S., Schmidt S. J., Adams N. A., "Large-eddy simulation of cavitating nozzle flow and primary jet break-up," Physics of Fluids, 2015.

The author contributed to the following book chapters:

- M. S. Mihatsch, S. J. Schmidt, M. Thalhamer, and N. A. Adams, "Numerical Prediction of Erosive Collapse Events in Unsteady Compressible Cavitating Flows", in: Marine 2011, IV International Conference on Computational Methods in Marine Engineering - Selected Papers, Springer, 2013.
- Adams, Nikolaus A. and Steffen J. Schmidt. "Shocks in cavitating flows." In: Bubble Dynamics and Shock Waves. Springer, 2013. 235-256.
- S. J. Schmidt, M. S. Mihatsch, M. Thalhamer and N. A. Adams (2014). "Assessment of erosion sensitive areas via compressible simulation of unsteady cavitating flows." In: Advanced Experimental and Numerical Techniques for Cavitation Erosion Prediction, Springer, 2014. 329-344.

The author contributed to work which has been presented at the following conferences with conference proceedings:

- M. S. Mihatsch, S. J. Schmidt, M. Thalhamer, and N. A. Adams, "Collapse Detection in Compressible 3-D Cavitating Flows and Assessment of Erosion Criteria," WIMRC 3rd International Cavitation Forum 2011, Warwick 2011.
- S. J. Schmidt , M. S. Mihatsch, M. Thalhamer, and N. A. Adams, "Assessment of the Prediction Capability of a Thermodynamic Cavitation Model for the Collapse Characteristics of a Vapor-Bubble Cloud," WIMRC 3rd International Cavitation Forum 2011, Warwick 2011.
- R. Skoda, U. Iben, A. Morozov, M. S. Mihatsch, S. J. Schmidt, and N. A. Adams, "Numerical simulation of collapse induced shock dynamics for prediction of the geometry, pressure, and temperature impact on the cavitation erosion in micro channels," WIMRC 3rd International Cavitation Forum 2011, Warwick 2011.

- S. Hickel, M. S. Mihatsch and S. J. Schmidt, “Implicit Large Eddy Simulation of Cavitation in Micro Channel Flows,” WIMRC 3rd International Cavitation Forum 2011, Warwick 2011.
- M. S. Mihatsch, S. J. Schmidt, M. Thalhamer, and N. A. Adams, “Numerical Prediction of Erosive Collapse Events in Unsteady Compressible Cavitating Flows,” IV International Conference on Computational Methods in Marine Engineering, Lisbon 2011.
- M. Thalhamer, S.J. Schmidt, M. Mihatsch, N.A. Adams, “Numerical Simulation of Sheet and Cloud Cavitation and Detection of Cavitation Erosion,” 14th International Symposium on Transport Phenomena and Dynamics of Rotating Machinery, ISROMAC-14, Honolulu 2012.
- M. S. Mihatsch, S. J. Schmidt, M. Thalhamer, and N. A. Adams, “Quantitative Prediction of Erosion Aggressiveness through Numerical Simulation of 3-D Unsteady Cavitating Flows,” 8th International Symposium on Cavitation, Singapore 2012.
- Örley Felix, Trummler Theresa, Hickel Stefan, Mihatsch Michael S., Schmidt Steffen J., and Adams Nikolaus A.,“ LES of Cavitating Nozzle and Jet Flows,” Direct and Large-Eddy Simulation X, ERCOFTAC Workshop DLES 10, Limassol, Cyprus, 2015.

The author contributed to work which has been presented at the following conferences with oral presentation only:

- M. S. Mihatsch, M. Thalhamer, S. J. Schmidt and N. A. Adams, “Numerical Prediction of Erosive Collapse Events in Unsteady Compressible Cavitating Flows”, Jahrestreffen der Fachgruppen Computational Fluid Dynamics und Fluidverfahrenstechnik, Weimar 2012.
- M. S. Mihatsch , S. J. Schmidt, N. A. Adams, “Estimation of Incubation Times through Numerical Simulation of 3-D Unsteady Cavitating Flows,” SHF Conference Hydraulic Machines and Cavitation /Air in Water Pipes, Grenoble 2013.
- Michael S. Mihatsch, Steffen J. Schmidt and Nikolaus A. Adams, „Estimation of incubation times through numerical simulation of 3-D unsteady cavitating flows,” 11th. World Congress on Computational Mechanics (WCCM XI), Barcelona 2014.

Ideas and results of the author published in these publications are included in parts or in an extended version in this thesis.

Table of Content

1 Introduction

1.1 Background and Motivation

Cavitation is defined as the generation of vapor within a liquid due to a drop of the static pressure below vapor pressure.[1,2] In hydrodynamic cavitation, pressure-drops often are caused by a local acceleration of the flow, for example by the contraction of a nozzle[2], the curvature of a hydrofoil[2-4], or the presence of vortical structures[5], such as the tip-vortex of a propeller blade, or vortices generated by a turbulent shear layer[6,7]. Evaporation is usually followed by recondensation, when vapor structures are advected into areas of higher static pressure. Collapse of vapor regions results in shock waves, which can trigger vibration modes of structures.[4] In the vicinity of solid boundaries, the collapse of vapor structures often leads to severe damage of surface material.[1-4] The ability of a cavitating flow to cause material damage can be described as 'erosive potential' of the flow.[2] In most cases, actual damage is not caused by a single collapse, but is the result of repeated impacts. Several studies suggest that the erosive potential can be specified by (so-called) impact load spectra, which contain information about intensity and temporal rate of collapse-induced loads.[8-10] In hydrodynamic cavitation, factors affecting collapse intensity and mechanisms controlling collapse rates are related. The intensity of a single collapse event has been the subject of numerous studies (e.g. Refs. 11-13). For a given fluid, the intensity mainly depends on the volume of condensing vapor, the position relative to boundaries or to other vapor structures, and the motion and the pressure in the ambient liquid. The rate of collapse events in sheet and cloud cavitation, for example, is affected by characteristic bulk velocity, pressure level, and intrinsic dynamics.

While experiments can provide information about position and progress of erosion damage, they do not necessarily relate erosion and flow dynamics. This is, however, necessary to prevent erosion. Here, Computational Fluid Dynamics (CFD) is an important tool for providing detailed flow information. For the prediction of the erosive potential of a cavitating flow by numerical simulation, occurrence and extent of vapor regions, cavitation dynamics, and characteristic frequencies have to be captured. Moreover, the simulation has to resolve collapse-induced loads and the resulting impact load spectrum. Several incompressible approaches have been applied for predicting cavitating flows. Bensow *et al.*[14,15] reproduced the shedding mechanism of a cavity on a NACA 15 hydrofoil and the typical cavitation behavior on a rotating ship propeller (sheet- and root-cavitation, tip vortex cavitation), by using large-eddy simulation (LES) along with a homogeneous mixture model and finite-rate mass transfer terms. Yakubov *et al.*[16] applied a RANS approach and an Euler-Lagrange cavitation model to consider water quality effects through the tracking of nuclei, which can have a considerable impact for example on cavitation inception. Andriotis *et al.*[17] and Giannadakis e*t al.*[18] also used a RANS approach with an Euler-Lagrange cavitation model, accounting for a variety of physical effects including breakup and coalescence of bubbles, to predict characteristic cavitation structures in diesel injection nozzles.

For capturing collapse-induced shock formation, compressibility is essential. Taking the compressibility of both phases into account, Schmidt *et al.*[19] developed an explicit, density-based method for the simulation of cavitating flows. The approach employs an inviscid formulation, a homogeneous mixture model with equilibrium phase change, and resolves wave dynamics. The method has been successfully applied to a collapsing bubble and cavitation dynamics on hydrofoils.[20,21]

Numerical prediction of cavitation erosion still remains a challenging task. By monitoring the maximum pressures recorded on solid boundaries during the (compressible and time resolved) simulation, Schmidt *et al.*[22] showed good agreement for the area of predicted erosion damage. Other approaches propose physically motivated erosion criteria (e.g. condensation rate) that are evaluated either through their maximum values,[23,24] mean values,[25] or the percentage of the simulation time during which predefined thresholds are exceeded.[23] While the first method focuses on the importance of the strongest events, the latter quantifies the loading of the material mainly by the temporal duration of a pulse, not taking into account the amplitude. Additionally, definition of limiting thresholds can be case-dependent and is mostly not straight forward.[23] Information generated by the above mentioned approaches is limited to a spatially resolved scalar, representing an 'erosion intensity', which can be used for relative comparison of erosion risk. No information characterizing the frequency and intensity distribution of loads is obtained by any of the methods.

Technical liquids contain gas, either solved, or free in the form of micro bubbles. Tinguely *et al.*[12] showed that the collapse energy of a single spherical bubble is distributed between emission of a shock wave and rebound of the bubble depending on the gas content. Kjeldsen *et al.*[26] demonstrated that dynamic behavior similar to a cavitating flow could be generated by adding air to a liquid flow. The authors reported, however, that governing frequencies changed compared to the cavitating flow field. Ventilated cavities, i.e., injecting non-condensable gas into a vapor cavity, has been used to suppress dynamics of sheet cavitation in spillways of dams in order to prevent erosion.[1,2]

Above findings show that free gas content can influence global dynamics and collapse characteristics, which both characterize the erosive potential of a flow. In numerous experimental investigations the gas content is carefully controlled by degassing the liquid or by seeding specific gas concentrations into the flow, see, e.g., Refs. 27,28. In many technical applications, however, gas content can not be controlled and may change during operation. Examples are sea water at different temperatures or fuel quality, which may vary strongly over the life cycle of a combustion engine. The effect of gas content on cavitating flows should thus be considered carefully. Battistoni *et al.*[29] investigated the influence of free gas on the cavitating flow through a micro nozzle by numerical simulation. The mass fraction of gas was kept constant during each simulation and effects of release of gas from the liquid or absorption of gas into the liquid were not modelled. Iben *et al.*[30] demonstrated that cavitation in a nozzle can lead to the release of solved gas and thus strongly enhances the content of free gas. For a different nozzle geometry, these findings were confirmed by Freudigmann *et al.*[31]. Therefore, interaction of

cavitation and gas content has to be included in the numerical model to assess the erosive potential of a flow.

1.2 Scope of this Work

The goal of this thesis is to develop a framework for a quantitative numerical prediction of cavitation erosion. In a first step, the erosive potential of the flow is determined numerically. Therefore, numerical simulations are performed to predict position, latitude, and dynamic behavior of vapor regimes. Additionally, collapse and shock formation have to be captured to reproduce collapse-induced loads and resulting impact load spectra. These general capabilities have been demonstrated for homogeneous mixture cavitation models in combination with compressible modelling of all phases as proposed by Schmidt *et al.*[19].

The present approach employs a density-based, low-Machnumber-consistent numerical method with explicit time-stepping, solving the inviscid Euler equations coupled with a homogeneous thermodynamic equilibrium cavitation model. Euler equations do not contain a limiting length scale (viscous length scale) for the creation of small scale flow structures. Neither does the homogeneous mixture model contain a limiting length scale for the formation of small scale vapor structures (smallest bubble diameter). A limit is, however, introduced by the spatial discretization. The first part of this work thus puts a focus on assessing the influence of spatial resolution on the prediction of hydrodynamic cavitation dynamics, collapse situations, and resulting impact load spectra.

Several models to assess erosion risk from either experimental or numerical flow data have been proposed (see Van Terwisga *et al.*[32] for a review). Based on the work of Karimi *et al.*[33], Berchiche *et al.*[34] and Franc *et al.*[35] proposed an analytical material model that derives incubation times from experimentally determined impact load spectra. For a numerical erosion prediction framework, we adapt this model to estimate incubation times based on numerically derived impact load spectra. Thereby, the quality of the generated information increases from a qualitative identification of a potential 'erosion risk' to a quantitative statement concerning material fatigue.

An important parameter influencing the erosive potential is the free gas content. To accurately model this effect in numerical simulations, it is mandatory to know the amount and distribution of gas in the system. Investigations by Iben *et al.*[30] and Freudigman *et al.*[31] indicate that cavitation can lead to enhanced discharge of solved gas. In the last part of this thesis a model to account for this interaction is introduced.

1.3 Outline

This thesis is structured in nine chapters. After the introduction, chapter 2 provides information on the physical background. Governing equations, physical and mathematical methods, and numerical

algorithms utilized in this work are introduced in chapter 3. Results of the thesis are presented in the subsequent four chapters. The first two chapters, chapters 4 and 5, assess fundamental capabilities of the homogeneous mixture model with special emphasis on the influence of spatial resolution and thermodynamic modelling. In chapter 4, the collapse of a vapor cloud is investigated. The prediction of hydrodynamic cavitation is assessed in chapter 5. Predicted cavitation dynamics, erosion sites and impact load spectra are compared with experimental data. In chapter 6, a method to estimate incubation times based on numerically determined impact load spectra is presented. Predictions are compared to experimental findings for different operating conditions and materials. Chapter 7 discusses the interaction of cavitation and free gas content. The predicted amount of gas released by cavitating nozzle flows is compared to experimental data. Finally, a short summary and outlook to future work are given in chapter 8 and 9.

2 Physical Background

The following chapter gives a brief overview on cavitation and cavitation erosion. Sections 2.1 and 2.2 introduce fundamentals and hydrodynamic cavitation, mainly following Brennen[1] and Franc *et al.*[2] Collapse-induced impact loads and resulting cavitation erosion are discussed in section 2.3, which is mainly based on Ref. 36. Parts of the literature review in section 2.3 have been published by the author in Ref. 37.

2.1 An Introduction to Cavitation

Cavitation is defined as the generation of vapor within a liquid due to a drop of the static pressure below vapor pressure.[1,2] Figure 2.1 shows a schematic p-T phase diagram. The stable states liquid and vapor are separated by the coexistence line which connects the triple point with the critical point. Brennen[38] differentiates two thermodynamic changes of state, which lead to the evaporation of a liquid. When the temperature T in a liquid is increased at approximately constant pressure, vapor may form as soon as T is equal to the saturation temperature T_v. This process is called boiling. When in contrast the pressure p in a liquid is decreased at approximately constant temperature, evaporation may take place as soon as p is equal to the saturation pressure p_v. This process is called cavitation.

Evaporation is usually followed by recondensation, when the ambient pressure rises, or vapor structures are advected into areas of higher static pressure. Collapse of vapor regions results in shock waves, which can trigger vibration modes of structures.[4] Near solid boundaries, the collapse of vapor structures often leads to severe damage of surface material.[1-4] The erosive potential of cavitating flows is discussed in more detail in section 2.3.

When p drops below p_v, a liquid can undergo phase-change at a phase boundary. In absence of a phase boundary, p can decrease below p_v without production of vapor, i.e., if the pressure difference $\Delta p = p_v - p$ is smaller than zero, the liquid sustains tension. The value of Δp can thus be defined as the tensile strength of a liquid. In a perfect liquid without any impurities, no phase boundaries exist a priori. In this case, a nucleus has to be created out of the liquid itself by overcoming intermolecular adhesion forces. This process is called homogeneous nucleation. Purified water, for example, can sustain tension of about 500 bar at room temperature.

Liquids in technical applications usually contain impurities like small gas bubbles, gas trapped in crevices at walls, or solid particles in the fluid. These sites act as nuclei, where phase change can occur at pressure differences lower than the theoretical value for a pure liquid.

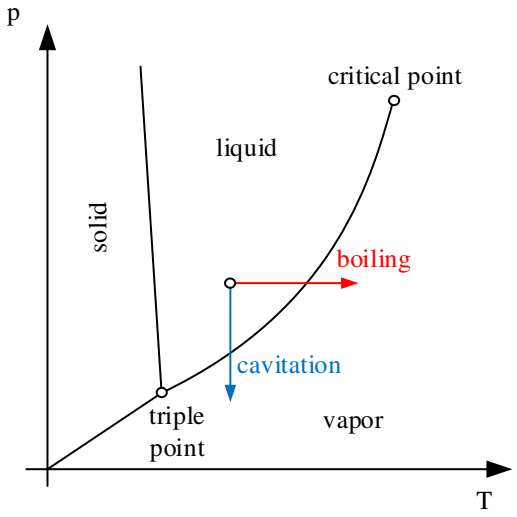

FIG. 2.1. Schematic *p-T* diagram.

2.2 Hydrodynamic Cavitation

Different types of cavitation can be classified by the driving mechanism of pressure decrease. In hydrodynamic cavitation, the pressure-drop is caused by the dynamics of liquid motion. Examples are the local acceleration of the flow, generated, e.g., by the contraction of a nozzle,[2] the curvature of a hydrofoil,[2-4] or the presence of vortical structures[5], such as the tip-vortex of a propeller blade, or vortices generated by a turbulent shear layer.[6,7] Other types include, e.g., acoustic cavitation, where a drop in pressure is induced by wave dynamics. A second field focuses on the detailed investigation of the behavior of single bubbles, including interaction with boundaries or other bubbles (e.g., Refs. 11,39-41). In contrast to hydrodynamic cavitation, the process of vapor generation is mostly of different nature (e.g. local energy input), or not of interest in more fundamental studies.

An important parameter to describe hydrodynamic cavitation is the cavitation number σ. A general definition is given by Franc *et al.*[2] as

$$\sigma = \frac{p_{ref} - p_v(T)}{\Delta p}, \tag{2.1}$$

where p_{ref} is a characteristic reference pressure in the fluid, $p_v(T)$ is the vapor pressure, and Δp is a characteristic pressure difference of the considered flow. Following this general definition, a common case specific definitions of σ for a cavitating foil as shown in FIG. 2.2 is[2]

$$\sigma = \frac{p_0 + \rho g h - p_v(T)}{\frac{1}{2}\rho u^2}, \tag{2.2}$$

where p_0, u, and ρ are pressure, flow velocity of the undisturbed flow, and liquid density, respectively. In this work, we use a definition suitable for nozzle flows[2]

$$\sigma = \frac{p_{upstream} - p_v(T)}{p_{upstream} - p_{downstream}}, \tag{2.3}$$

where the subscripts 'upstream' and 'downstream' denote pressures upstream and downstream of the nozzle.

Hydrodynamic cavitation can exhibit different topologies. For different values of Reynolds number Re, cavitation number σ, and angle of attack φ, the cavitating flow around a hydrofoil is shown in FIG. 2.2. Here, the following cavitation characteristics topologies can be observed.

- Traveling bubble cavitation is characterized by single, isolated bubbles which originate from nuclei present in the upstream flow. These bubbles grow in regions of low pressure and collapse upon pressure rises. The growth is mainly driven by evaporation of liquid at the phase boundary of the bubble. Cases when the growth is mainly due to the expansion of gas inside the bubble are referred to as gaseous cavitation or pseudo cavitation. Note that gaseous cavitation can occur when the pressure is still higher than the vapor pressure, while the pressure has to be lower than the vapor pressure for traveling bubble cavitation. In FIG. 2.2 (a), traveling bubble cavitation appears together with cloud cavitation at the downstream part of the foil.
- Sheet cavitation describes a vapor sheet that is attached to a contour in a low pressure region like a foil or a nozzle. In FIG. 2.2 (b) a vapor sheet develops from the leading edge of the foil and covers approximately two thirds of the foil. While the beginning of the sheet is usually fixed to the leading edge of the foil or the inlet of the nozzle, the position of cavity closure often oscillates and can shed vapor clouds which get advected downstream.
- Cloud cavitation describes a dense agglomeration of vapor bubbles. Vapor clouds can be generated, for example, by detachment from sheet cavities near the trailing edge of the foil as shown in FIG. 2.2 (b).
- Supercavitation defines a state, in which the extent of the cavity in flow direction is comparable or larger than the characteristic length of the flow problem. In FIG. 2.2 (c), the vapor sheet extends beyond the foil and closure takes place in the liquid. Supercavities are usually stable.

An additional form is vortex cavitation:

- Vortex cavitation is the generation of vapor in the low pressure region of vortex cores. Well-known examples are cavitating tip vortices or a cavitating hub vortex of a ship propeller, as shown in FIG. 2.3 in model scale.

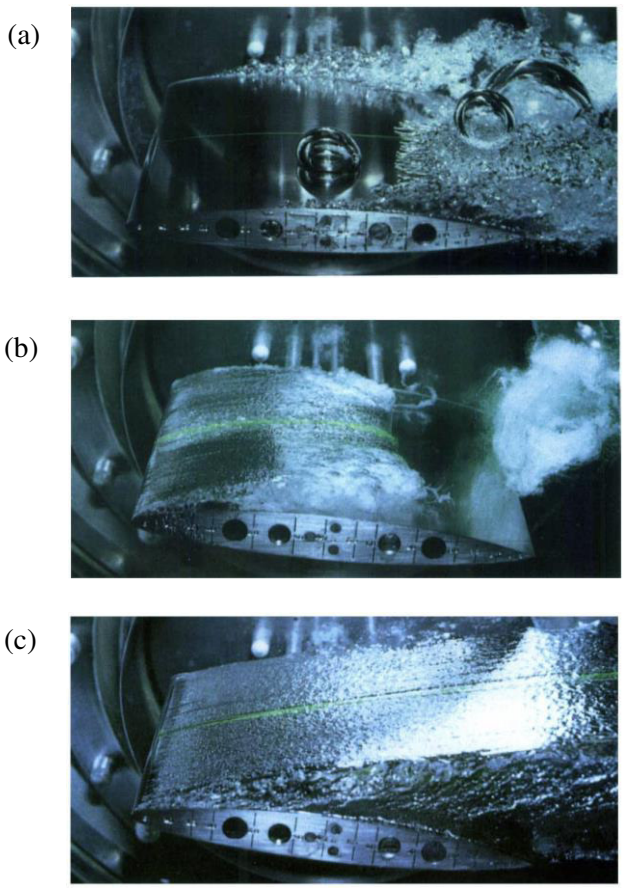

FIG. 2.2. Cavitating flow around a NACA16 012 hydrofoil with angle of attack φ. (a) Re = 600 000; σ = 0.13; φ = 2°. (b) Re = 1 000 000; σ = 0.81; φ = 6°. (c) Re = 1 000 000; σ = 0.045; φ = 8. Reprint with permission from Ref. 42. Copyright 1985 by Cambridge University Press.

In many cases of technical relevance the flow field features a combination of the above mentioned characteristics. As an example, FIG. 2.4 shows a ship propeller positioned upstream of a rudder. Here, sheet-, cloud-, and vortex cavitation are present.

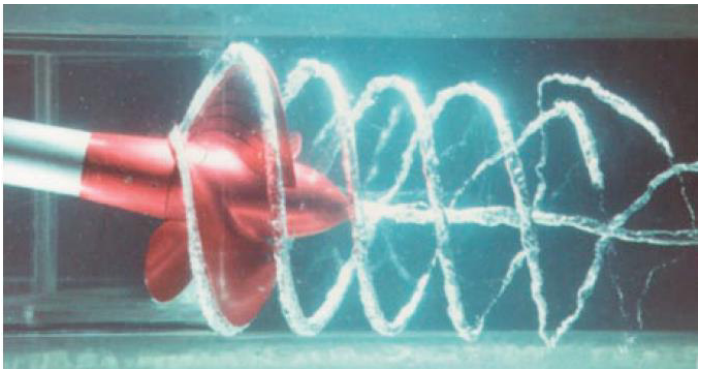

FIG. 2.3. Vortex cavitation at a ship propeller at model scale. Reprint with permission from Ref. 5. Copyright 2002 by Annual Review.

FIG. 2.4 Various types of cavitation on a naval ship model. Reprint with permission from Ref. 36. Copyright 2014 by Springer.

The so called shedding instability is a periodical combination of sheet and cloud cavitation. The periodical mechanism is sketched in FIG. 2.5 for a foil. In the beginning of a period, t/T=0, a sheet cavity has developed at the leading edge. This sheet gets detached by a reverse flow ('re-entrant flow') between foil and sheet, t/T=1/6. Once detached, t/T=1/3, the cavity is advected downstream in a spanwise vortex, t/T=2/3, and eventually collapses in areas of higher pressure. A Strouhal number characterizing a shedding mechanism with the frequency f can be defined as

$$Sr = \frac{f L_{max}}{u}, \tag{2.4}$$

where L_{max} is the maximum length of the attached cavity and u is velocity in the fluid on the cavity. Typical values of thus defined Strouhal numbers lie between 0.25 and 0.35.[2] This allows for an estimate of the order of magnitude of the shedding frequency f that can be expected in different applications

under certain flow conditions. For typical values found in ship propulsion ($L_{max} \approx 0.1$ m, $u \approx 10$ m/s), usually f = O(10 Hz). In the context of fuel injection ($L_{max} \approx 0.1 \cdot 10^{-3}$ m, $u \approx 100$m/s) we find f = O(10 kHz). Because of these potentially high frequencies, the shedding instability is known to have a high erosive potential, especially when detached vapor structures collapse near solid boundaries.[2]

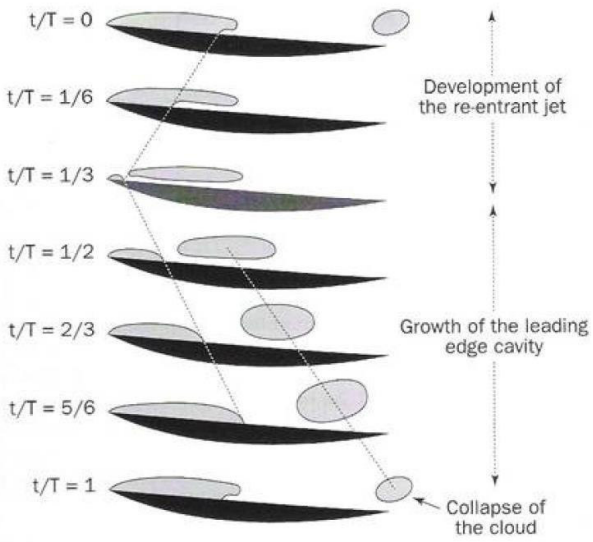

FIG. 2.5. Schematic of the shedding instability. Reprint with permission from Ref. 43. Copyright 1993 by ASME.

2.3 Collapse-Induced Impact Loads and Cavitation Erosion

A characteristic feature of cavitating flows is the collapse-like recondensation when vapor structures are advected into regions of higher static pressure. When the pressure in the liquid is higher than vapor pressure, condensation of vapor starts at the phase boundary. The specific volume of a liquid is usually several orders of magnitude smaller than the specific volume of vapor (for water: five orders of magnitude at room temperature). Thus, the condensation of vapor leads to an acceleration of the surrounding liquid.

Different collapse mechanisms are discussed in the literature. The most fundamental mechanism is the collapse of a spherical bubble, see FIG. 2.6 (a). Here, the liquid is accelerated towards the center of the bubble. When all vapor is condensed, inertia of the liquid leads to the formation of a spherical shock wave originating from the collapse center. The collapse of a bubble near a solid boundary is of particular interest. Here, the wall restricts acceleration of liquid and induces an asymmetrical collapse, as shown in FIG. 2.6 (b). Directed towards the wall, a liquid jet, the so called micro-jet, forms. When the jet hits the opposite phase boundary, the inertia of the liquid leads to the formation of a shock wave. The pressure Δp_{shock} generated by an instant decrease in velocity Δu can be estimated as

$$\Delta p_{shock} = \rho c \Delta u \,, \tag{2.5}$$

where the product of density ρ and sonic speed c is the acoustic impedance. Typical values for water ($\rho \approx 1000$ kg/m^3 and $c \approx 1500$ m/s) lead to pressure differences of 15 bar per 1 m/s velocity difference. Jet velocities up to O(100 m/s) have been observed experimentally, which leads to potential pressures on the material of more than 1000 bar. Collapse intensity can be further amplified by shock waves of previous nearby collapses, see FIG. 2.6 (c).

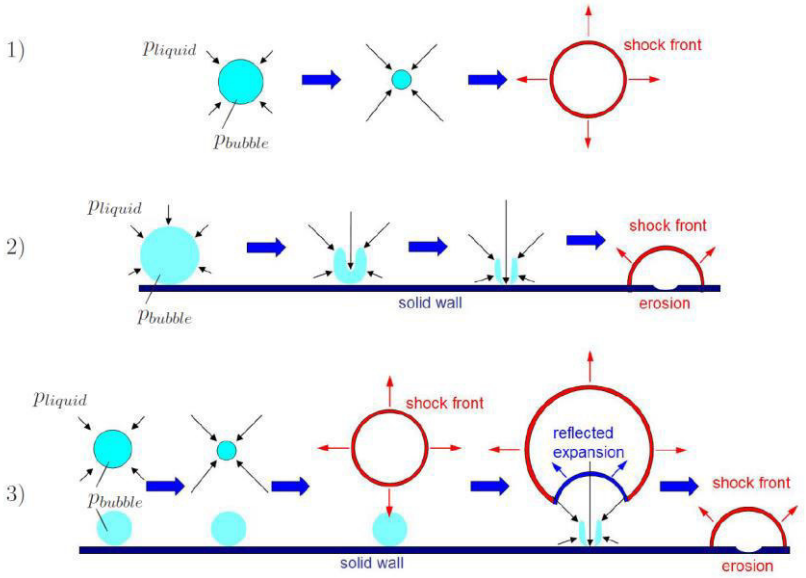

FIG. 2.6 Schematic of different collapse mechanisms. (a) Spherical collapse. (b) Aspherical collapse near a wall. (c) Interaction of a collapse-induced shock wave and a collapse near a wall. Reprint from Ref. 44. Copyright 2009 by I. H. Sezal.

Collapse-induced loads are characterized by a low duration, a high amplitude, and a small affected area.[36] These extreme values make impact loads difficult to measure. To quantify the strength of collapse-induced loads, two different approaches have been followed. Several groups used pressure sensors to measure collapse-induced pressure peaks.[8,10,45] While high frequency sensors allow for a temporal resolution of the peak, these sensors also implies low-pass spatial filtering down to the finite sensor size. Other groups have utilized short duration tests on soft ductile metals to identify pits formed by single impacts (known as pitting tests).[35,46] While pit-shape and size can give spatial information about the load, no time-dependent information of the impact is obtained. Additionally, information determined by this method is always a combination of the impact load and material properties. Still in some cases correlations have been found to account for the material influence.[35,46,47]

Occurring near a solid boundary, the collapse of a vapor structure can lead to the concentration of mechanical energy on a small surface area for a short time in the material. This results in high stress and strain rates in time, and stress and strain gradients in space that eventually lead to erosion damage.

Cavitation occurs in many technical applications. To illustrate this variety, FIG. 2.7 holds two examples of erosion damage caused by cavitation at different scales: a spillway of the Hoover Dam and a nozzle hole of a fuel injector. While both examples are geometrically similar, their characteristic dimension differs by about five orders of magnitude. Depending on the application, cavitation erosion has different consequences. In most cases, erosion leads to the destruction of the device (e.g. marine propulsion[2] or turbo machinery[4], FIG. 2.8). In other cases, shape modification due to material removal may influence the general functionality (e.g. fuel injectors[48]). Furthermore, in some applications contamination of the processed fluid with solid particles of eroded material is unacceptable (e.g. food processing[49]). Energy focusing in cavitating flows is also utilized in a growing number of applications, for example in medical applications[50,51], cleaning technologies[52,53], and the optimization of spray characteristics[54-56].

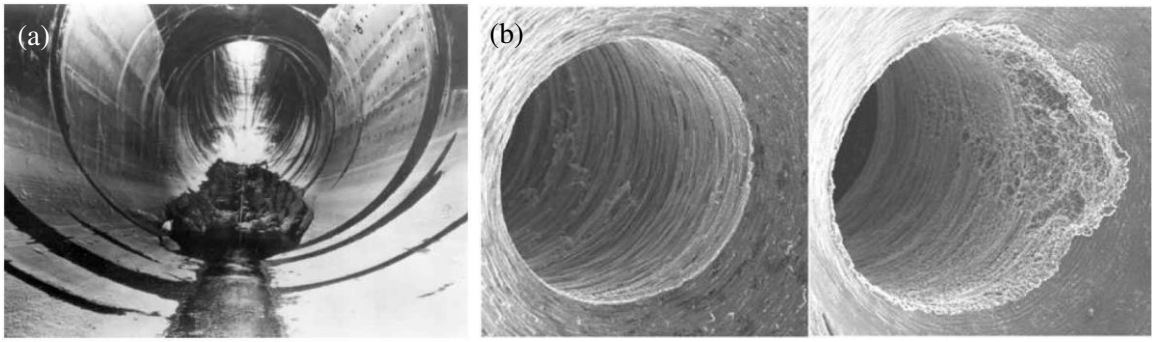

FIG. 2.7 (a) Erosion damage in the concrete of a spillway of the Hoover Dam (channel diameter 15.2 m, extend of damage: length 35 m width 9 m, depth 13.7 m). Reprint from Ref. 57. (b) Nozzle hole of a fuel injector before (left) and after erosion damage (right). Reprint from Ref. 58. Copyright 2005 by F. Wrona.

FIG. 2.8 Damage on the blades at the discharge from a Francis turbine. Reprint with permission from Ref. 4. Copyright 1994 by C. E. Brennen.

In general, cavitation erosion can be divided into three stages[2]: the incubation period, in which no material is removed, followed by the acceleration period, in which mass loss begins and increases, and, finally, the steady state period, characterized by constant mass loss. Some authors define an additional deceleration period, where mass loss is reduced after the removal of material has changed geometry of

the flow problem. The different phases can be more or less pronounced, depending on the application and the eroded material. Among many others, Patella *et al.,*[46] and Franc[35] used pitting tests to identify pits formed by single impacts during the incubation period to describe the aggressiveness of a cavitating flow. By counting and analyzing the pits, information about the distribution of intensity of events (quantified by pit diameter, depth, or volume) over the frequency of occurrence, i.e., an impact load spectrum,[35] was generated. Franc measured pits up to 220 μm in diameter, while the contribution of a pit class to the damage on the material (damaged surface and pit volume) exhibited a maximum for pits of approx. 100 μm in diameter[35]. Furthermore, several groups used pressure sensors to measure pressure peaks caused by the collapse of single bubbles created artificially,[39,59] or hydrodynamic cavitation[8,10,45]. Okada *et al.*[60] combined two techniques by analyzing single pits on a pressure sensor and comparing them to the recorded pressure signal. The author found a linear relation between the pit diameter and the corresponding peak pressure. Hattori *et al.*[47] evaluated particles removed from the material by a device generating cavitation through a vibrating horn. They reported that during the initial stage the volume loss was dominated by small particles (≈ 3 μm) generated by impact fracture, while larger particles (> 10 μm) generated by fatigue fracture dominated the erosion process in the steady state period. Similar results were reported earlier by Endo *et al.*[61] It was stated that the two mechanisms are triggered by impacts of different strength, namely single high-intensity impacts in the case of impact fracture, and a large number of lower-intensity impacts in the case of fatigue fracture. The experimental studies indicate that for a comprehensive quantification of the erosive potential of a flow, the complete load spectrum on the material has to be determined.

3 Numerical Method and Physical Models

In the following, the governing equations, numerical method and thermodynamic models are introduced.

3.1 Governing Equations and Numerical Method

We solve the compressible Euler equations

$$\frac{\partial \underline{q}}{\partial t} + \sum_{i=1}^{3} \frac{\partial \underline{F}_i}{\partial x_i} = 0, \tag{3.1}$$

where $\underline{q}$ is the vector of the conserved quantities $\underline{q} = (\rho, \rho u_1, \rho u_2, \rho u_3, \rho E)^T$ and $\underline{F}_i(\underline{q})$ are the fluxes of mass, momentum, and energy

$$\underline{F}_i(\underline{q}) = \rho u_i \begin{pmatrix} 1 \\ u_1 \\ u_2 \\ u_3 \\ E \end{pmatrix} + p \begin{pmatrix} 0 \\ \delta_{1i} \\ \delta_{2i} \\ \delta_{3i} \\ u_i \end{pmatrix}, \tag{3.2}$$

with density ρ, velocity in i-direction u_i, specific total energy $E = e + 0.5\sum u_i^2$. δ_{ij} is the Kronecker symbol. Equation 3.1 is discretized by a finite volume method, where the physical fluxes are approximated by a low-Mach-number consistent numerical flux function $\underline{F}_{i,num}$. The numerical flux $\underline{F}_{i,num}$ in x_1-direction, where the superscripts "-" and "+" denote the "left-" and "right-hand side" quantities, and $u*$ and $p*$ denote cell-face quantities, is defined as

$$\underline{F}_{1,num} = \rho^- u* \begin{pmatrix} 1 \\ u_1^- \\ u_2^- \\ u_3^- \\ E^- \end{pmatrix} + p* \begin{pmatrix} 0 \\ 1 \\ 0 \\ 0 \\ u* \end{pmatrix} \qquad \text{for } u* \geq 0 \tag{3.3a}$$

$$\underline{F}_{1,num} = \rho^+ u* \begin{pmatrix} 1 \\ u_1^+ \\ u_2^+ \\ u_3^+ \\ E^+ \end{pmatrix} + p* \begin{pmatrix} 0 \\ 1 \\ 0 \\ 0 \\ u* \end{pmatrix} \qquad \text{for } u* < 0. \tag{3.3b}$$

The cell-face velocity $u*$ is computed from

$$u* = \frac{\rho_n^+ u_1^+ + \rho_n^- u_1^-}{\rho_n^+ + \rho_n^-} - \frac{p^+ - p^-}{(\rho_n^+ + \rho_n^-) c_m}, \tag{3.4}$$

with

$$\rho_n^+ = \frac{1}{4}(3\rho^+ + \rho^-), \rho_n^- = \frac{1}{4}(3\rho^- + \rho^+). \tag{3.5}$$

In Eq. 3.4, c_m is an estimate for the fastest signal speed. Based on numerical experiments we found that the constraint $c_m \geq 200 m/s$ results in robust simulations while avoiding excessive numerical dissipation

$$c_m = \max(c^+, c^-, c_{\min}), \tag{3.6}$$

This quantity determines numerical dissipation of this scheme.[62] As discussed in Ref. 22, low-Mach-number consistency is achieved by computing the cell-face pressure from the arithmetic mean of the pressures of the neighboring cells,

$$p^* = \frac{p^+ + p^-}{2}. \tag{3.7}$$

Left and right velocity reconstructions are subject to a high resolution TVD (total variation diminishing) limiter,[63] and are formally third-order accurate for smooth fields. Pressure, density and specific internal energy use first-order reconstruction. Kinetic contribution to the specific total energy is calculated with the reconstructed velocity components.

The equations are advanced in time by an explicit second-order accurate low-storage 4-step Runge-Kutta method. The numerical time step is subject to a CFL criterion *CFL*=1.4. We adopt body-fitted structured hexahedral grids to discretize the flow field.

3.2 Physical Model

Cavitating flows feature a broad range of length scales Δ_{flow}, ranging from the size of nuclei (< O(10^{-4} m)) to the size of large-scale coherent vapor structures, which are of the same order of magnitude as the characteristic length scales of the flow problem, e.g., O(10^{-3}m) – O(1m) for injection nozzles and ship propellers, respectively. Additionally, the applied finite volume method introduces a length scale Δ_{CFD} that is characteristic for the numerical grid. The parameter $\psi=\Delta_{flow}/\Delta_{CFD}$ allows for a classification of different cavitation models available in literature. The discussion is given in more detail in Refs. 20 and Ref. 64.

For $\psi >> 1$, cavitation structures are fully resolved by the computational grid. This allows for the application of models that explicitly capture phase boundaries like, e.g., sharp interface methods. In these models, a set of transport equations for mass momentum and energy is solved for each phase. Interaction between the phases is modeled via explicit exchange terms. While the level of detail that can

be investigated is high for these models, the required spatial resolution leads to high computational cost. Consequently, computations are usually limited to a small number of cavitation structures.

For $\psi << 1$, cavitation structures are smaller than the computational grid size and thus are underresolved. This allows for the application of bubbly flow models, where the liquid phase is treated as a continuum, while particles in a Lagrangian frame of reference represent the vapor phase as dispersed bubbles. Interaction of both phases is often modeled with the Rayleight-Plesset equation or derivations thereof. Bubbly flow models are well suited to study, e.g., the influence of nuclei distributions on incipient cavitation. Special treatment is needed as soon as cavitation structures are of the same size as the numerical resolution, i.e., $\psi \approx 1$.

However, hydrodynamic cavitation can feature cavitation structures that are approximately of the same size as the flow problem and thus have to be resolved ($\psi>1$). Additionally, structures like individual bubbles in a vapor cloud are computationally too expensive to resolve ($\psi<1$). Consequently, simulating hydrodynamic cavitation requires a model that is valid in the full range of ψ. This is fulfilled by so called 'single fluid-' or 'homogeneous mixture-' models. FIG. 3.1 illustrates this approach. Consider a control volume Ω containing a two-phase mixture with vapor structures of different sizes as sketched in FIG. 3.1 (a). Volume fraction β and mass fraction ε of a component Φ are defined as

$$\beta_\Phi = \frac{V_\Phi}{V} \quad \text{with} \quad \sum_\Phi \beta_\Phi = 1, \tag{3.8}$$

$$\varepsilon_\Phi = \frac{m_\Phi}{m} \quad \text{with} \quad \sum_\Phi \varepsilon_\Phi = 1. \tag{3.9}$$

Properties of the modelled single fluid are defined by mixture of each single component, FIG. 3.1 (b). Thus, information regarding length scales smaller than the grid size ($\psi<1$) is lost and conserved quantities of mass, momentum and energy become

$$\overline{\rho} = \frac{1}{\Omega}\int_\Omega \rho d\Omega, \tag{3.10}$$

$$\overline{\rho u_i} = \frac{1}{\Omega}\int_\Omega \rho u_i d\Omega, \tag{3.11}$$

$$\overline{\rho E} = \frac{1}{\Omega}\int_\Omega \rho E d\Omega. \tag{3.12}$$

Density ρ_Φ of component Φ can be expressed as

$$\rho_\Phi = \frac{m_\Phi}{V_\Phi} = \frac{\varepsilon_\Phi m}{\beta_\Phi V} = \frac{\varepsilon_\Phi}{\beta_\Phi}\overline{\rho}, \tag{3.13}$$

where m_Φ is the mass of Φ and V_Φ the volume occupied by that component. Mixture density $\overline{\rho}$, defined by mass m and volume V of the whole system, finally depends on all single components

$$\bar{\rho} = \frac{m}{V} = \sum_{\Phi} \beta_{\Phi} \rho_{\Phi} \ . \tag{3.14}$$

A remaining open question is the influence of spatial resolution on the predictive capability of the applied model. This will be addressed by investigating a collapse situation in chapter 4 and hydrodynamic cavitation in chapter 5.

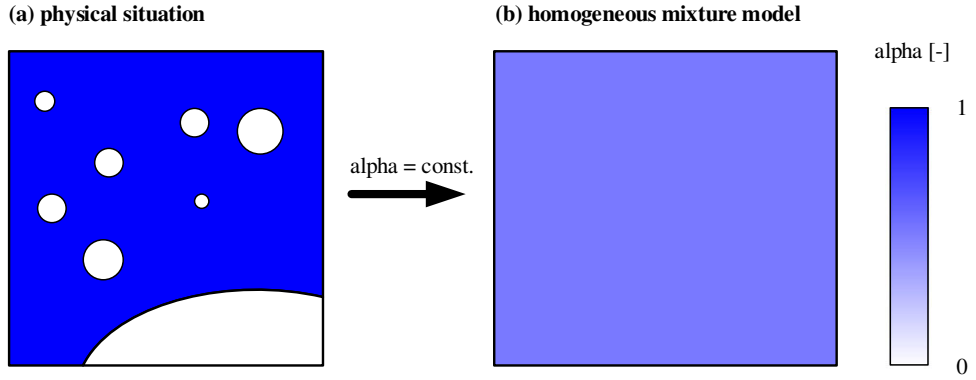

FIG. 3.1 (a) Example of a physical distribution of different phases in a control volume. (b) Representation of (a) by a homogeneous mixture model.

3.3 Thermodynamic Models

3.3.1 Full Thermodynamic Model

Following Ref. 20, the thermodynamic properties of the working fluid are characterized by closed-form equations of state. For the liquid phase a modified Tait equation is used

$$p(\rho,T) = B\left[\left(\frac{\bar{\rho}}{\rho_{sat,l}(T)}\right)^{N} - 1\right] + p_{sat}(T) \tag{3.15}$$

with B=3300 bar and N=7.15, together with an expression for internal energy.[65] The phase transition model is based on local equilibrium assumptions for pressure, temperature, and specific Gibbs functions. In the two phase regime, the mixture density $\bar{\rho}$ and mass specific internal energy $\bar{e}$ are thus convex combinations of the saturation densities of liquid $\rho_{sat,l}$ and vapor $\rho_{sat,v}$, and internal energy at saturation of liquid $e_{sat,l}$ and vapor $e_{sat,v}$, respectively

$$\bar{\rho} = \alpha \rho_{sat,v}(T) + (1-\alpha)\rho_{sat,l}(T)\,, \tag{3.16}$$

$$\bar{e} = \varepsilon e_{sat,v}(T) + (1-\varepsilon)e_{sat,l}(T)\,, \tag{3.17}$$

$$\varepsilon\bar{\rho} = \alpha \rho_{sat,v}(T)\,, \tag{3.18}$$

$$p = p_{sat}(T)\,, \tag{3.19}$$

$$0 \le \alpha < 1, \quad 0 \le \varepsilon < 1\,. \tag{3.20}$$

Here, α is the vapor volume fraction and ε is the vapor mass fraction. Following Ref. 66, temperature dependent saturation conditions in Eq. 3.16 - 3.18 are modeled by polynomial fits of the IAPWS[67] data. Finally, the piecewise definition of α is

$$\alpha = \begin{cases} 0 & , \ \bar{\rho} \ge \rho_{sat,l}(T), \\ \dfrac{\rho_{sat,l}(T) - \bar{\rho}}{\rho_{sat,l}(T) - \rho_{sat,v}(T)} & , \ \bar{\rho} < \rho_{sat,l}(T). \end{cases} \tag{3.21}$$

3.3.2 Barotropic Equation of State

In a barotropic flow, isothermal and isobaric lines (in two dimensions) or planes (in three dimensions) collapse. An equation of state can therefore be formulated as sole function of pressure, independent of temperature, i.e., $\rho=\rho(p)$. Although the equation of state is independent of temperature, it should be noted that it does not correspond to an isothermal formulation, see FIG. 3.2. Computation of the energy equation is not necessary with a barotropic thermodynamic model.

The liquid phase is again modelled with a modified Tait equation. In contrast to Eq. 3.15, saturation properties are evaluated for a constant reference temperature T_{ref}.

$$p(\rho) = B\left[\left(\frac{\bar{\rho}}{\rho_{sat,l}(T_{ref})}\right)^N - 1\right] + p_{sat}(T_{ref})\,, \qquad \text{for } \bar{\rho} \ge \rho_{sat}\,. \tag{3.22}$$

The isentropic definition of the speed of sound is used to model the two phase mixture

$$c = \sqrt{\left.\frac{\partial p}{\partial \rho}\right|_{s=const}} \quad \rightarrow \quad \partial p = c^2 \partial \rho\,. \tag{3.23}$$

Phase change is assumed to take place in equilibrium. Thus, c is the equilibrium speed of sound c_{eq}, see e.g. Ref. 2

$$\frac{1}{\bar{\rho} c_{eq}^2} \cong \frac{\alpha}{\rho_v c_v^2} + \frac{1-\alpha}{\rho_l c_l^2} + \frac{(1-\alpha)\rho_l c_{p,l} T}{(\rho_v L)^2}\,, \tag{3.24}$$

where subscripts v and l denote properties of the vapor phase and the liquid phase, respectively, c_p is the specific heat capacity, and L the latent heat of evaporation. Integrating from a saturated state

$$p = p_{sat} + \int_{\rho_{sat}}^{\bar{\rho}} c_{eq}^2 \partial \rho\,, \qquad \text{for } \bar{\rho} < \rho_{sat} \tag{3.25}$$

leads to[68]

$$p = p_{sat} + \frac{\log\left(\frac{\rho}{A+B\rho}\right)}{A}, \qquad \text{for } \bar{\rho} < \rho_{sat}, \tag{3.26}$$

where A, B, a, and b are the constants

$$A = a - \frac{b\rho_l}{\rho_v - \rho_l} \quad , \qquad B = \frac{b}{\rho_v - \rho_l}, \tag{3.27}$$

$$a = \frac{1}{\rho_l c_l^2} + \frac{T\rho_l c_{p,l}}{L^2 \rho_v^2}, \qquad b = \frac{1}{\rho_v c_v^2} - \frac{1}{\rho_l c_l^2} + \frac{T}{L^2 \rho_v^2}(\rho_l c_{p,v} - \rho_l c_{p,l}). \tag{3.28}$$

Saturation properties in the piecewise definition of α are evaluated for constant T_{ref}

$$\alpha = \begin{cases} 0 & , \ \bar{\rho} \geq \rho_{sat,l}(T_{ref}), \\ \dfrac{\rho_{sat,l}(T_{ref}) - \bar{\rho}}{\rho_{sat,l}(T_{ref}) - \rho_{sat,v}(T_{ref})} & , \ \bar{\rho} < \rho_{sat,l}(T_{ref}). \end{cases} \tag{3.29}$$

Evaporation leads to a drop in temperature due to latent heat. FIG. 3.2 schematically shows the isentropic expansion of a saturated liquid, P_1, into the two phase region, P_3. As saturation densities in Eq. 3.29 are evaluated for a constant reference temperature (P_1 and P_2 in FIG. 3.2 for liquid and vapor respectively), $\alpha(P_3)$ is approximated by $\alpha(P_3^*)$. In the following, an upper estimate for the error will be derived. The error is most significant for high values of α (corresponding low densities) and a large temperature difference between P_1 and P_3. As will be introduced in section 3.3.4, a minimum admissible density is defined in the present method. A typical value ρ_{min} = 5 kg/m³ is used in this estimate. The largest temperature difference ΔT can be generated by expanding to the triple line (T=273K), i.e., $\Delta T = T_{ref}$. The highest reference temperature used in this work is T_{ref}=293K. The relative error in the calculation of α is small ($< 4\text{x}10^{-5}$), even for higher values of T_{ref}, see Table I.

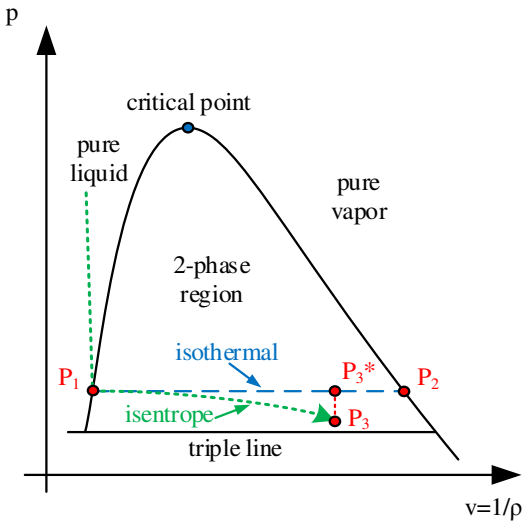

FIG. 3.2 Schematic *p-v* diagram. Green dotted line shows isentropic expansion starting in pure liquid, leading into the two phase regime. Blue dashed line shows the corresponding isothermal behavior in the two phase region. Solid state is not considered.

Table I: Influence of T_{ref} on α for water. Fluid properties are found in Ref. 69.

$T_{ref} = \Delta T$ [K]	$\rho_{l,sat}(T_{ref})$ [kg/m³]	$\rho_{v,sat}(T_{ref})$ [kg/m³]	α [-]	$(\alpha(T_{ref})-\alpha(273\text{K}))/\alpha(273\text{K})$ [-]
273	999.78	0.004855	0.995004	-
293	998.19	0.01731	0.995008	$\approx 4\text{x}10^{-6}$
333	983.16	0.13030	0.995046	$\approx 4\text{x}10^{-5}$

3.3.3 Barotropic Two-Phase Mixture with Free Gas Content

In the following, the barotropic model is extended to account for additional gas content. Gas can either be solved in the liquid, or free. Together with the liquid and vapor phase, this gives a total of four components to differentiate. They are identified by the subscript Φ, where Φ=1 denotes liquid, Φ=2 vapor, Φ=3 solved gas, and Φ=4 free gas.

Pure liquid (component 1) and liquid-vapor mixture (components 1 and 2) are modeled based on the definition of the isentropic speed of sound (Eq. 3.23). Compared to section 3.3.2, the speed of sound is assumed to be constant for both regimes. This leads to a piece-wise definition of the density of components 1 and 2. Additionally, the model assumes that solved gas does not change the behavior of the liquid phase. Eq. 3.30 thus describes the density of components 1, 2, and 3

$$\rho_{1,2,3} = \rho_{l,sat} + \frac{1}{c^2}(p - p_{sat}), \quad \text{with } c = \begin{cases} c_l = const. & for\ p \geq p_{sat} \\ c_m = const. & for\ p < p_{sat} \end{cases}. \tag{3.30}$$

Free gas is modeled as isothermal and ideal

$$\rho_4 = \frac{p}{R_G T_{ref}}, \tag{3.31}$$

where R_G is the specific gas constant and T_{ref} is the reference temperature. A closed form equation of state is obtained by combining Eq. 3.30 and Eq. 3.31 in Eq. 3.14

$$\bar{\rho} = \sum_{\Phi} \beta_\Phi \rho_\Phi = (\beta_1 + \beta_2 + \beta_3)\left[\rho_{l,sat} + \frac{1}{c^2}(p - p_{sat})\right] + \beta_4 \frac{p}{R_G T_{ref}} \tag{3.32}$$

Rewriting Eq. 3.32 with

$$\beta_1 + \beta_2 + \beta_3 = 1 - \beta_4 . \tag{3.33}$$

and substituting the volume fraction β with mass fraction ε (Eq. 3.13) leads to a function of pressure p and mass fraction of free gas ε_4

$$\bar{\rho} = \left(1 - \varepsilon_4 \frac{\bar{\rho} R_G T_{ref}}{p}\right)\left(\rho_{l,sat} + \frac{1}{c^2}(p - p_{sat})\right) + \varepsilon_4 \bar{\rho}, \quad c = \begin{cases} c_l & for\ p \geq p_{sat} \\ c_m & for\ p < p_{sat} \end{cases}. \tag{3.34}$$

With known ε_4, the local pressure p can now be obtained from the mixture density $\bar{\rho}$ by solving the quadratic equation. Due to the piece-wise definition of Eq. 3.30, p is first computed for $c=c_l$. If the solution does not fall into a valid range, i.e., $p<p_{sat}$, p is recomputed for $c=c_m$. In most cases, most of the computational cells in the domain contain no vapor and thus this procedure is appropriate. With known pressure, β_4 can be computed from Eq. 3.13 and Eq. 3.31. Finally, the piece-wise definition of α is

$$\alpha = \beta_2 = \begin{cases} 0 & , \ p \geq p_{sat}(T_{ref}), \\ \dfrac{(1-\beta_4)\rho_{sat,l}(T_{ref}) - (1-\varepsilon_4)\bar{\rho}}{\rho_{sat,l}(T_{ref}) - \rho_{sat,v}(T_{ref})} & , \ p < p_{sat}(T_{ref}). \end{cases} \tag{3.35}$$

Until now, the amount of gas in a cell does only change by passive transport and the total mass of free gas in the computed domain only changes by transport over boundaries. In the following, the model is extended to allow for the release of solved gas. Three physical processes can change the free gas content:

(a) When a given volume of liquid evaporates, the gas solved in that volume is released.

(b) Solved gas gets released from the liquid by diffusion at an interfacial area between liquid and gas or liquid and vapor, if the static pressure is lower than the saturation pressure of gas in the liquid.

(c) Free gas gets solved in the liquid by diffusion at an interfacial area between liquid and gas or liquid and vapor, if the static pressure is higher than the saturation pressure of gas in the liquid.

For process (b) and (c) the change in mass by diffusion Δm is proportional to a concentration difference Δc (e.g. expressed as difference of partial pressures of gas in the liquid and inside a bubble), the interfacial area A, and time Δt.

$$\Delta m \propto \Delta c \cdot A \cdot \Delta t \,. \tag{3.36}$$

As A is not available in the framework of the applied homogeneous mixture model, process (b) and (c) cannot be modelled physically correct without major assumptions. In this work, we thus focus on process (a), which is described in the following

Gas is set free in a computational cell, whenever liquid evaporates. The vapor volume fraction $\Delta\beta_2'$ defines the volume of newly created vapor, when release of gas is suppressed. The model assumes that the volume defined by $\Delta\beta_2'$ is filled with free gas, $\Delta\beta_4$, and vapor, $\Delta\beta_2$

$$\Delta\beta_2' = \Delta\beta_2 + \Delta\beta_4 \,. \tag{3.37}$$

The mass ratio of released gas, $\Delta\varepsilon_4$, and created vapor, $\Delta\varepsilon_2$, equals the mass ratio of solved gas, ε_3, and liquid, ε_1

$$\frac{\Delta\varepsilon_4}{\Delta\varepsilon_2} = F\frac{\varepsilon_3}{\varepsilon_1} \,. \tag{3.38}$$

F is a model parameter. Process (a) is modelled physically for F=1. Combining Eq. 3.13 and Eq. 3.38 in Eq. 3.37 leads to

$$\Delta\beta_2' = \Delta\varepsilon_4 \frac{1}{F}\frac{\varepsilon_1}{\varepsilon_3}\frac{\bar{\rho}}{\rho_{v,sat}} + \Delta\varepsilon_4 \frac{\bar{\rho}}{\rho_4} \,. \tag{3.39}$$

Finally, rearranging Eq. 3.39 provides the newly created mass fraction of free gas $\Delta\varepsilon_4$

$$\Delta\varepsilon_4 = \frac{\Delta\beta_2'}{\frac{1}{F}\frac{\varepsilon_1}{\varepsilon_3}\frac{\bar{\rho}}{\rho_{v,sat}} + \frac{\bar{\rho}}{\rho_4}} \,. \tag{3.40}$$

If F is chosen F>1 it has to be ensured that not more gas is released, as is solved in the liquid

$$\Delta\varepsilon_4 = \max\left(\frac{\Delta\beta_2'}{\frac{1}{F}\frac{\varepsilon_1}{\varepsilon_3}\frac{\bar{\rho}}{\rho_{v,sat}} + \frac{\bar{\rho}}{\rho_4}}, \varepsilon_3\right) \quad for\ F > 1. \tag{3.41}$$

ε_3 and ε_4 each require one scalar transport equation. In some cases it can be assumed that the total gas content, i.e., $\varepsilon_3+\varepsilon_4=\varepsilon_{g,tot}$, is constant in the fluid domain. Examples include flow situations, where

the liquid is homogeneously saturated with gas at a certain condition (see section 7). Here, only one transport equation is sufficient as ε_3 can be calculated from ε_4 (or vice visa). Finally, an additional transport equation is required for ε_2 to distinguish between newly created and transported vapor.

FIG. 3.3 summarizes the algorithm.

```
// density and mass fractions are known from flux computations
// and transport equations
calculate p from Eq. (3.32)
calculate β2 and β2' from ε2 and ε2'

//no evaporation, no release of solved gas
if     (β2 >= β2') {
   calculate β4
}
//evaporation and release of solved gas
elseif (β2 <  β2') {
   calculate Δε4 from Eq. (3.40) or Eq. (3.41)

   ε4 = ε4 + Δε4
   ε3 = ε3 - Δε4

   calculate p from Eq. (3.32)
   calculate β2 and β4
}
```

FIG. 3.3. Gas model algorithm.

3.3.4 Density Limiter

Figure 3.4 (a) shows the isentropic thermodynamic path in a *p-v* diagram. Along equilibrium isentropes in the two-phase region, the temperature of the mixture decreases due to latent heat of evaporation. FIG. 3.4 (b) shows that an isentropic expansion from the liquid phase reaches the triple line and prevents complete evaporation. We hence define a minimum admissible mixture density of ρ_{min} corresponding to a maximum admissible vapor volume fraction α_{max}. However, as the numerical approach is explicit in time, it cannot a priori be ensured that this lower density limit is preserved. In case that the computed density is lower than the specified limit, an a posteriori correction to $\overline{\rho} = \rho_{min}$ is applied. While specific internal energy and momentum remain unmodified, limiting $\overline{\rho}$ leads to an increase of mass in the respective cell. In the reference simulation performed in chapter 5 the resulting

maximum increase of mass in the entire computational domain per timestep is less than 0.1% with respect to the mass flow rate.

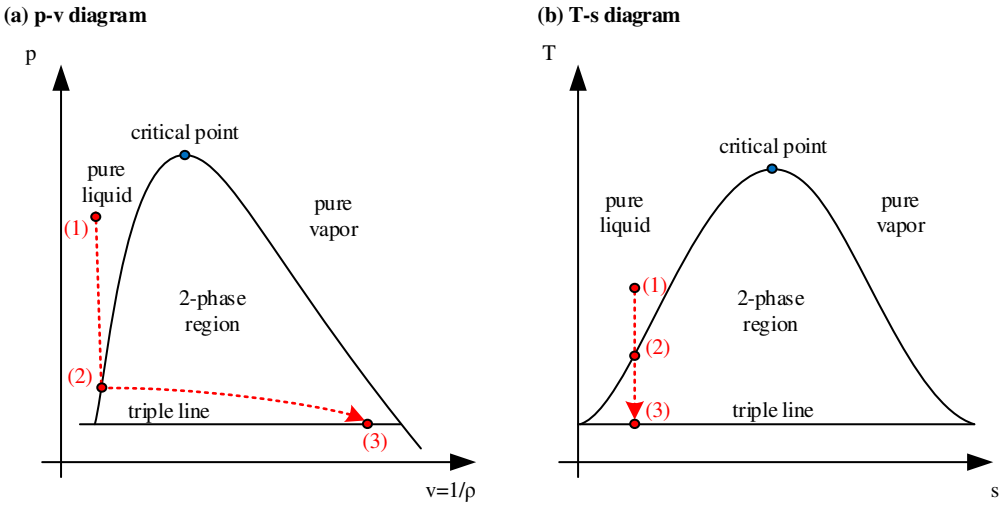

FIG. 3.4 Schematic phase diagrams: (a) *p-v* diagram. (b) *T-s* diagram. Red dotted line shows isentropic expansion starting in pure liquid. (1-2) Expansion of pure liquid. (2-3) Expansion of two-phase mixture. Solid state is not considered. Reprint with permission from Ref. 37. Copyright 2015 by AIP Publishing.

3.4 Quantification of Impact Load Spectra

The technical term ‘impact load spectrum’ describes the temporal rate and the strength of collapse-induced loads in a cavitating flow.[8] It is either defined globally as loads per time, or locally as loads per time and area. The impact load spectrum can be used to define the erosive potential of a flow[2] and is a characteristic quantity for collapse-related dynamics.

In experimental studies mainly high frequency pressure sensors and pitting tests have been utilized to quantify impact load spectra. Pressure sensors imply low-pass spatial filtering down to finite sensor size, while with pitting tests shape and size of pits can provide spatial information about the load, but no time-dependent information of the impact. Additionally, for both methods only information at the wall is obtained.

Spatially and temporally resolved information is available in numerical simulation. To quantify the load spectrum in the entire fluid domain, we introduce a collapse detection algorithm based on the work of Mihatsch *et al.*[70]. For this purpose we define physical criteria to identify collapses of isolated vapor regions and to characterize the strength of the generated shock waves as predicted by numerical simulation.

Collapse stages are illustrated in FIG. 3.5. The onset of condensation is indicated by a negative divergence of the velocity. Due to compressibility of the liquid, $div(\vec{u})$ is proportional to the vapor production rate only as long as the thermodynamic state corresponds to a two-phase mixture. Assuming that the specific Gibbs functions remain in equilibrium and disregarding solved or dissolved gas, the

pressure within the vapor region equals vapor pressure. Hence, the surrounding liquid accelerates towards the collapse center until the vapor completely condenses at the last stage of the collapse. At this time instant, the condensation rate exhibits a maximum. In the following, flow inertia results in a strong pressure increase. The pressure maximum is reached when the mass flux towards the center vanishes. At that point, $div(\vec{u})$ changes sign and the negative radial pressure gradient displaces fluid. Consequently, the pressure at the collapse center decreases and may even lead to a re-evaporation of the liquid (rebound). As non-condensable gas is not modeled, the rebound mechanism mentioned here is due to the inertia of the velocity field after the collapse, see, e.g., Ref. (71). Above considerations motivate an algorithm for a collapse detector as follows:

- ‘Candidate’ cells are computational cells where vapor content condensed completely during the previous time step. If the neighboring cells of such a ‘candidate’ contain liquid only, an isolated collapse is detected.
- Once a collapse is detected, the maximum pressure is determined at the time instant when the divergence of the velocity field changes sign.
- Collapse strength is characterized by its maximum (negative) divergence and its maximum pressure.

The algorithm is sketched in FIG. 3.6.

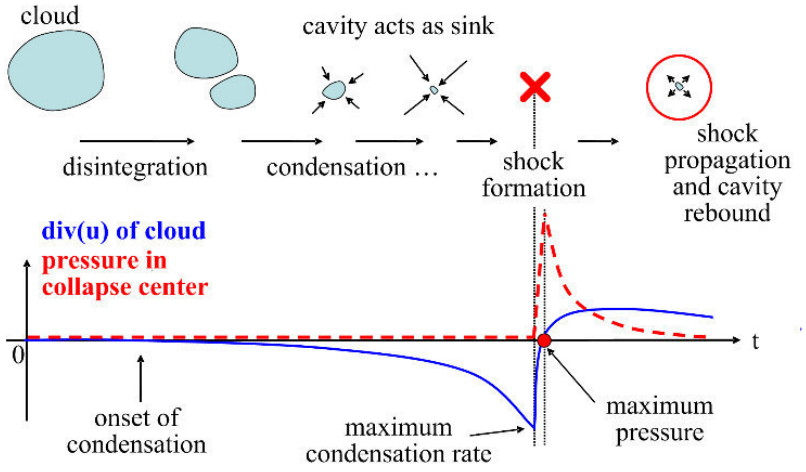

FIG. 3.5. Collapse stages of a vapor region, temporal evolution of velocity divergence (solid blue line) and pressure at the collapse-center (dashed red line). Reprint with permission from Ref. 72. Copyright 2011 by Springer.

```
// initial value of the status of a cell
status = 0

// check if cell is a "candidate" at timestep "t"
if (status == 0 .and. α(t) == 0 .and. α(t-1) > 0) {
   status = 1
   // loop over "j" neighbors to check if collapse is isolated
   for (i = 1 to j) {
      if (α_neighbor(i,t) > 0) {
      status = 0
      }
   }
}
// store "div(u)" when local minimum is reached
if (status == 1 .and. div(u(t-1)) < div(u(t)) {
store div(u(t-1))
   status = 2
}
// store "p" when "div(u)" changes sign
if (status == 2 .and. div(u(t)) > 0) {
   store p(t-1)
   status = 0
}
```

FIG. 3.6. Collapse detector algorithm.

4 Capabilities of a Homogenous Mixture Model to Predict Collapse Situations

Cavitating flows are characterized by a variety of length scales. The hydrofoil shown in FIG. 4.1 (a) has a cord length of about 10 mm, while the diameter of individual bubbles in the vapor cloud near the trailing edge is several orders of magnitude smaller. Discretizing such a flow by explicitly resolving each individual bubble leads to a huge amount of computational cells and extensive numerical cost. With the homogenous mixture model applied in this work it is possible to resolve large-scale cavitation structures while individual bubbles are usually under-resolved. FIG. 4.1 (b) shows a cut through a simulated flow field comparable to FIG. 4.1 (a). The vapor cloud near the trailing edge is macroscopically resolved and individual bubbles are represented as disperse mixture. In the following chapter it is investigated whether the collapse of a fully resolved cloud strongly differs from the collapse of an under-resolved disperse vapor structure. The applied homogenous mixture model in conjunction with the inviscid flow modelling used in this work does not contain a limiting length scale. The only limiting length scale is introduced by the numerical grid. Thus, the influence of spatial resolution is addressed by grid studies.

Parts of the results presented in the following chapter have been published in conference proceedings and book chapters. Parts of section 4.2.1 were published in Ref. 71. Parts of section 4.2.2 and 4.2.3 were published in Refs. 23 and 73.

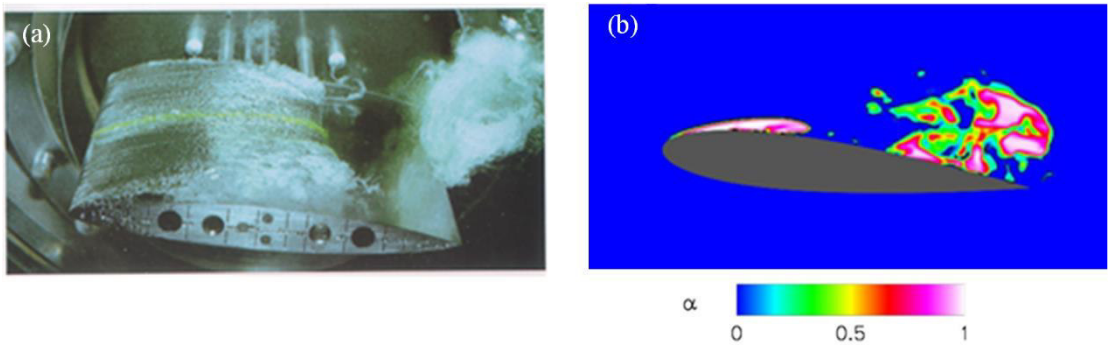

FIG. 4.1. (a) Experiment of a cavitating flow around a hydrofoil. Reprint with permission from Ref. 42. Copyright 1985 Cambridge University Press. (b) Simulation of a cavitating flow similar to (a), contour represents vapor volume fraction.

4.1 Cloud Generation and Numerical Setup

We define an artificial cloud of vapor bubbles as shown in FIG. 4.2, which collapses under an ambient pressure of p_∞=40 bar at an ambient temperature T_{ref}=293 K. The cloud consists of 125 spherical vapor bubbles surrounded by liquid. Bubbles do not intersect and have a minimum distance of 0.2 mm. In the center of the cloud, bubbles are bigger and are packed more densely. Radii of individual bubbles

range from R_{min}≈0.70 mm to R_{max}≈1.65 mm, with an average radius of $\overline{R}$≈0.95 mm. The distribution in size and space is listed in appendix 10.1. An initial radius of the overall cloud can be defined as $A_{c,0}$=10 mm. The corresponding initial vapor volume fraction of the cloud is $\alpha_{c,0}$=11,7 %. With respect to the cloud interaction parameter β[38]

$$\beta = \alpha_{c,0}\left(\frac{A_{c,0}}{\overline{R}}\right)^2 = 13.9 >> 1 \tag{4.1}$$

the setup is chosen such that a strong interaction of individual bubbles within the cloud is expected. The cloud is positioned in a cubic domain of 20x20x20 mm³, referred to as inner domain, with a solid wall at the bottom (z=0). This inner domain is embedded into a larger rectangular outer domain of 4x4x2 m³, see FIG. 4.3. With the speed of sound in water c≈1500 m/s, pressure waves originating from the small domain travel approximately $13\cdot10^{-3}$ s to the boundary of this outer domain. As the simulation time is about 2 orders of magnitude smaller (see next section), the outer domain acts as a non-reflecting boundary condition and its boundaries can be treated as solid walls.

The cloud is mapped to different numerical grids. The procedure is as follows: cells entirely outside of a bubble are given the state ‘outside’. Analogously, cells completely within a bubble are given the state ‘inside’. All remaining cells are ‘cut-cells’ with respect to a bubble surface (a bubble being entirely inside a cell is a special case occurring at coarse resolutions). With the applied thermodynamic modelling, neither a complete evaporation of pure liquid, nor a total condensation of pure vapor is possible (see chapter 3.3.4). We thus initialize all ‘inside’ cells with a high vapor content of $\alpha_{num,0}$=0.95. All ‘cut-cells’ are consequently initialized with $\alpha_{num,0}$=0.95$\cdot V_{c,inside}/V_c$, where $V_{c,inside}/V_c$ is the fraction of the cell-volume, that is inside of a bubble. The density of all ‘inside’ and ‘cut-cells’ is computed with the saturation densities of pure liquid and vapor, $\rho_{sat,l}$ and $\rho_{sat,v}$ respectively

$$\tilde{\rho}(\alpha) = \alpha_{num,0}\rho_{sat,v}(T_{ref}) + (1-\alpha_{num,0})\rho_{sat,l}(T_{ref})\,. \tag{4.2}$$

The pressure in these cells is defined by the equation of state $p = f(\tilde{\rho})$. All ‘outside’ cells correspond to pure liquid. To avoid wave-dynamics induced by the initial condition, we solve a Laplace-equation Δp=0 for the pressure field in these cells with the constrains of p=p_{sat} in all ‘inner’ and ‘cut-cells’ and p=p_∞ in cells at the outer boundary of the outer domain. The velocity field is initially at rest.

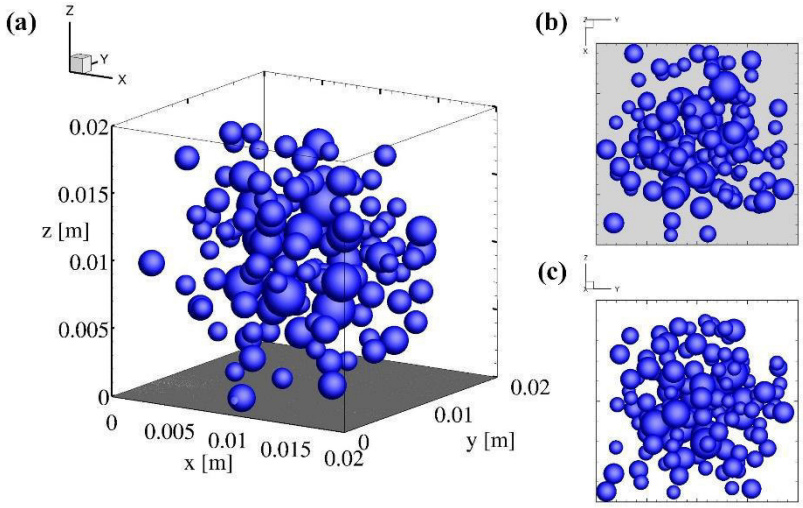

FIG. 4.2. Cloud with 125 spherical non-intersecting vapor bubbles within the small cubic domain of 20^3 mm³. The lower boundary at z=0 is modeled as solid wall. (a) Perspective view. (b) Top view. (c) Side view.

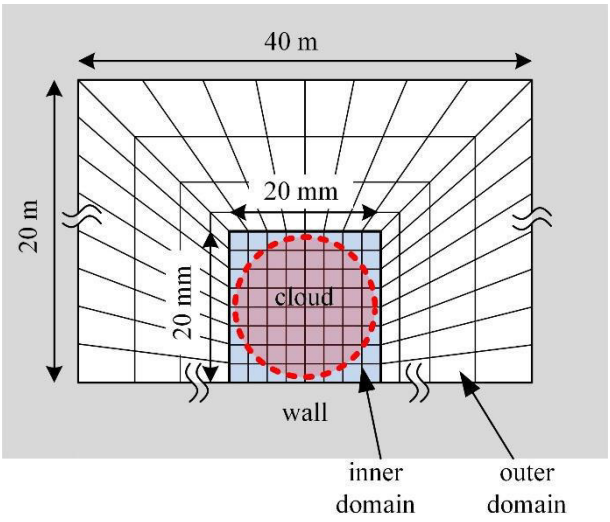

FIG. 4.3. Computational domain.

We apply a series of different spatial resolutions. For the reference configuration, grid I, the inner domain consists of $440^3 \approx 85 \cdot 10^6$ homogenously spaced cells, resulting in a characteristic cell length Δ_{CFD}=0.046 mm. The outer domain is discretized by approximately $35 \cdot 10^6$ cells with exponentially increasing spacing towards the outer boundary. Grid II originates from grid I by halving the number of cells in each dimension and thus consists of 220^3 cells in the inner domain. In total we apply seven grids by consequently applying coarse graining, see Table II. The numerical time-step approximately doubles with each grid level and varies about two orders of magnitude from $\Delta t_{CFD} \approx 9.4 \cdot 10^{-9}$ s (grid I) to $\Delta t_{CFD} \approx 6.8 \cdot 10^{-7}$ s (grid VII).

Figure 4.4 shows the resulting grid-dependent representation of the cloud. Grid I resolves individual bubbles with ≈30-70 cells over the diameter (ψ≈30-72) and ≈15000-200000 cells per bubble, depending

on the bubble-size. Each bubble is thus fully resolved. For grids II and III all individual bubbles are still resolved (ψ>>1). Beginning with grid IV, neighboring bubbles start to merge into under-resolved clusters. Finally, on grid VI and VII, the cloud is completely under-resolved and represented as a disperse vapor pattern ($\psi \leq 1$).

Table II: Parameters of the numerical grids.

	Resolution	Number of cells	Δ_{CFD}	$\psi := \Delta_{flow}/\Delta_{CFD}$
grid I	440^3	$440^3 \approx 8.5 \cdot 10^7$	0.046 mm	≈ 30 - 72
grid II	220^3	$220^3 \approx 1.1 \cdot 10^7$	0.091 mm	≈ 15 – 36
grid III	110^3	$110^3 \approx 1.3 \cdot 10^6$	0.18 mm	≈ 8 – 18
grid IV	55^3	$55^3 \approx 1.7 \cdot 10^5$	0.36 mm	≈ 4 – 9
grid V	28^3	$28^3 \approx 2.2 \cdot 10^4$	0.71 mm	≈ 2 – 5
grid VI	14^3	$14^3 \approx 2.7 \cdot 10^3$	1.43 mm	≈ 1 – 2
grid VII	7^3	$7^3 \approx 3.4 \cdot 10^2$	2.86 mm	≈ 0.5 – 1

To analyze impact-loads we record spatially averaged pressure data at the wall. We define two numerical pressure sensors at the center of the wall of the inner domain. They are of rectangular shape, covering an area of 1x1 mm^2 and 10x10 mm^2 respectively. The pressure on each sensor is averaged at each timestep, resulting in average sampling frequencies between $1.1 \cdot 10^8$ Hz (grid I) and $1.5 \cdot 10^6$ Hz (grid VII).

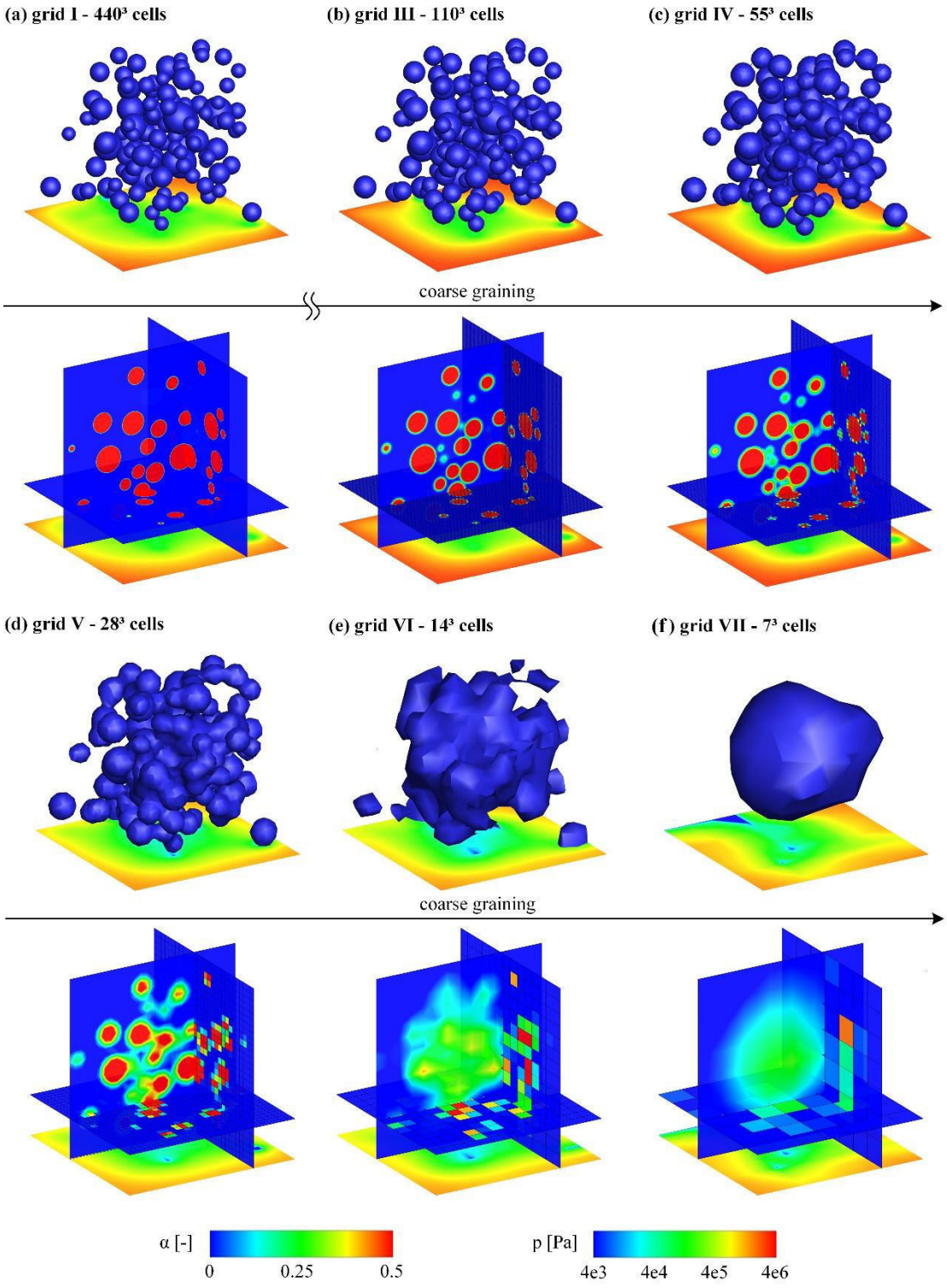

FIG. 4.4. Representation of the cloud on different numerical grids. Iso-surfaces (upper row, $\alpha = 0.5$), and cut-planes (lower row, contour) of the vapor volume fraction. Bottom plane shows the initial pressure field.

4.2 Results

In the following section, the results of the grid-study are presented. First we discuss general collapse characteristics computed on the reference configuration (grid I). The influence of spatial resolution on general collapse characteristics is discussed in the second section, impact-related quantities are discussed in detail in the third section.

4.2.1 Reference Solution

The progress of the collapse can be characterized by the time-evolution of the total vapor volume $V_v(t)$. For further analysis, we define an equivalent radius $R_{equiv.}(t)$

$$R_{equiv.}(t) = \sqrt[3]{\frac{3}{4\pi} V_v(t)}\ , \tag{4.3}$$

which describes the radius of a single bubble with identical vapor volume as the cloud. For the present case, the initial radius is $R_{equiv.}(t=0) \approx 4.81$ mm. FIG. 4.5 (a) shows the time evolution of the dimensionless radius $R_{equiv.}(t)/R_{equiv.}(t=0)$. The radius exhibits a first minimum at $t \approx 67 \cdot 10^{-6}$ s, which is followed by a rebound and a second collapse.

Consecutive time instants corresponding the first collapse of the cloud, indicated in the graph as (a) – (i), are depicted in FIG. 4.6. Instant (a) shows the initial bubble-distribution together with the pressure initialization on the wall. First, outermost bubbles collapse due to the high ambient pressure p_∞ (FIG. 4.6 (b)). Bubbles in an isolated position collapse independently. Instant (b) represents an exemplary chosen time instant, when the emitted shock wave is just registered on the wall. Most Bubbles collapse aspherical and form microjets, which are directed towards to center of the cloud. This behavior is strongly connected to the asymmetric collapse of a single bubble near a solid wall. During the early stages, (a-d), bubbles in the center of the cloud remain in their initial shape. A cut through the velocity field, FIG. 4.7, shows the formation of a global collapse front and its propagation towards the center of the cloud. When the front reaches a bubble a collapse is initiated. In FIG. 4.6 (c) and (d) shock waves from single bubble collapses are registered at the wall. Additionally, the inertia of the global velocity field leads to an increasing pressure behind the collapse front, see (d) and (e). The maximum pressure in the field is recorded when the front reaches the collapse center at $t \approx 65 \cdot 10^{-6}$ s, FIG. 4.6 (f). When the emitted shock wave reaches the wall, FIG. 4.6 (g), rebounding vapor structures are observed, which lead to a second collapse, see (g-i).

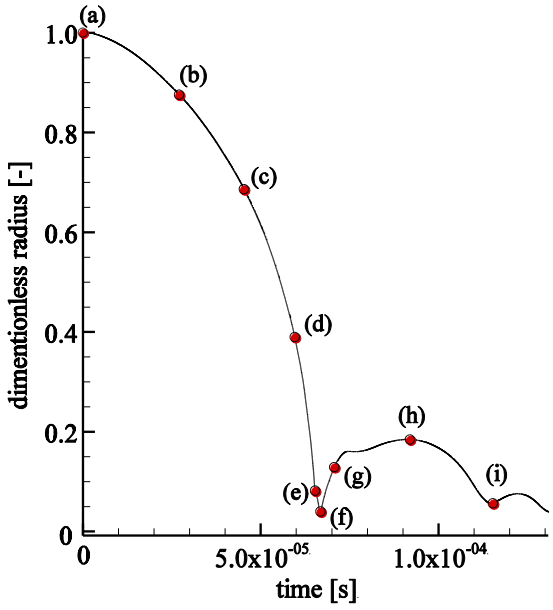

FIG. 4.5. Time evolution of dimensionless equivalent radius $R_{equiv.}(t)/R_{equiv.}(t=0)$ in the reference configuration (grid I). (a-i) correspond to time instants in FIG. 4.6.

FIG. 4.8 shows the time evolution of the equivalent radius and the maximum pressure in the inner domain. As mentioned before, the highest pressure ($t \approx 65 \cdot 10^{-6}$ s) is recorded slightly before the equivalent radius reaches its first minimum ($t \approx 67 \cdot 10^{-6}$ s). As can be seen in FIG. 4.6 (e), rebounds of earlier collapses increase the vapor volume. The emitted shock wave then leads to a collapse of these structures. At the time these earlier rebounds collapse, the main collapse creates a rebound in the focal point. The vapor volume thus exhibits a local minimum, but does not vanish. For further analysis we define the time where the highest pressure is recorded in the field as collapse time $t_{collapse} \approx 65 \cdot 10^{-6}$ s. For the investigated setup, an analytical solution for the collapse time is not available. However, a characteristic collapse time, the so called Rayleigh time, can be approximated with the equivalent radius R_{equiv} by[2]

$$t_{Rayleigh} \approx 0.915 R_{equiv.}(t=0)\sqrt{\frac{\rho_l}{p_\infty - p_{sat}}} \approx 69 \cdot 10^{-6}\, s\,. \tag{4.4}$$

Although $t_{Rayleigh}$ gives an estimate for the collapse duration of a single spherical bubble surrounded by liquid only, it is in good agreement with the collapse duration of the bubble cluster considered here.

The highest pressure recorded in the inner domain is $p_{max} = 9.36 \cdot 10^9$ Pa and lasts for $\Delta t \approx 6 \cdot 10^{-9}$ s ($p > p_{max} \cdot 90\%$). Aside this highest value, two peaks with maximum values of $0.5 \cdot p_{max}$ are recorded. 120 peaks exceed 5% of the maximum pressures. We thus conclude, that the majority of individual bubbles collapse with a relatively low intensity in the propagating collapse front, while few bubbles collapse with a high intensity, when the front reaches the focal point.

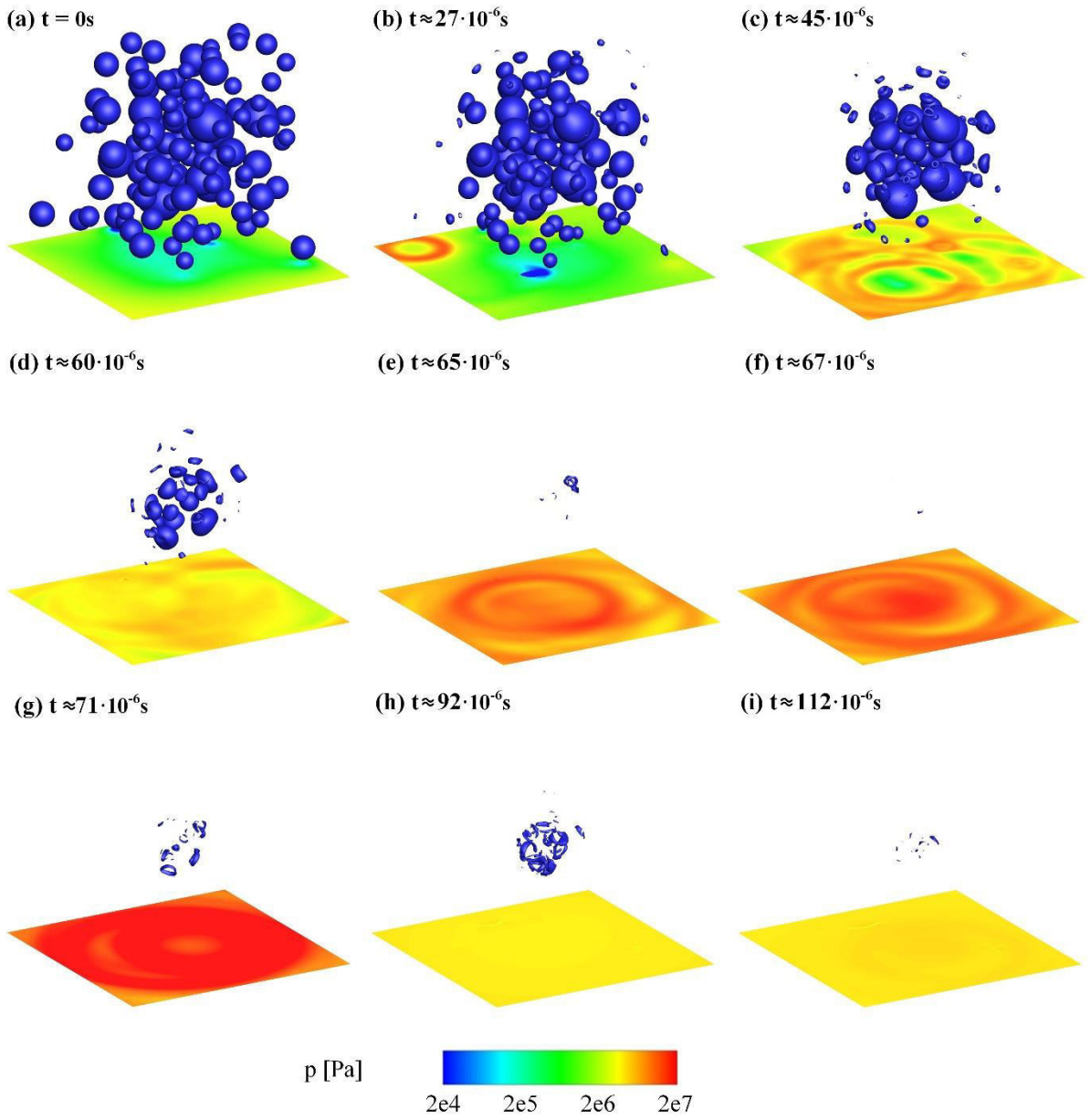

FIG. 4.6. Vapor regimes (iso-surfaces α=0.5) and static pressure on the wall (contour) in subsequent time instants during the collapse (grid I).

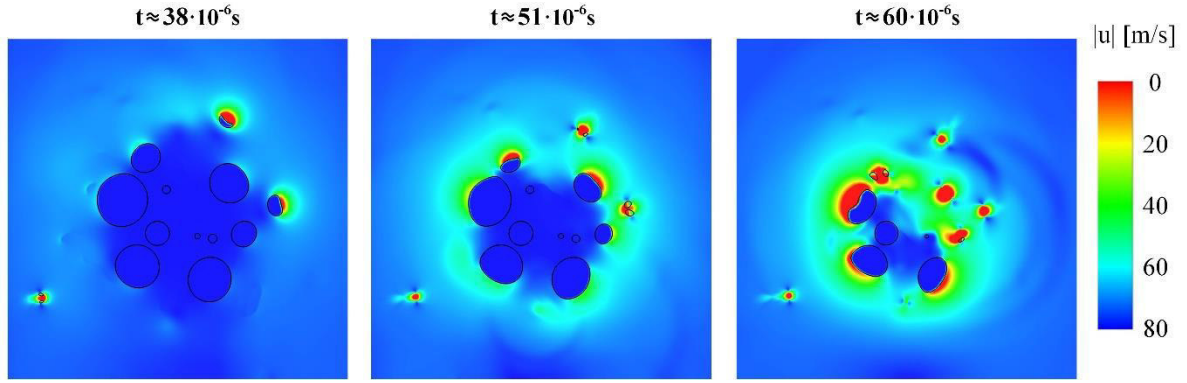

FIG. 4.7. Vapor regimes (iso-lines, α=0.5) and velocity magnitude (contour) on the cut-plane y=10 mm.

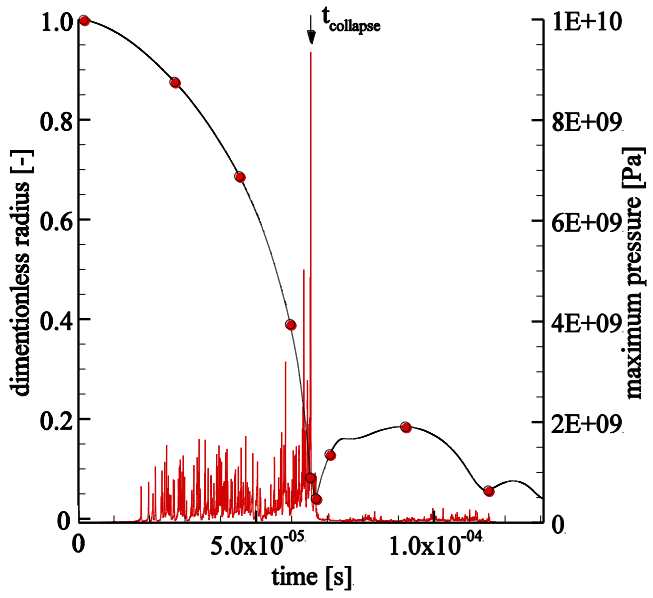

FIG. 4.8. Time evolution of dimensionless equivalent radius $R_{equiv.}(t)/R_{equiv.}(t=0)$ (black line) and the maximum pressure in the inner domain (red line).

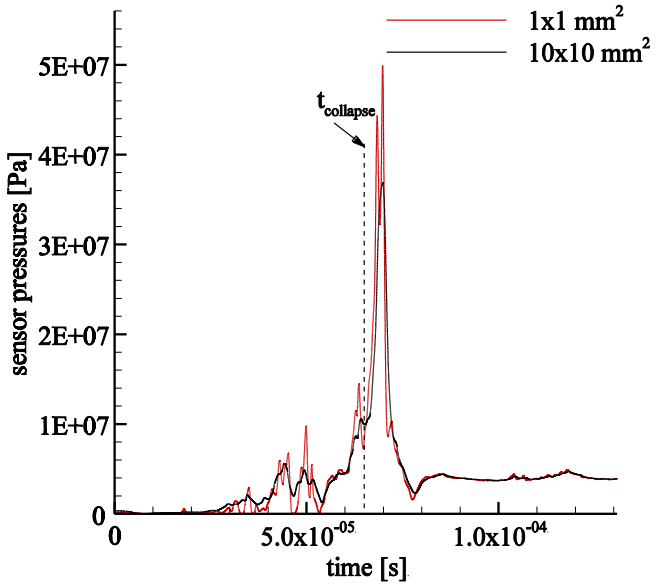

FIG. 4.9. Time evolution of the pressure on two pressure sensors with different size (1x1 mm^2 and 10x10 mm^2).

The output of the pressure sensors on the bottom wall is shown in FIG. 4.9. Two strong collapse events indicated in the plot of the maximum pressure (FIG. 4.8) are also recorded on the small sensor, while on the larger sensor only one peak is registered. The temporal offset corresponds to the propagation time of the pressure wave from the focal point to the wall. Due to the spherical decay of the shock the pressure recorded on the sensor is significantly lower than the maximum pressure at the collapse center. On the larger sensor, the two peaks merge because of spatial averaging.

Both sensors do not record pressures higher than ambient pressure (p_∞=40 bar) before $t \approx 4 \cdot 10^{-5}$ s, although high maximum pressures (>1000 bar) are detected within the field. This is due to the bubbles located just above the sensors, which damp incoming pressure waves. The collapse of these structures then leads to loads on the wall at the location of the sensors for $t > 4 \cdot 10^{-5}$ s, see FIG. 4.6 (c).

4.2.2 Influence of Spatial Resolution on Collapse Characteristics

FIG. 4.10 shows the time evolution of the dimensionless equivalent radius for the different spatial resolutions. From the start of the simulation until the first collapse all grids show a similar behavior. The maximum deviation of the collapse time from the mean value is 5% (grid IV, see Table III). After the first collapse, rebounds are predicted on grids I-IV, while they are not resolved with coarser resolutions (grids V-VII).

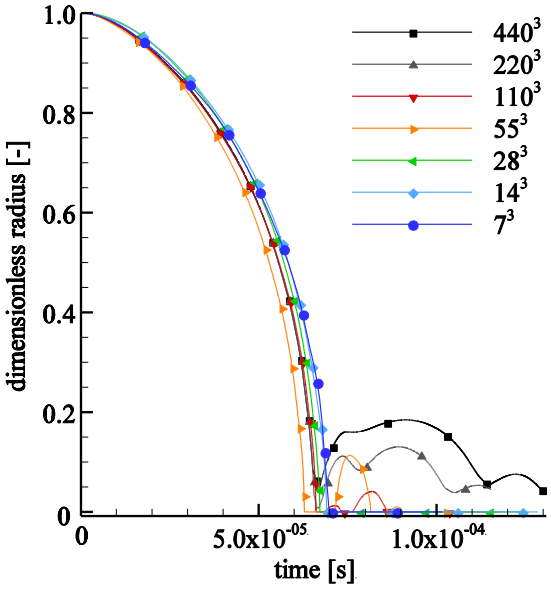

FIG. 4.10. Time evolution of dimensionless equivalent radius $R_{equiv.}(t)/R_{equiv.}(t=0)$. Time instants t_1-t_4 correspond to snapshots in FIG. 4.11.

Iso-surfaces of vapor volume fraction and wall pressure of the marked time instants t_1-t_4 are depicted in FIG. 4.11 for selected grids. FIG. 4.11 (a) shows the reference configuration discussed in the previous chapter. FIG. 4.11 (d) shows the coarsest resolution, (b) and (c) present two intermediate refinement levels. Comparing (a) and (b) demonstrates that small scale information like toroidal rebounds of asymmetrical collapsing single bubble are not representable with a lower spatial resolution. Still some features like isolated collapses (1), or the pattern of collapse-induced pressure waves at the wall (2) are represented. With further coarsening, FIG. 4.11 (c), single bubbles are under-resolved and merge to a single connected vapor pattern. Although a high pressure region connected to (1) can still be recognized,

most of the details are lost. Finally, in FIG. 4.11 (d) only the collapse of a single disperse vapor pattern is resolved.

FIG. 4.12 shows the velocity magnitude on a cut-plane for the third time instant t_3, just before the collapse. The collapse front directed towards the focal point is predicted by all grids. Grid I and III (FIG. 4.11 (a) and (b)) resolve high velocity regimes linked to individual collapse situations. Analogous to the volumetric representation in FIG. 4.11, one observes that small scale information is lost with grid coarsening. Finally on grid VII, FIG. 4.11 (d), only the collapse front is resolved (by approximately two cells).

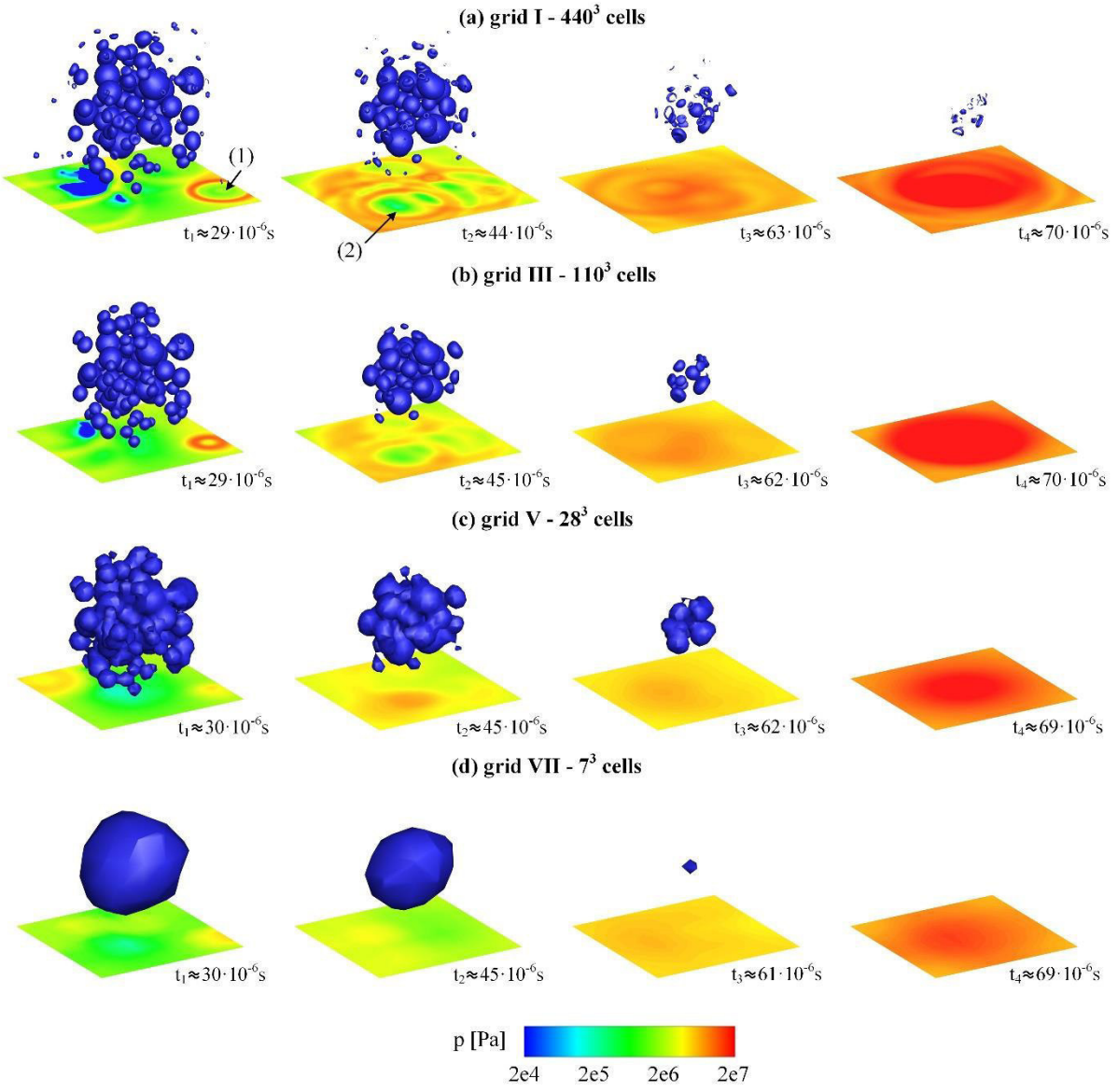

FIG. 4.11. Vapor regimes (iso-surfaces α=0.5) and static pressure on the wall (contour) in subsequent time instants during the collapse. Grid resolution decreases from (a) to (d).

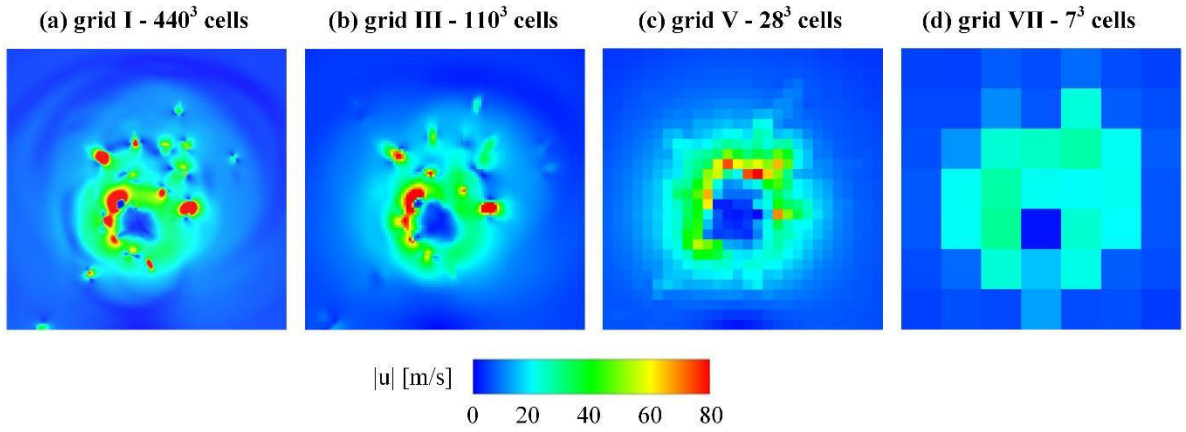

FIG. 4.12. Velocity magnitude in cut-planes (y=10 mm). Grid resolution decreasing from (a) to (d). Time instants correspond to t_3 in FIG. 4.11.

In FIG. 4.13 the time evolution of the kinetic energy E_{kin} is shown. Due to the initialization, E_{kin} is zero at the beginning of the simulation. As long as the liquid accelerates towards the center, E_{kin} increases and the maximum is reached just before the main collapse. During the main collapse, velocity towards the focal point vanishes with the release of the shock wave. This leads to a sharp decrease of E_{kin}. Note that, although the maximum kinetic energy is grid-dependent, the jump in energy caused by the pressure wave, ΔE_{kin}, only weakly depends on grid resolution (maximal deviation from the mean value ≈ 13 %, see Table III and FIG. 4.13). We conclude that while detailed information can not be represented with coarse resolution, the global dynamics of the main collapse are still resolved.

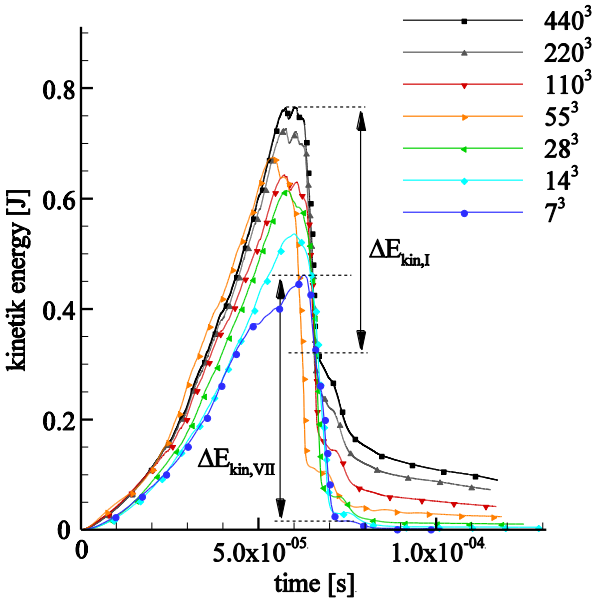

FIG. 4.13. Time evolution of the kinetic energy in the inner domain.

Table III: Comparison of collapse duration $t_{collapse}$ and jump in kinetic energy during the shock ΔE_{kin}.

Resolution	$t_{collapse}$ [s]	ΔE_{kin} [J]	$\Delta E_{kin}/E_{kin,max}$ [%]
440^3	$6.5 \cdot 10^{-5}$	0.45	58
220^3	$6.6 \cdot 10^{-5}$	0.47	65
110^3	$6.6 \cdot 10^{-5}$	0.46	81
55^3	$6.3 \cdot 10^{-5}$	0.55	82
28^3	$6.7 \cdot 10^{-5}$	0.54	88
14^3	$7.0 \cdot 10^{-5}$	0.50	93
7^3	$7.0 \cdot 10^{-5}$	0.45	96

4.2.3 Influence of Spatial Resolution on Impact Quantities

Finally, we analyze the influence of grid resolution on impact quantities of the collapse. We therefore evaluate the maximum pressure in the flow field, time signals of the two numerical pressure sensors, and different definitions of impulse strengths at the wall.

The maximum values of the pressure in the flow field and the pressure measured by two pressure sensors are shown in FIG. 4.14 and summarized in Table IV. The maximum pressure in the field varies about two orders of magnitude. It scales with the inverse of the characteristic cell size Δ_{CFD} ($p \sim 1/\Delta_{CFD}$), as indicated in FIG. 4.14. The maximum pressures on the sensors only show a comparatively weak variation by a factor of ≈ 2.5. To analyze these variations, we derive an analytical relation between the two quantities as proposed in Ref. 74.

We consider the behavior of a linear spherical pressure wave. The amplitude of the wave decays inversely proportional to radius of the wave front, i.e., $p \sim 1/r$. When the wave is reflected at a wall, the amplitude approximately doubles. We assume that the maximum pressure in the field corresponds to the initial amplitude of the wave front. Assuming the collapse occurs at the center of the corresponding computational cell, the initial radius is defined by the cell resolution $\Delta_{CFD}/2$. The maximum pressure on the sensor corresponds to a wave front at a distance D to the origin that just has been reflected at the wall. This leads to

$$\frac{p_{\max,filed}}{p_{\max,sensor}} \approx \frac{D}{\Delta_{CFD}}. \tag{4.5}$$

Values of D are summarized in Table IV for the pressure on the small sensor. Assuming that the collapse is perfectly focused into one fixed point independent of the applied grid, one would expect that D is approximately constant (if nonlinear effects are negligible). All estimates for D are in a reasonable range (5,7 mm < D < 9,9 mm). We conclude that the grid-dependent maximum pressures within the

flow field are not a numerical artifact, but rather represent a physically correct behavior, that is well captured by the applied method.

Table IV: Grid-dependence of impact-quantities.

Resolution	p_{max} (field)	p_{max} (small sensor)	p_{max} (large sensor)	D
440^3	$9.36 \cdot 10^9$ Pa	$5.0 \cdot 10^7$ Pa	$3.7 \cdot 10^7$ Pa	$9{,}9 \cdot 10^{-3}$ m
220^3	$3.78 \cdot 10^9$ Pa	$4.1 \cdot 10^7$ Pa	$3.6 \cdot 10^7$ Pa	$6{,}3 \cdot 10^{-3}$ m
110^3	$1.17 \cdot 10^9$ Pa	$3.9 \cdot 10^7$ Pa	$3.4 \cdot 10^7$ Pa	$6{,}8 \cdot 10^{-3}$ m
55^3	$0.63 \cdot 10^9$ Pa	$3.6 \cdot 10^7$ Pa	$3.2 \cdot 10^7$ Pa	$6{,}4 \cdot 10^{-3}$ m
28^3	$0.34 \cdot 10^9$ Pa	$3.5 \cdot 10^7$ Pa	$3.1 \cdot 10^7$ Pa	$5{,}7 \cdot 10^{-3}$ m
14^3	$0.12 \cdot 10^9$ Pa	$2.8 \cdot 10^7$ Pa	$2.4 \cdot 10^7$ Pa	$7{,}0 \cdot 10^{-3}$ m
7^3	$0.07 \cdot 10^9$ Pa	$1.9 \cdot 10^7$ Pa	$1.7 \cdot 10^7$ Pa	$8{,}5 \cdot 10^{-3}$ m

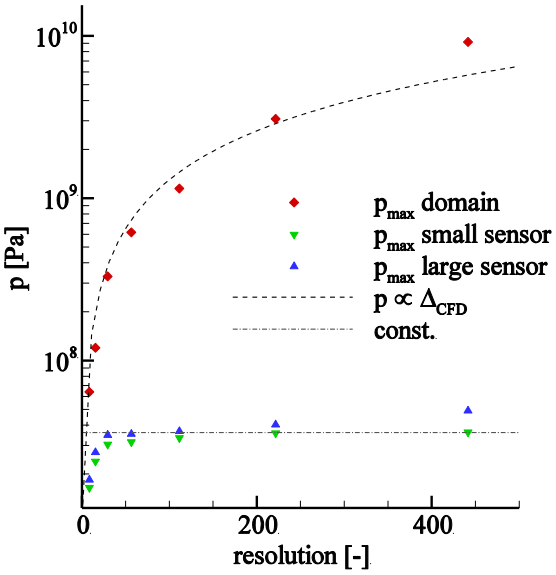

FIG. 4.14. Grid-dependence of the maximum pressure in the field and the maximum pressures on the two sensors.

We now analyze the influence of grid resolution on the impact of the pressure wave on the wall. FIG. 4.15 shows time signals as obtained by the large sensor. In the reference configuration, the impact is represented as a sharp peak with a duration of approximately $5 \cdot 10^{-6}$ s. Comparison with the sensor output acquired on grid II shows that this solution is grid converged. With the lowest resolution, grid VII, the peak has a lower amplitude and is smeared.

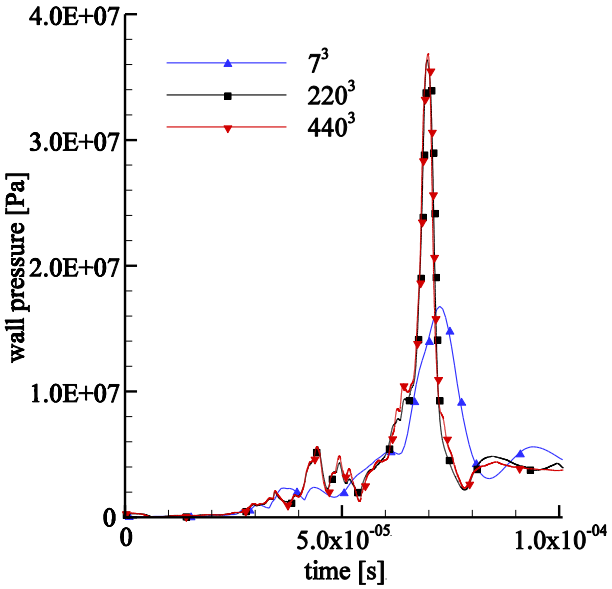

FIG. 4.15. Time evolution of the pressure on the small sensor (1x1 mm^2) for selected grids.

For a quantitative comparison we compute the impulse on the sensors, which is the time integral of the pressure signal. We define three different impulse strengths I_1-I_3, as proposed in Ref. 74

$$I_1 := \int_0^{10^{-4}\,s} p\,dt, \tag{4.6}$$

$$I_2 := \int_{5\cdot10^{-5}\,s}^{8.5\cdot10^{-5}\,s} p\,dt, \tag{4.7}$$

$$I_3 := \int_0^{10^{-4}\,s} \begin{Bmatrix} p \;for\; p > 80bar \\ 0 \;for\; p \le 80bar \end{Bmatrix} dt\,. \tag{4.8}$$

I_1 covers the entire collapse. I_2 approximately includes the time interval where the peak pressure from the main collapse of the cloud is observed. I_3 is obtained by integrating the pressure only during the time where the pressure exceeds 80 bar (twice the far-field pressure). I_1-I_3 are shown for both pressure sensors in FIG. 4.16. All Impulse strengths only show a weak scatter for different spatial resolutions. For I_1 and I_2 all variations are smaller than 5% of the mean value, the highest variation of I_3 is ≈ 11% of the mean value for the small sensor and grid IV.

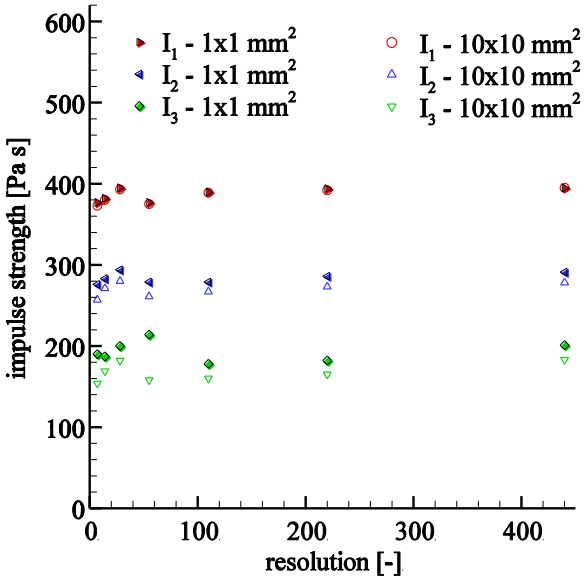

FIG. 4.16. Impulse strengths I_1, I_2, and I_3 for both pressure sensors (1x1 mm^2 and 10x10 mm^2).

Integral quantities analyzed so far show that the strength of the pressure wave induced by the main collapse can be predicted reasonably well even with coarse resolution. Only the pressure at the focal point shows significant grid-dependence. Eq. 4.5 demonstrates, that this pressure can be interpreted as the amplitude of a collapse-induced wave. The distance to the collapse center is defined by the cell size. To account for this grid resolution effect we introduce a scaled collapse pressure p_{scale} at a reference length scale $x_{ref,p}$. We define the cube root of the volume V_{cell} of the cell where the collapse was detected as characteristic cell size. Thus we obtain

$$p_{scale} = \frac{\sqrt[3]{V_{cell}}}{x_{ref,p}} p_{collapse}, \tag{4.9}$$

where, at this point, $x_{ref,p}$ is a parameter that requires calibration.

4.2.4 Effect of Thermodynamic Modelling

To investigate the influence of thermodynamic modelling, calculations on grids II - VII have been performed with a thermodynamic model for comparison, taking into account the energy equation (see section 3.3.1). The numerical setup remains unchanged, see section 4.1. Within the entire domain (fluid and bubbles) the initial temperature is $T(t=0)=T_{ref}=293$ K.

The characteristic behavior of the vapor phase can be studied by the equivalent radius (Eq. 4.3), see FIG. 4.17. Due to the high density, the characteristic behavior of the liquid phase can be evaluated by means of kinetic energy, see FIG. 4.18. For both quantities a slight influence of the thermodynamic

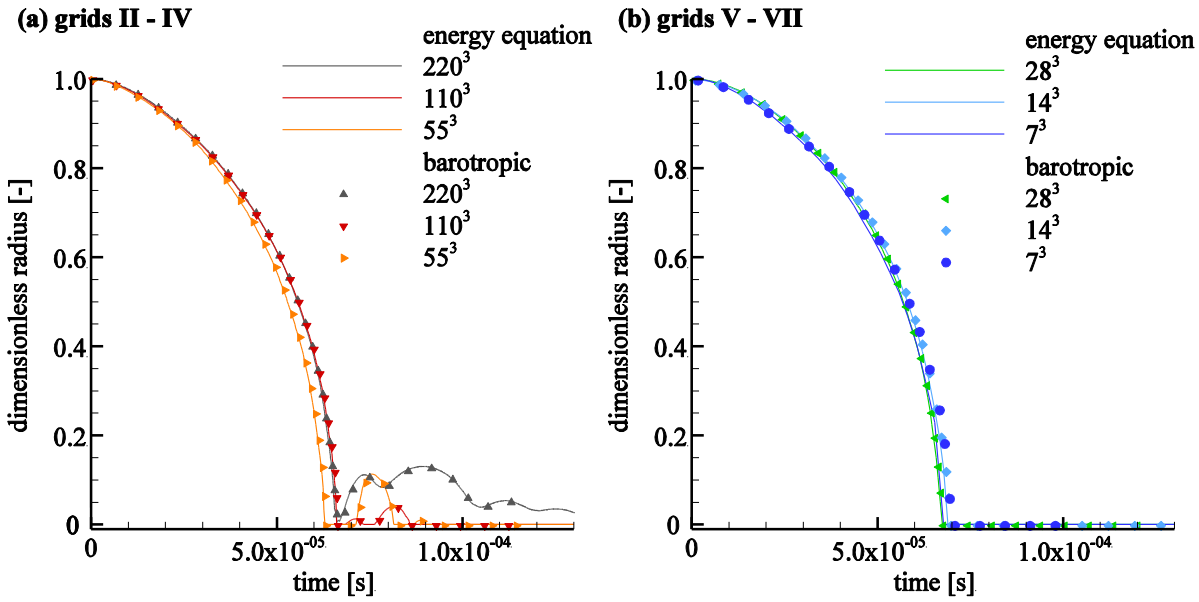

FIG. 4.17. Time evolution of dimensionless equivalent radius $R_{equiv.}(t)/R_{equiv.}(t=0)$ for barotropic calculations (symbols) and calculations with energy equation (lines). (a) grids II – IV. (b) grids V – VII.

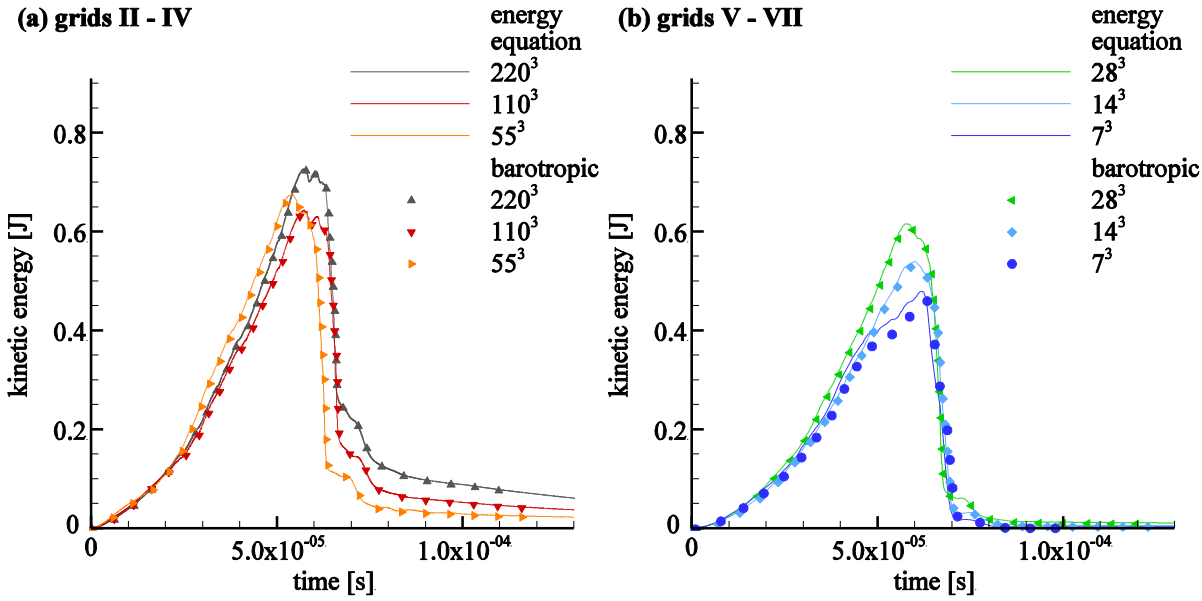

FIG. 4.18. Time evolution of the kinetic energy in the inner domain for barotropic calculations (symbols) and calculations with energy equation (lines). (a) grids II – IV. (b) grids V – VII.

model is present for the coarsest resolution, grid VII. For the remaining grids, grid II – grid VI, no influence of the thermodynamic model is visible.

Table V summarizes the relative deviation of impact quantities for each resolution $\Delta(p)$. The highest deviations between both models occur on the coarsest resolution and are approximately 3.4% for the maximum pressure in the fluid domain and about 2.3% for the maximum pressures on the two sensors.

The remaining grids show lower deviations (<1.5% for p_{max} in the fluid and <0.4% for p_{max} on the two sensors). In summary, taking the energy equation into account only has a minor influence on the main characteristics of the collapse.

Table V: Relative deviation of impact quantities calculated with barotropic modelling and with energy equation respectively.

Resolution	$\Delta(p_{max}$(field))	$\Delta(p_{max}$(small sensor))	$\Delta(p_{max}$(large sensor))
220^3	-1.18 %	0.29 %	0.13 %
110^3	0.54 %	0.12 %	0.19 %
55^3	0.15 %	0.17 %	0.16 %
28^3	-0.20 %	0.15 %	0.21 %
14^3	1.40 %	0.38 %	0.13 %
7^3	3.42 %	2.30 %	2.27 %

4.3 Conclusion

The collapse of a resolved dense cloud of bubbles is closely related to the collapse of an under-resolved vapor volume fraction distribution. Collapse times are almost identical. While the kinetic energy in the entire domain increases with resolution, the amount of kinetic energy, which is decreased due to the shock formation and propagation of the main collapse, is approximately constant. Same holds for the pressure and impulse strength at some distance to the collapse center. The collapse of a given vapor volume fraction leads to a grid-dependent instantaneous maximum pressure. However, the grid-dependence is linear to good approximation. A scaling law to account for this grid resolution effect is introduced, see Eq. (4.9). The law is based on the decay of a linear spherical wave and incorporates a reference length scale $x_{ref,p}$, which will be further discussed in chapter 5.6 and is a parameter at this point. Finally, comparison of barotropic calculations with calculations with full thermodynamic treatment show only a minor influence of the thermodynamic modelling on the collapse behavior.

In conclusion, the homogeneous mixture approach is suitable for predicting important characteristics of potentially erosive collapses of a given vapor-structure, even if actual vapor-structures are under-resolved.

5 Capabilities of a Homogenous Mixture Model to Predict Hydrodynamic Cavitation

In the preceding chapter, the predictive capabilities of a homogeneous mixture model for the collapse of a vapor cloud was investigated. Location and amount of vapor, as well as the initial pressure and velocity field were part of the initialization. In hydrodynamic cavitation all these properties are part of the solution and interdepend. In the following chapter, the predictive capabilities of a homogeneous mixture model for hydrodynamic cavitation are under consideration. As testcase we choose a setup where evaporation is initiated by a geometrically induced acceleration of the liquid, and that features a shedding instability. As the only limiting length scale is introduced by the numerical grid, the influence of spatial resolution is again of special interest.

Most parts of this chapter have been published in Ref. 37. Preliminary investigations have been published in Refs. 72 and 73-75.

5.1 Test Case and Numerical Setup

The numerical setup reproduces a reference experiment as described in detail in Ref. 35. Experimental data is provided in Refs. 35 and 76. The axisymmetric configuration consists of a nozzle, directed onto a target, and forming a radially divergent gap. A cross section is sketched in FIG. 5.1 (a). At the exit of the nozzle, the fluid accelerates along a small radius and forms an unsteady toroidal cavitation pocket. The cavitation number σ has been defined for nozzle flows in Eq. 2.3 as

$$\sigma = \frac{p_{exit} - p_{sat}}{p_{in} - p_{exit}} \tag{5.1}$$

with the pressure in front of the contraction of the nozzle p_{in}, the pressure downstream of the cavity p_{exit}, and the vapor pressure p_{sat}.[35] Different operating conditions have been investigated with a constant value of $\sigma = 0.9$ which result in different pressure levels and flow rates, while the radial extent of the cavity remains constant.[35] Near the closure region of the cavity, pitting at the target surface (referred to as "lower wall", FIG. 5.1(b)) was observed in a ring-shaped area at $19 \cdot 10^{-3}$ m $< r < 32 \cdot 10^{-3}$ m (position 1).[35] Additionally, two areas of material damage have been reported on the opposite side of the gap (referred to as "upper wall", FIG. 5.1(c)) at $r = 11 \cdot 10^{-3}$ m (position 3) and $17 \cdot 10^{-3}$ m $< r < 27 \cdot 10^{-3}$ m (position 2).[76] A pressure sensor was flush mounted on the lower wall at $r = 24.5 \cdot 10^{-3}$ m; this corresponds to the location where the cavitating flow was found to be most aggressive.[8] The sensor area was circular, with a diameter of $3.6 \cdot 10^{-3}$ m, the temporal resolution was approximately $2 \cdot 10^{6}$ Hz[8].

Proper representation of viscous wall layers can be an important aspect for the prediction of internal flows. In the present case flow dynamics in the cavitating part of the gap are dominated by a shedding mechanism, which is an inviscid instability.[21] Additionally, the axis symmetric setup does not promote

the formation of geometrically induced secondary flow structures such as corner vortices, as observed e.g. in Ref. (64). As our focus is on simulation of the cavity dynamics and resulting collapse events, we conclude that an inviscid flow model is sufficient. This modeling choice is supported by comparison with experimental data in part 5.2, 5.3, and 5.4.

FIG. 5.2 shows a cut through the computational domain which represents the experimental geometry.

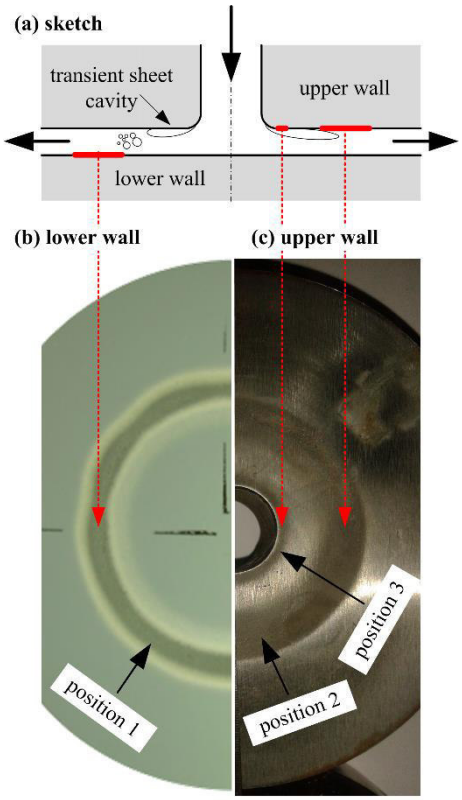

FIG. 5.1. (a) Sketch of the axisymmetric experimental setup. (b) Material damage at the lower wall (position 1: $19 \cdot 10^{-3}$ m < r < $32 \cdot 10^{-3}$ m). (c) Material damage at the upper wall (position 3: $r = 11 \cdot 10^{-3}$ m; position 2: $17 \cdot 10^{-3}$ m < r < $27 \cdot 10^{-3}$ m)[76]. (a) and (c) reprint with permission from Ref. 37. Copyright 2015 by AIP Publishing. (b) Reprint with permission from Ref. 35. Copyright 2009 by ASME.

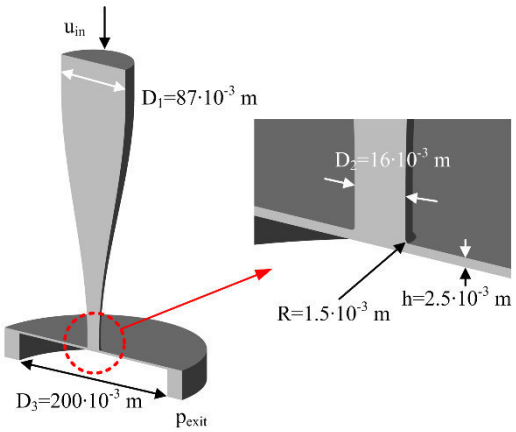

FIG. 5.2. Cut through the numerical setup. All solid boundaries are treated as adiabatic slip walls. The simulation is performed on the full 360° domain. Fluid is water at T = 293K. Reprint with permission from Ref. 37. Copyright 2015 by AIP Publishing.

At the inlet, we prescribe a uniform velocity, which is calculated from the experimental mass flux. An asymptotic pressure-boundary condition is imposed at the axial exit of a circular reservoir attached at a radial distance of $100 \cdot 10^{-3}$ m. We impose the static pressure measured in the experiment downstream of the entire setup. The working fluid is water at a temperature $T = 293$K. All solid boundaries are treated as adiabatic slip walls. We consider three operating conditions at different pressure levels. In the following, the operating conditions are identified by the stagnation pressure of the incoming flow ("10 bar", "20 bar", "40 bar"). Corresponding boundary conditions are listed in Table VI.

Table VI: Boundary conditions.

operating condition	10 bar	20 bar	40 bar
u_{in} [m/s]	0.668	0.956	1.37
p_{out} [bar]	4.80	9.42	18.9

To assess the effect of spatial resolution we perform a grid-resolution study. We use three grids for each operating condition: "coarse" ($6.3 \cdot 10^4$ cells), "medium" ($5.0 \cdot 10^5$ cells), and "fine" ($4.0 \cdot 10^6$ cells). Each grid is divided into 152 blocks. It results from the next coarser one by dividing each cell-edge by 2. Hence, for each refinement step the number of cells grows by a factor of 8, while the numerical time step reduces by a factor 0.5. Parameters of the three setups are summarized in Table VII.

Table VII: Parameters of the Computations.

Grid	coarse	medium	fine
Numerical time-step	$7.0 \cdot 10^{-8}$ s	$3.3 \cdot 10^{-8}$ s	$1.6 \cdot 10^{-8}$ s
Simulated physical time	≈ 2.1 s	≈ 0.25 s	≈ 0.039 s

We collect pressure data averaged over an area, which matches the experimental pressure sensor area. We place these numerical pressure sensors at radial positions $r = 24.5 \cdot 10^{-3}$ m, $r = 26.0 \cdot 10^{-3}$ m, and $r = 27.5 \cdot 10^{-3}$ m. For each sensor position, we equally distribute four numerical pressure sensors in circumferential direction, resulting in 12 numerical sensors in total. The force on each sensor is calculated at each timestep, resulting in sampling frequencies of (coarse to fine) $14 \cdot 10^6$ Hz, $30 \cdot 10^6$ Hz, and $62 \cdot 10^6$ Hz.

5.2 Flow Dynamics and Shedding Mechanism

In the experiment, the lower wall was exchanged by a glass window for optical accessibility, see FIG. 5.3. FIG. 5.4 compares instantaneous cavitation structures in experiment and simulation. In the simulation, vapor regions are indicated by iso-surfaces of the vapor volume fraction (α = 10%, i.e., $\geq$ 10% of the cell-volume is vapor). At the nozzle exit unsteady sheet cavities develop. The dynamics of these cavities is governed by a periodic shedding mechanism, see chapter 2.2. At the beginning of a period, an attached sheet grows in radial direction (FIG. 5.4 (1)). The sheet detaches by reverse liquid flow at the upper wall. The detached cavity is advected further in outward direction as a circumferential vortex. Vortex breakup leads to fragmentation (FIG. 5.4 (2)). The subsequent collapse (FIG. 5.4 (3)) is induced by the positive radial pressure gradient.

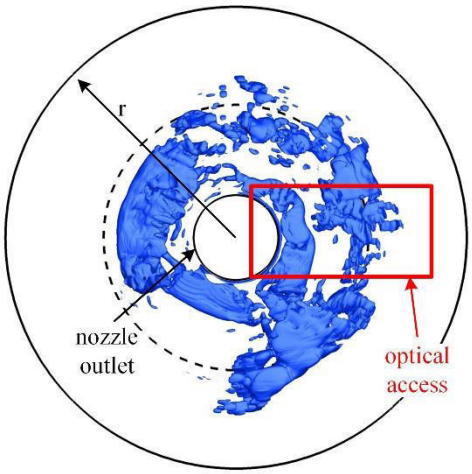

FIG. 5.3. Position of the optical access in the experiment. The perspective is along the nozzle axis in flow direction. The dashed circle marks $r = 25 \cdot 10^{-3}$ m.

Structures from different stages of subsequent shedding cycles interact with each other, resulting in a strong non-uniformity in circumferential direction. FIG. 5.5 shows cavitation structures in the whole gap at four consecutive single time instants ($\Delta t \approx 7.4 \cdot 10^{-5}$ s) as obtained with different spatial resolutions. At all grid resolutions the evolution phenomena of the shedding mechanism (i.e., (1) growth of an attached cavitation sheet, (2) fragmentation, (3) collapse) are reproduced. As the spatial resolution determines the scale of the smallest representable vapor structures we observe the recovery of increasingly fine structures with grid refinement.

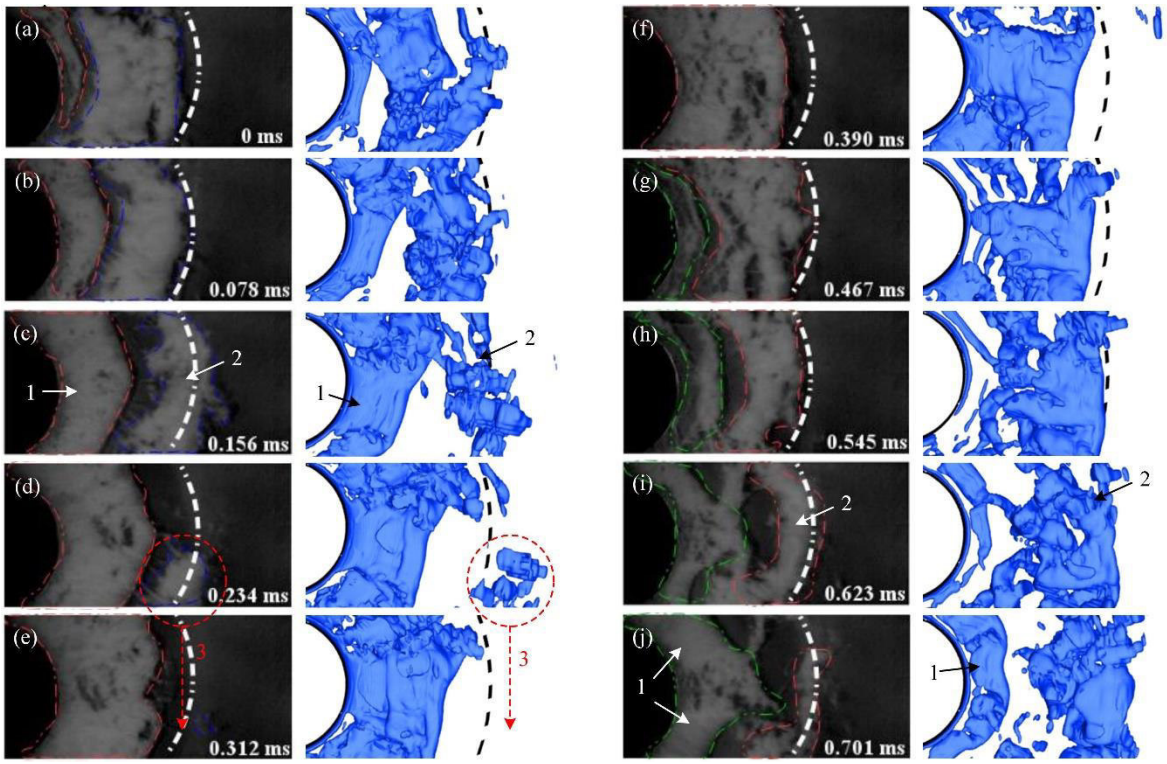

FIG. 5.4. Cavitation structures in experiment (photographs) and simulation (iso-surfaces of the vapor volume fraction, i.e., $\alpha \geq 10\%$) at consecutive time instants. Experiment and simulation show consecutive stages of the periodic shedding, e.g.: (1) Growth of an attached cavitation sheet. (2) Fragmentation of detached cavitation structures. (3) Collapse. Experimental pictures (left row in (a)-(i)) reprinted with permission from Ref 76. Copyright 2015 by Elsevier.

While FIG. 5.4 and FIG. 5.5 cover the time-scales of the dominant shedding mechanism, FIG. 5.6 shows consecutive time instants of a collapse situation at a higher time resolution. Additional to vapor structures (iso-surfaces of the vapor volume fraction), the static pressure on the lower wall is depicted as a contour. In FIG. 5.6 (a), a cavitation structure has detached in the end of a shedding cycle and is advected outwards in radial direction (290°). At the same circumferential position, an attached cavity already develops, initiating the next shedding period. Additionally, at 240° the pressure wave of a previous collapse impinges on the lower wall. The collapse of the detached vapor structure is accompanied by further fragmentation. After $5.7 \cdot 10^{-5}$ s, FIG. 5.6 (b), a first fragment has collapsed; the propagation of the subsequent shock wave on the wall is clearly visible in the static pressure field, FIG. 5.6 (b-c). The collapse of a second fragment is amplified by the pressure wave of the first collapse; this results in a higher collapse pressure and a stronger shock (FIG. 9 c-d). Note that the compressible treatment of the fluid and the high temporal resolution in the simulation are necessary requirements for resolving such an interaction. The remaining flow field (0°-200°), which changes on the time-scale of the shedding mechanism, remains essentially unaltered during the shown collapse situation.

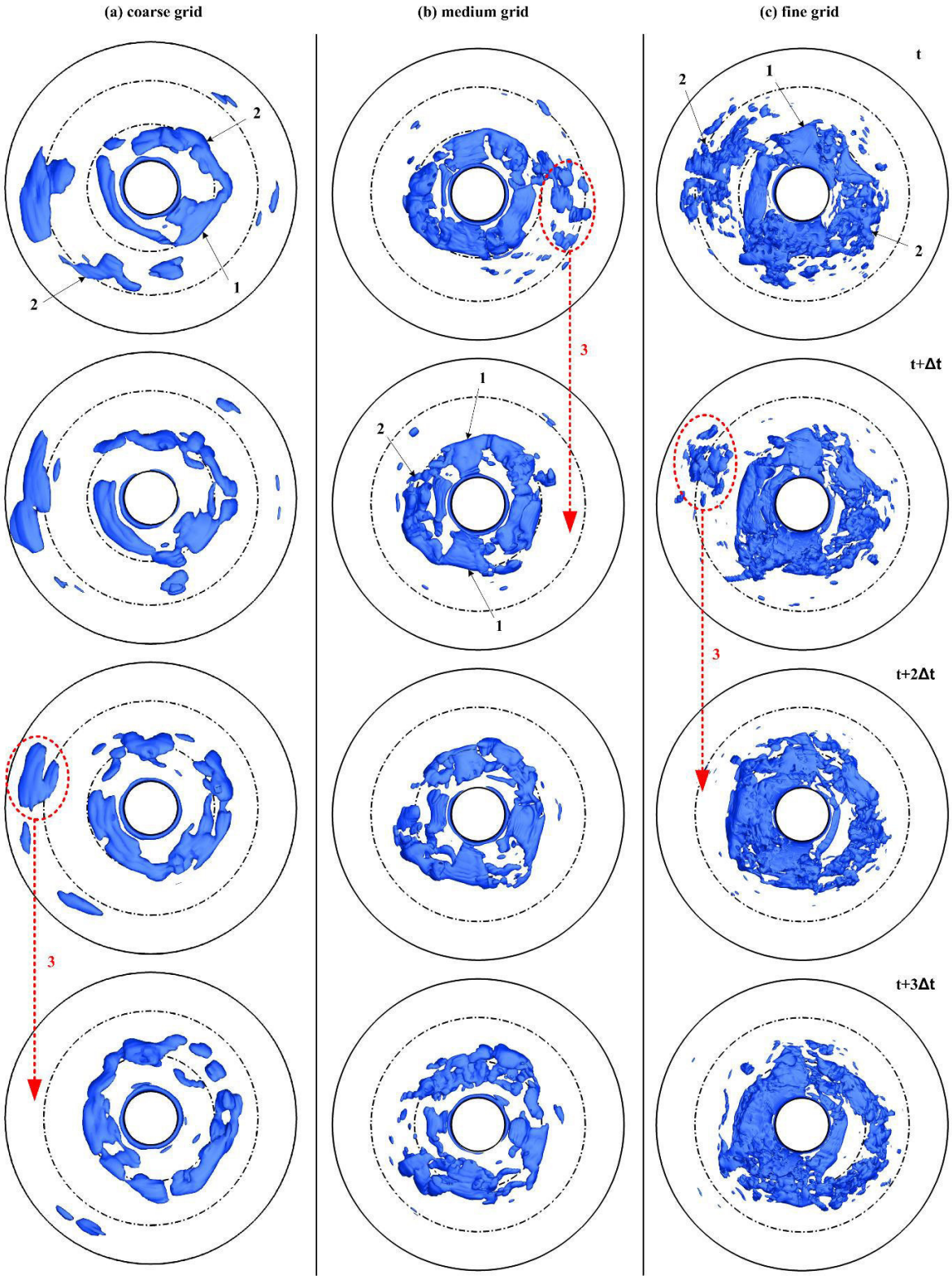

FIG. 5.5. Iso-surfaces of the vapor volume fraction ($\alpha \geq 10\%$) at consecutive time instants ($\Delta t \approx 7.4 \cdot 10^{-5}$ s) for three different spatial resolutions of the 40 bar case. The perspective is along the nozzle axis in flow direction. (a) coarse grid. (b) medium grid. (c) fine grid. The inner solid circle marks the diameter of the nozzle outlet ($r = 8 \cdot 10^{-3}$ m), the outer solid circle marks the size of the target ($r = 50 \cdot 10^{-3}$ m). Dash-dotted lines indicate the area where pitting was observed in the experiment. Each snapshot shows different stages of the periodic shedding mechanism at different circumferential positions, e.g.: (1) Growth of an attached cavitation sheet. (2) Fragmentation of detached cavitation structures. (3) Collapse. Reprint with permission from Ref. 37. Copyright 2015 by AIP Publishing.

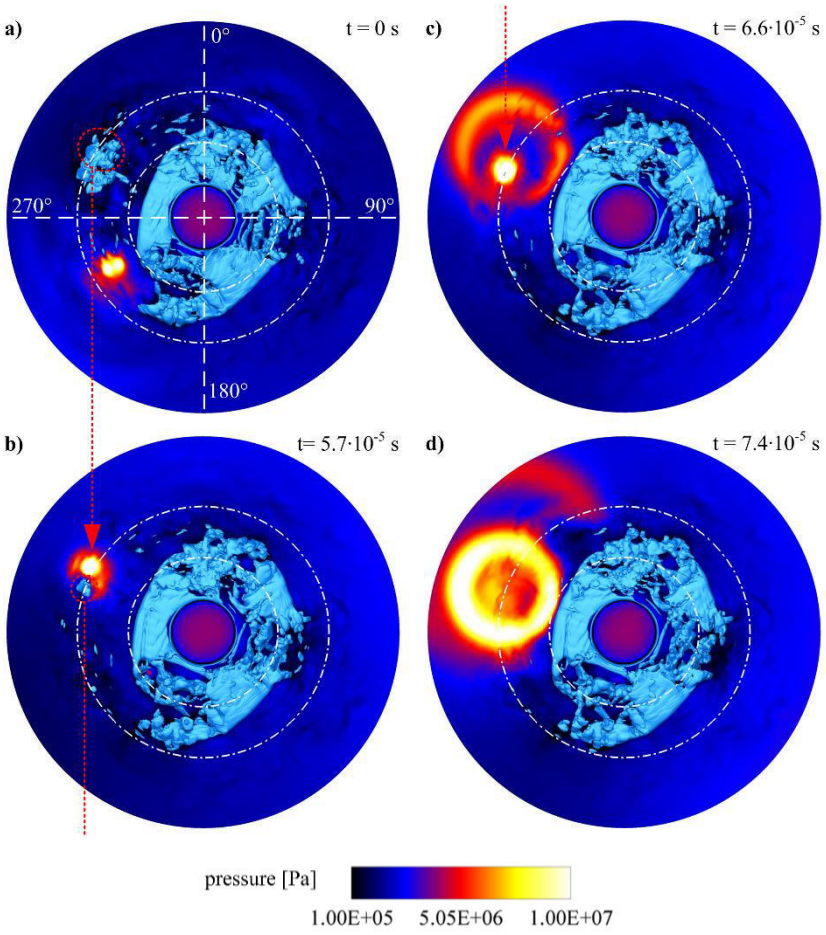

FIG. 5.6. Four consecutive single time instants of a collapse situation (40 bar case) showing iso-surfaces of the vapor volume fraction ($\alpha \geq 10\%$) and static pressure on the lower wall as contour. The view is in the direction of the nozzle flow facing the target. Dash-dotted lines indicate the area where pitting was observed in the experiment.

5.3 Frequency Spectra

Growth, fragmentation, and collapse of vapor structures occur periodically. To identify underlying flow dynamics, we analyze the frequency spectra of time-dependent quantities. Spectra are computed using the MATLAB implementation of the Welch method with 50 % overlap and a rectangular window function of ≈ 0.01 s size. FIG. 5.7 shows spectra of vapor volume fraction, integrated over the entire domain and sampled at each timestep.

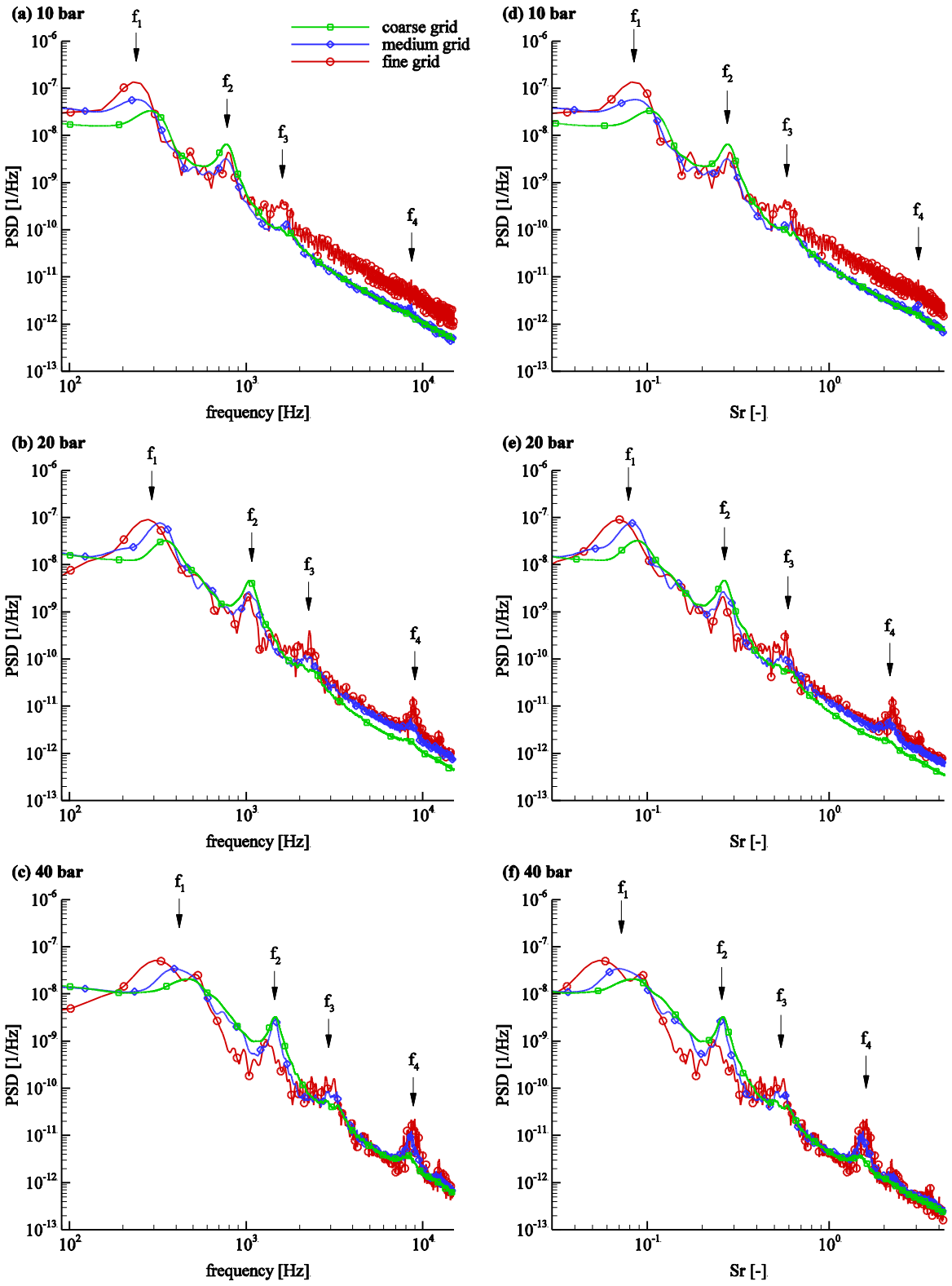

FIG. 5.7. Frequency spectra of the vapor volume fraction integrated over the computational domain for all three grids. (a), (d): 10 bar. (b), (e): 20 bar. (c), (f): 40 bar. Four characteristic frequencies ($f_1 - f_4$) are present in all calculations. Reprint with permission from Ref. 37. Copyright 2015 by AIP Publishing.

Four characteristic frequencies (referred to as $f_1 - f_4$) are present in the spectra of all operating conditions: $f_1 - f_3$ increase with increasing pressure level; f_4 is independent of the operating condition. f_2 is the shedding frequency. The Strouhal number characterizing a shedding mechanism with the frequency f has already been defined as[2]

$$Sr_{shedding} = \frac{f\, L_{\max}}{v_c} \tag{5.2}$$

with the maximum length of an attached sheet cavity L_{max}. The characteristic velocity on the cavity v_c, which can be estimated by the Bernoulli equation[8]

$$v_c \approx \sqrt{2(p_{in} - p_{sat})/\rho} \tag{5.3}$$

assuming vapor pressure in the liquid near the cavity. Here, p_{in} is the stagnation pressure of the incoming flow, p_v the vapor pressure, and ρ the density of the liquid phase. L_{max} was estimated by visual inspection of 200 consecutive snapshots of data ($\Delta t \approx 8.8 \cdot 10^{-6}$ s). Based on observed values of v_c ($v_{c,\,10bar}$ = 44.6 m/s, $v_{c,\,20bar}$ = 63.3 m/s, $v_{c,\,40bar}$ = 89.6 m/s), L_{max} ($\approx 16 \cdot 10^{-3}$ m), and f_2 ($f_{2,10bar} \approx 800$ Hz, $f_{2,20bar} \approx$ 1100 Hz, $f_{2,40bar} \approx 1550$ Hz), values of Sr are found ($Sr_{10bar} = 0.269$; $Sr_{20bar} = 0.261$; $Sr_{40bar} = 0.259$). This is in good agreement with values for Sr reported for shedding instabilities ($Sr \approx 0.25$-0.35, e.g. Ref. 2). Furthermore, f_2 is consistent with the shedding frequency estimated from time-series similar to FIG. 5.5. f_3 is the first harmonic mode of f_2. The mechanism responsible for f_1 cannot be clearly identified ($f_{1,10bar}$ ≈ 280 Hz, $f_{1,20bar} \approx 350$ Hz, $f_{1,40bar} \approx 450$ Hz). The corresponding Sr slightly increase from ≈ 0.07 to $\approx$ 0.1 with increasing characteristic velocity. f_1 is probably due to an oscillation of the total vapor volume in radial direction, as f_1 can also be found in the spectrum of the mass-flux across planes with constant radius (FIG. 5.9) and the mass-flux at the outlet (not shown).

Frequency f_4 is related to the reflection of collapse-induced pressure waves at the radial boundary of the gap. The values of f_4 ($\approx 8000 - 9000$ Hz) and the speed of sound in water ($c_l \approx 1482$ m/s) correspond to a radial collapse position of $r \approx 27 - 38 \cdot 10^{-3}$ m, which is consistent with the observed outermost collapse positions (see section 5.4, FIG. 5.12 and FIG. 5.11). As wave speed and geometry do not vary with operating conditions wave-reflection explains why f_4 is constant for all operating conditions.

For validation we compare spectra of the experimental and numerical pressure sensors. A dominant frequency f_2' is found that is close to f_2 but slightly larger for all operating conditions (FIG. 5.8) and f_3' is the first harmonic. Both frequencies are in good agreement with the experiment for the 10 bar case and are slightly underestimated for the 20 bar and 40 bar cases.

To differentiate more clearly between f_2 and f_2', FIG. 5.9 shows spectra of a numerical pressure sensor, the vapor volume, the mass-flux in radial direction in planes with constant radius, m_{rad}, and the mass-flux in circumferential direction in planes with constant circumferential position, m_{cir}. The shedding mechanism is a periodic motion in radial direction. Consequently f_2 is present in the spectra of

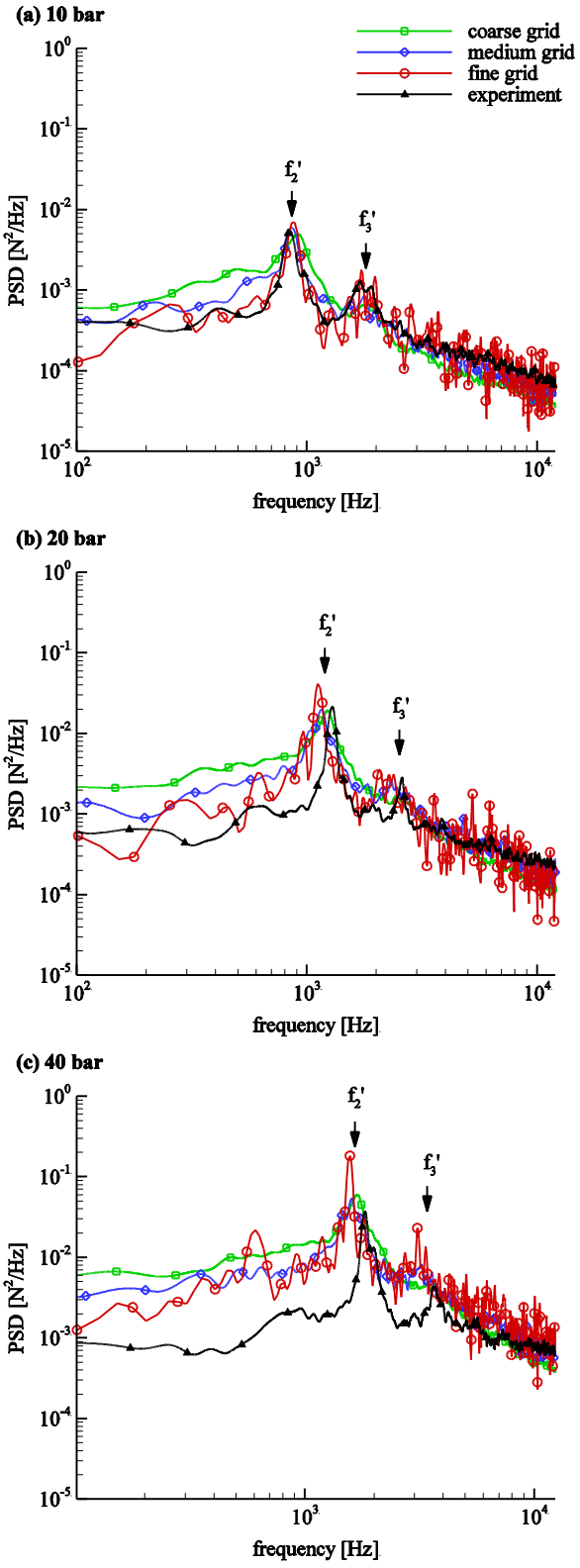

FIG. 5.8. Frequency spectra of the experimental pressure sensor and the numerical pressure sensors for all three grids. (a) 10 bar. (b) 20 bar. (c) 40 bar. Two characteristic frequencies (f_2', f_3') are present in all calculations and the experiment. Reprint with permission from Ref. 37. Copyright 2015 by AIP Publishing.

the vapor volume and of m_{rad}. The dominant frequency at the sensor, f_2', is present in the spectrum of m_{cir}. We thus can assume that f_2' is related to a circumferential mode.

As all characteristic frequencies mentioned above (especially f_2) are represented by the spectra for each grid (see FIG. 5.7 and FIG. 5.8), we can conclude that the main mechanisms are reproduced by all grid resolutions.

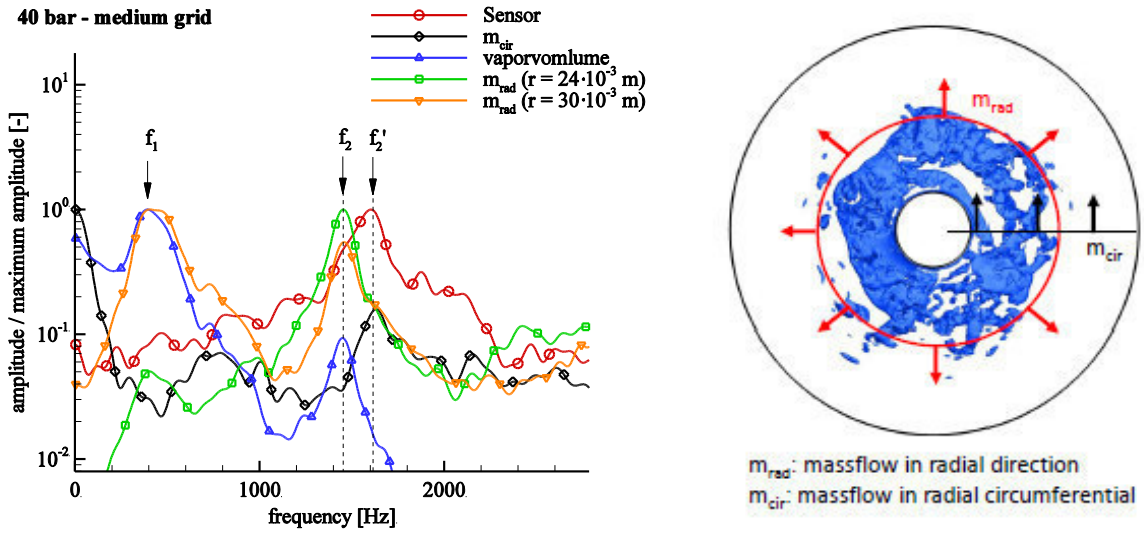

FIG. 5.9. Frequency spectra of the numerical pressure sensor, the vapor volume, the mass flux over planes with constant radius, m_{rad}, and the mass flux over planes with constant circumferential position, m_{cir}. Reprint with permission from Ref. 37. Copyright 2015 by AIP Publishing.

5.4 Collapse Positions and Relation to Damage Area

The collapse of vapor structures constitutes the main mechanism of cavitation erosion. In the following we discuss predicted collapse locations. FIG. 5.10 (a) shows all collapse events detected during the simulated time interval for the "fine" resolution of the 40 bar case. A high density of events is detected near the nozzle exit and in the closure region of the cavity. Collapse events near walls have a potential to cause damage on the material. Areas where high pressure maxima occur at a wall during the simulation time interval are indicative for strong collapses, FIG. 5.10 (c). In FIG. 5.10 (b) collapse events near the two walls are shown. When taking events within a distance of less than $0.5 \cdot 10^{-3}$ m into account, areas of high pressure maxima correlate well with areas with a high density of strong collapse events.

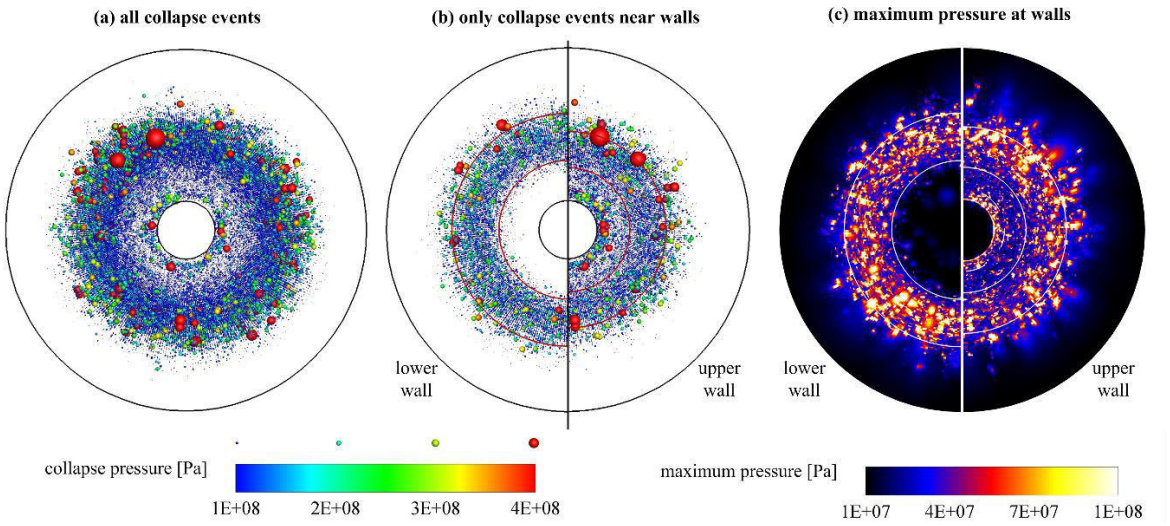

FIG. 5.10. (a) Collapses detected in the flow field for the 40 bar case on the fine grid. Each collapse is represented by a sphere at the center of the respective grid cell. Size and color represent the collapse pressure scaled to $x_{ref} = 181 \cdot 10^{-6}$ m (with the linear decay law for spherical waves, see Eq. (4.9)). (b) Only collapses with a distance to a wall $< 0.5 \cdot 10^{-3}$ m. (c) Maximum pressure recorded at the walls during the simulation time interval. Marked areas (red and white circles) correspond to experimentally observed material damage (see FIG. 5.1 (b)). Reprint with permission from Ref. 37. Copyright 2015 by AIP Publishing.

FIG. 5.11 shows events detected near walls for all simulations. Collapse pressures are scaled using Eq. (4.9) ($x_{ref} = 181 \cdot 10^{-6}$ m). FIG. 5.12 exhibits pressure maxima for all simulations. Only collapse events with pressures approximately one order of magnitude larger than the stagnation pressure ($> 10^7$ Pa) are shown. As expected, strong collapse events are detected near walls in regions of high pressure maxima. The highest maximum pressures are recorded at the lower wall at a radius $r \approx 28 \cdot 10^{-3}$ m. When comparing results from different spatial resolutions, two aspects have to be taken into account: First, the maximum pressure of a given collapse situation increases with increasing grid resolution (with characteristic cell length x_{char}, see chapter 4.2.3 and Eq. (4.9)). Thus, higher collapse- and maximum-pressures are detected on a finer grid. This mechanism is relevant for comparing (a) and (b) in FIG. 5.11 and FIG. 5.12. Second, simulation time intervals decrease with grid refinement (see Table VII). Consequently, smaller absolute number of collapses are computed on a finer grid (relevant for comparing (b) and (c) in FIG. 5.11 and FIG. 5.12). We compare our predictions (FIG. 5.11 and FIG. 5.12) with the position where material damage was observed in the experiment (FIG. 5.1 (b)). Experimental findings are marked with lines. Apparently, maximum pressure and high densities of strong collapse events correlate well with the three damage areas of the experiment. In the simulations the radial extent is slightly overestimated on both sides of the gap. We conclude that predicted collapse locations agree with the experiment. Additionally, the location of collapse events is not affected by grid resolution.

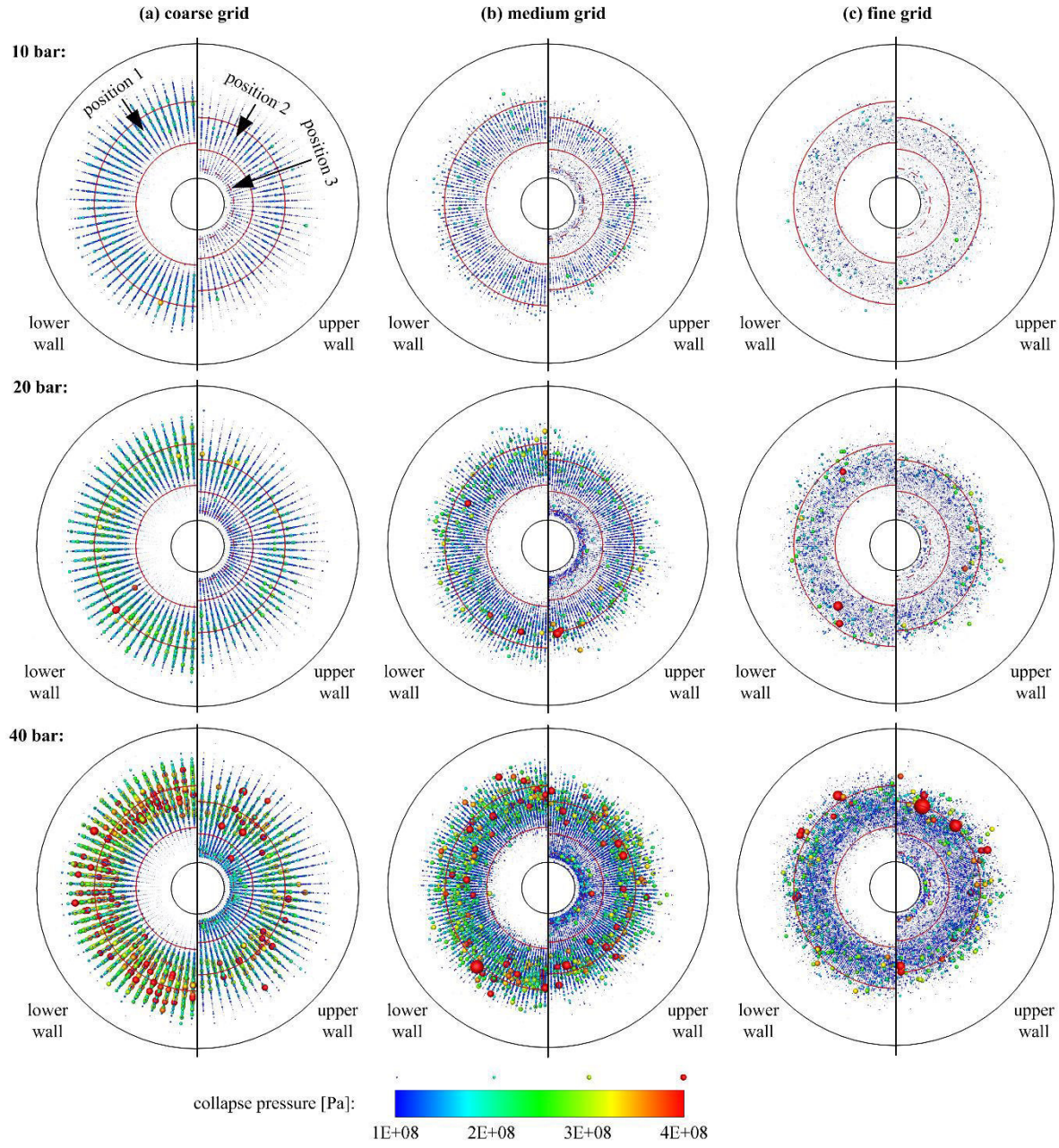

FIG. 5.11. Visualization of collapses detected during the analysis interval. Each collapse is represented by a sphere at the center of the respective grid cell. Size and color represent the collapse pressure scaled to $x_{ref,p} = 181 \cdot 10^{-6}$ m (with the linear decay law for spherical waves, see Eq. (4.9)). Only collapses with a distance to the target lower than $0.5 \cdot 10^{-3}$ m are shown. (a) coarse grid. (b) medium grid. (c) fine grid. Note that the simulated time interval decreases from (a) to (c) (see Table VII). Marked areas (red circles) correspond to experimentally observed material damage (see FIG. 5.1 (b)). Reprint with permission from Ref. 37. Copyright 2015 by AIP Publishing.

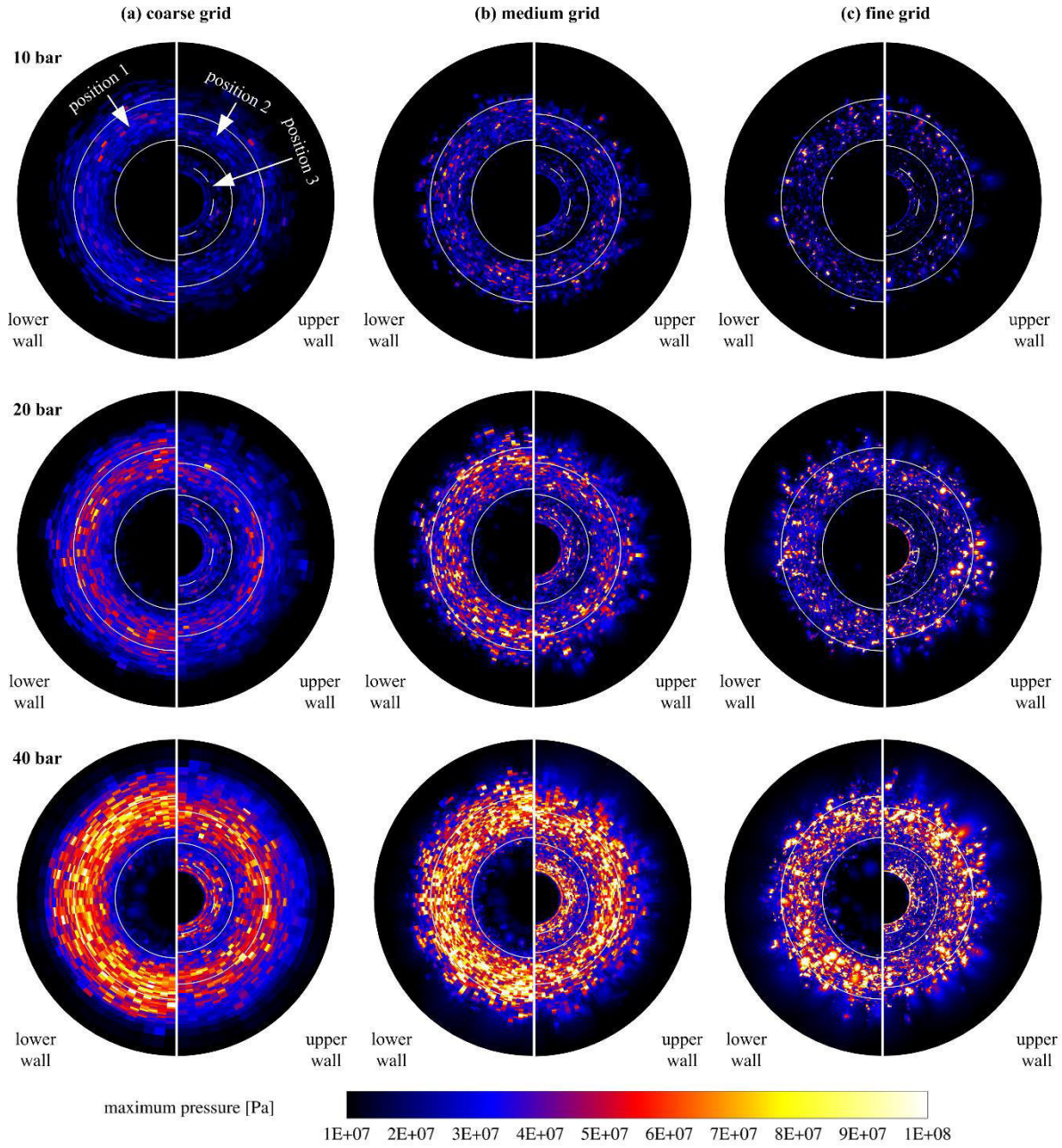

FIG. 5.12. Maximum pressure recorded at the walls during the simulation time interval. (a) coarse grid. (b) medium grid. (c) fine grid. Note that the simulated time interval decreases from (a) to (c) (see Table VII). Marked areas (white circles) correspond to experimentally observed material damage (see FIG. 5.1 (b)). Reprint with permission from Ref. 37. Copyright 2015 by AIP Publishing.

5.5 Collapse-Induced Load Spectra

In the preceding sections we showed that global cavitation dynamics, governing frequencies, and collapse locations are reasonably predicted by the simulation. In the following we discuss predicted load spectra.

5.5.1 Impact Load Spectra on Pressure Sensors

To determine the impact load spectra on the numerical pressure sensors isolated force-peaks are identified. FIG. 5.13 shows the time signal of a pressure sensor, generated on the fine mesh. It represents the largest numerical sampling rate ($62 \cdot 10^6$ Hz), which is approximately 30 times larger than in the experiment. For comparability we follow the signal processing procedure used in the experiment, where after detection of a peak a lock time of 10^{-6} s is applied.[8] Due to the lock time, wave reflections after a collapse are not taken into account for the computation of the peak rate (see FIG. 5.13 (c)). Additionally, a minimum threshold of 110 N was defined for the detection of a peak.[8]

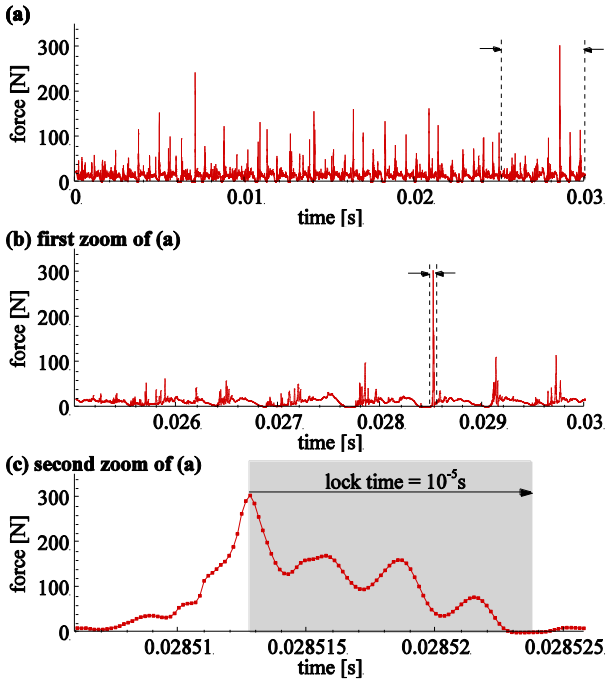

FIG. 5.13. Time signals of a pressure sensor on the fine mesh. (b) and (c) are successive temporal zooms of (a), showing a strong sharp peak, typically caused by a collapse on the sensitive area of the sensor. In (c) only every tenth data point is shown and the lock time of the post-processing routine is indicated. Reprint with permission from Ref. 37. Copyright 2015 by AIP Publishing.

The fragmentation of vapor structures depends on the grid resolution, see FIG. 5.5. Assuming that the collapse of every vapor fragment near the sensor leads to a pressure peak, the rate of pressure peaks

on the sensor is resolution dependent. FIG. 5.14 (a) shows the cumulative rate of pressure peaks per time and area, $\dot{N}_s$ vs. the force on a sensor F for the 40 bar case. The graphs follow a power law

$$\dot{N}_s = \dot{N}_0 \exp\left(-\frac{F}{F_0}\right) \tag{5.4}$$

where $\dot{N}_0$ is a characteristic rate (defining the intersection with the y-axis) and F_0 is a characteristic force (defining the slope in the semi-logarithmic diagram). All graphs show a self-similar behavior with approximately uniform F_0 and a constant offset per grid refinement level. This motivates a scaling for the peak rate in the form of

$$\dot{N}_{s,scale} = \left(\frac{x_{char}}{x_{ref,N}}\right)^{\kappa} \dot{N}_s \tag{5.5}$$

which represents a shift along the y-axis, while keeping the slope constant. Here $x_{char}/x_{ref,N}$ is the ratio of a characteristic cell-length of the grid x_{char} and a reference length scale $x_{ref,N}$ similar to Eq. (4.9). As measure for x_{char}, the cube root of the volume of a numerical cell in the center of the sensor is used. κ is a constant exponent that needs calibration. FIG. 5.14 (b) shows peak rates with applied scaling law (Eq. 5.5) for two different values of $x_{ref,N}$. The spectra collapse for $\kappa = 3/2$.

The impact load spectrum is a local quantity and depends on the position of the sensor. FIG. 5.15 compares the scaled spectra of two numerical sensor positions with the spectra (without any scaling) on the experimental sensor. We define a spectrum as “more aggressive” when it contains a higher rate for

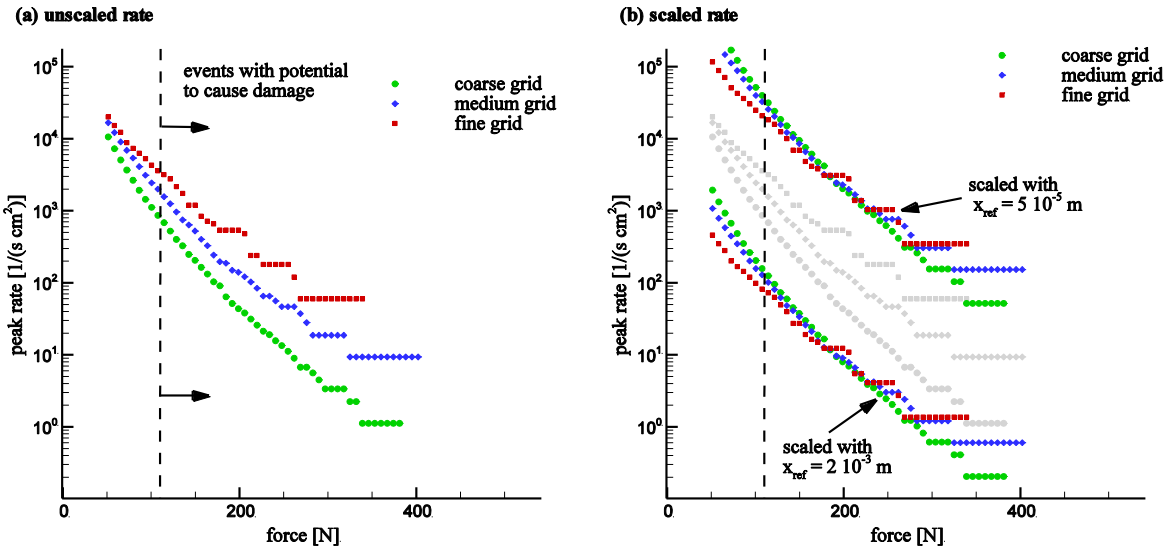

FIG. 5.14. Cumulative rate of pressure peaks on the numerical pressure sensors per time and area (log-scale) against the force on the sensor (linear scale). (a) Peak rates as recorded in the experiment. (b) Peak rates with applied scaling law (Eq. 5.5) for two different values of $x_{ref,N}$. Reprint with permission from Ref. 37. Copyright 2015 by AIP Publishing.

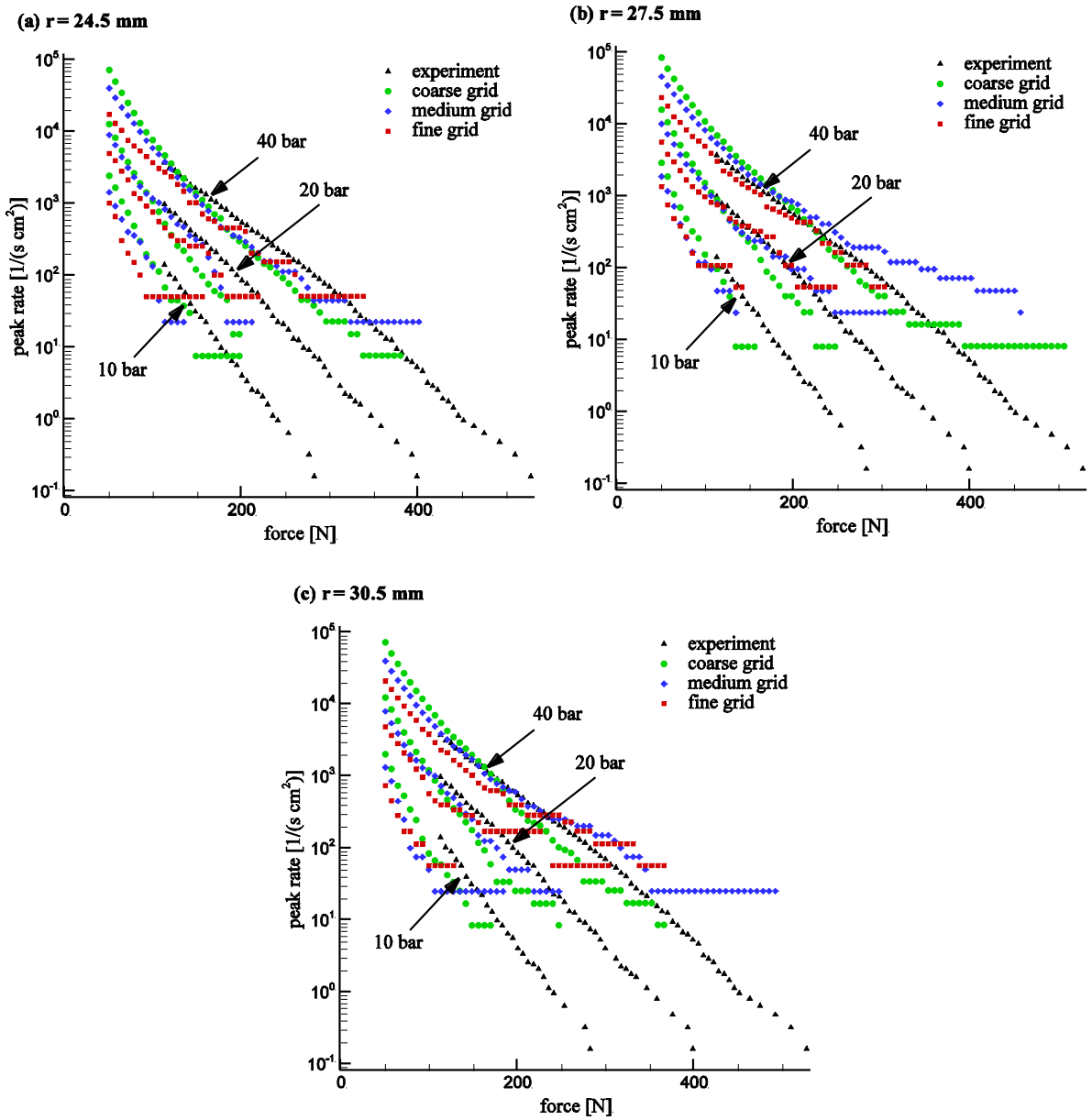

FIG. 5.15. Cumulative scaled rate of pressure peaks on the numerical pressure sensors per time and area for $x_{ref,N} = 181 \cdot 10^{-6}$ m and cumulative rate of pressure peaks on the experimental pressure sensors (without any scaling) per time and area against the force on the sensor. The position of the experimental sensor is fixed ($r = 24.5 \cdot 10^{-3}$ m), while the position of the numerical sensors vary: (a): $r = 24.5 \cdot 10^{-3}$ m. (b): $r = 27.5 \cdot 10^{-3}$ m. (c): $r = 30.5 \cdot 10^{-3}$ m. The numerical sensor at $r = 27.5 \cdot 10^{-3}$ m (b) shows the most aggressive spectrum. Experimental data from Ref. 8. Reprint with permission from Ref. 37. Copyright 2015 by AIP Publishing.

a given force. In the simulation, more aggressive spectra are recorded with the sensor at $r = 27.5 \cdot 10^{-3}$ m (FIG. 5.15 (b)). Here, experimental and numerical rates agree for $x_{ref,N} = 181 \cdot 10^{-6}$ m, which is close to the characteristic length scale on the fine grid. In particular, the slope of the experimental rate of events, which contains information about the composition of the load profile, can be reproduced by the simulations. The sensor at $r = 24.5 \cdot 10^{-3}$ m (FIG. 5.15 (a)) shows less aggressive spectra for the same $x_{ref,N}$. This is consistent with the overestimation of the radial extent of collapse locations in the

simulations (see. FIG. 5.11 and FIG. 5.12). The agreement of experimental and numerical data validates the impact load spectrum predicted by the numerical simulations.

5.5.2 Load Spectra in the Fluid Domain

While a pressure sensor records the impact load spectrum at a single location at a wall, collapse events are detected in the whole fluid domain by the collapse detector. In both cases, fragmentation leads to a grid-dependence of peak- and collapse rates, respectively. Therefore, we apply Eq. 5.5 to detected collapse rates. As the characteristic cell length x_{char} may vary locally, the scaling is applied for every collapse event independently. The rate of a single collapse occurring once within the analyzed time interval Δt is

$$\dot{N}_c = \frac{1}{\Delta t} \tag{5.6}$$

Incorporating Eq. 5.5, the scaled rate of that single collapse is computed as

$$\dot{N}_{c,scaled} = \frac{1}{\Delta t}\left(\frac{x_{char}}{x_{ref,N}}\right)^{\kappa} = \frac{1}{\Delta t}\left(\frac{\sqrt[3]{V_{cell}}}{x_{ref,N}}\right)^{\kappa}, \quad \kappa = \frac{3}{2} \tag{5.7}$$

The rate of all events is computed from the sum of all single-collapses event rates. Additionally, the collapse pressure is scaled according to Eq. (4.9).

FIG. 5.16 shows the scaled load spectra determined by the collapse detector. Spectra show grid convergence for high event rates, while scatter increases for events occurring less often. For all calculations the spectra decay exponentially. This is a typical behavior observed in cavitation experiments, when plotting a quantity for the intensity of an event (e.g. diameter of a resulting pit[9,77,78] or the peak of a recorded pressure signal[10,77,78]) against the temporal rate. For both scaling laws (Eq. (4.9) and Eq. 5.5) the same parameter $x_{ref,N} = x_{ref,p} = 181 \cdot 10^{-6}$ m is used. This choice is discussed in section 5.6.

We compare numerically predicted collapse rates to experimental pitting tests on an aluminum target, where the intensity of a single impact is quantified with the diameter of the corresponding pit. Pitting rates are available on the lower wall for a toroidal-area of $4 \cdot 10^{-3}$ m width in radius where most intense pitting was found.[79] In the simulations we take into account collapses near the lower wall (distance < $0.5 \cdot 10^{-3}$ m, see FIG. 5.10) in the region where the highest maximum pressures are detected at the wall ($26 \cdot 10^{-3}$ m < r < $30 \cdot 10^{-3}$ m, see section 5.4). This corresponds to the sensor position, where the most aggressive impact load spectra are recorded (FIG. 5.15).

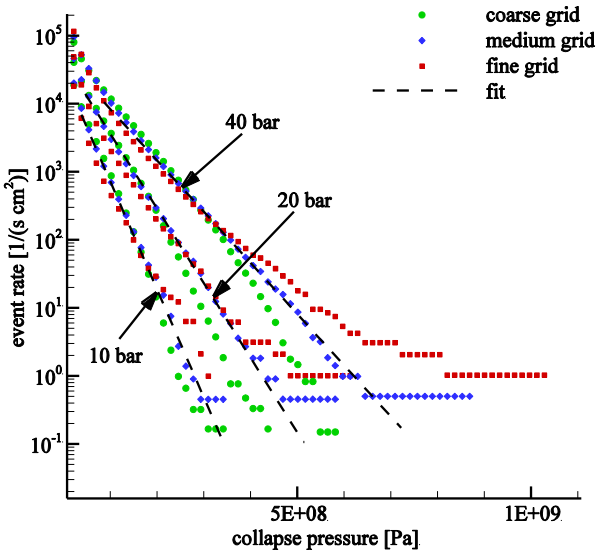

FIG. 5.16. Cumulative scaled rate of collapse events per time and area (Eq. 5.7) against the scaled collapse pressure p_{scale} (Eq. (4.9)) for $x_{ref} = 181 \cdot 10^{-6}$ m. Reference area is the pitted area on the lower wall (see FIG. 5.1 (b)). All detected collapses events are taken into account. The dashed black line represents a fit for each operating condition. Reprint with permission from Ref. 37. Copyright 2015 by AIP Publishing.

For each grid, thresholds of the scaled collapse pressure are shown in FIG. 5.17. Numerical collapse rates follow the trend of experimental pitting rates. The resulting ranges of the threshold of collapse pressure show only a slight grid-dependence, see Table VIII. The correlation of numerical collapse rates and experimental pitting rates demonstrates that the concept of the introduced collapse detector is capable of extracting meaningful information about the impact load spectrum from the simulation.

Table VIII: Comparison of experimental pitting rates on an Al-target and numerical collapse rates.

pit diameter [m]	range of scaled collapse pressures [Pa]
$> 10 \cdot 10^{-6}$	$1.60 \cdot 10^{8} - 1.88 \cdot 10^{8}$
$> 20 \cdot 10^{-6}$	$1.82 \cdot 10^{8} - 2.02 \cdot 10^{8}$
$> 50 \cdot 10^{-6}$	$2.20 \cdot 10^{8} - 2.29 \cdot 10^{8}$
$> 100 \cdot 10^{-6}$	$2.70 \cdot 10^{8} - 2.72 \cdot 10^{8}$
$> 200 \cdot 10^{-6}$	$3.85 \cdot 10^{8} - 4.23 \cdot 10^{8}$

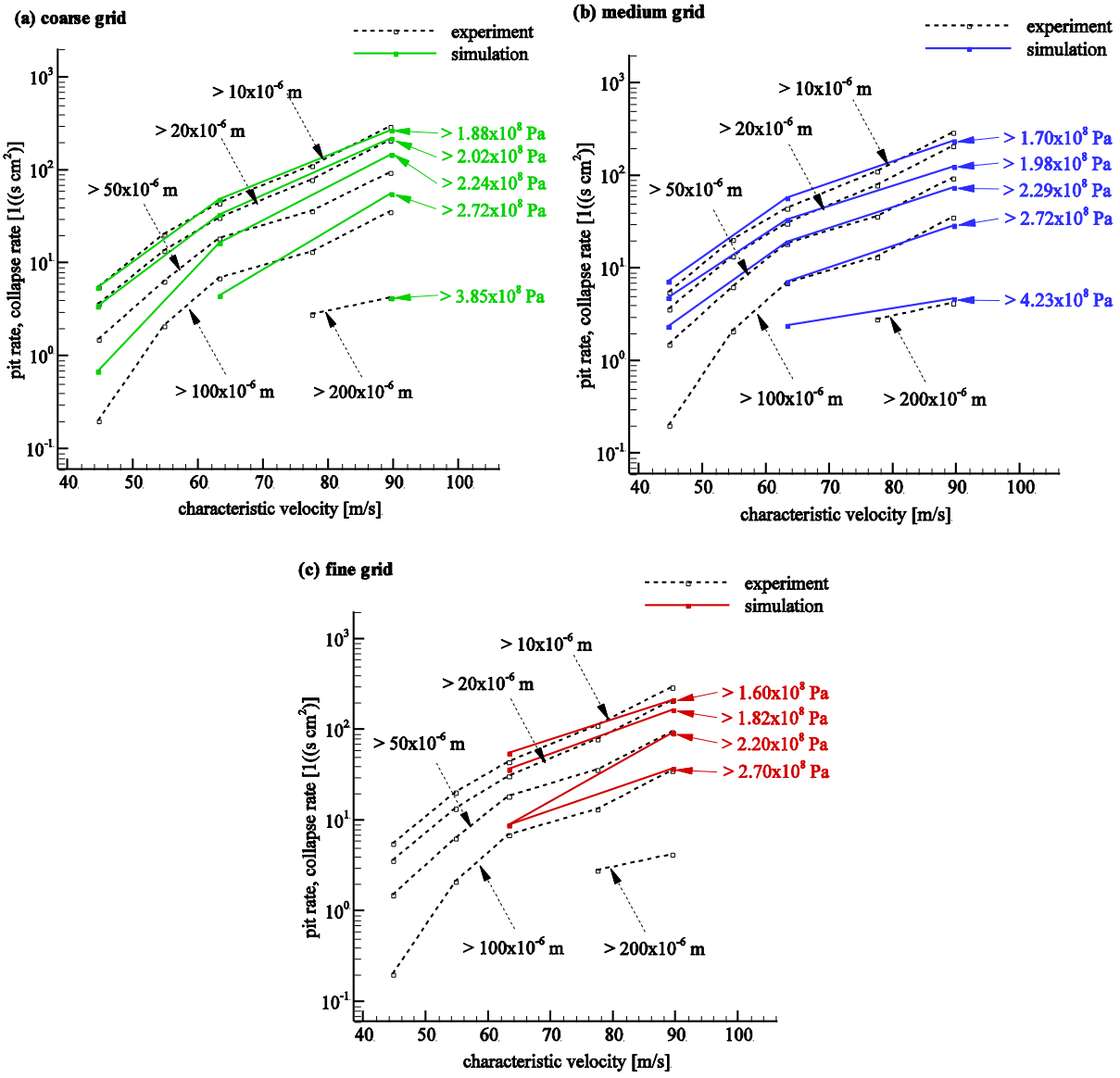

FIG. 5.17. Comparison of pitting rates on an Al-target for different pit sizes in the experiment (dashed line) and scaled collapse rates in the simulation (solid line). (a) coarse grid. (b) medium grid. (c) fine grid. Only collapses near the target (distance to target < $0.5 \cdot 10^{-3}$ m) in a toroidal area ($26 \cdot 10^{-3}$ m < r < $30 \cdot 10^{-3}$ m) are taken into account. Numerical rates and numerical collapse pressures are scaled to x_{ref} = $181 \cdot 10^{-6}$ m, experimental data is not scaled. Thresholds for the scaled collapse pressure slightly differ for each spatial resolution (see Table VIII). Experimental data from Ref. 79. Reprint with permission from Ref. 37. Copyright 2015 by AIP Publishing.

5.6 Discussion: Interpretation of $x_{ref,N}$ and $x_{ref,p}$

The identification of $x_{ref,N}$ is performed by comparing outputs from the experimental and numerical pressure sensors. The sensor is resolved in space by the numerical grid, and the pressure signal thus is averaged over the same area in experiment and simulation. A requirement for quantifying the rate of events is that data for experiment and simulation are both resolved in time.

In the presented setup, large-scale vortices provide kinetic energy at the integral length scale L_0 by the shedding mechanism and associated Kelvin-Helmholtz- and Rayleigh-Taylor-instabilities. As we observe large-scale dynamics on all grids (see e.g. section V. A and B), we conclude that the integral length scale is well resolved. The Kolmogorov scale η can be estimated to be around $\eta \approx 0.2\text{-}0.4 \cdot 10^{-6}$ m ($Re \approx 1\text{-}2 \cdot 10^5$ for 10 bar and 40 bar case, gap-size = $2.5 \cdot 10^{-3}$ m). The finest grid resolution in our computations is at least 200-400 times coarser than η. Thus, the smallest length scale, which can be resolved by our simulations Δx, is within the inertial subrange for all applied grid resolutions: $L_0 > \Delta x > \eta$ as shown in FIG. 5.18. The three spatial resolution differ in the resolved ranges of the inertial subrange.

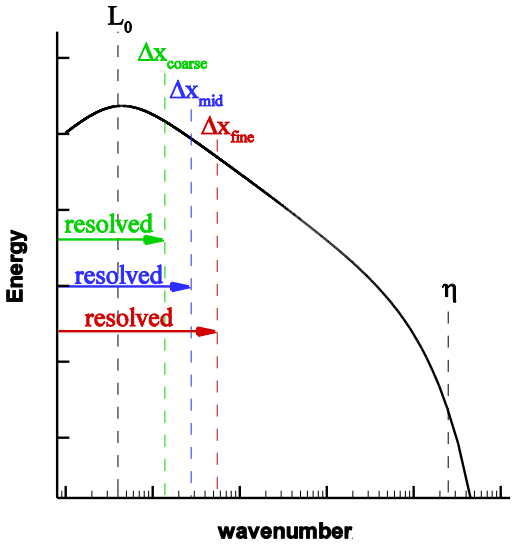

FIG. 5.18. Sketch of a model spectrum of kinetic energy over wave number. Reprint with permission from Ref. 37. Copyright 2015 by AIP Publishing.

It can be assumed that the rate of collapse events is proportional to the number of vapor structures that are resolved by the simulation. Large-scale vapor structures are produced by the shedding mechanism (represented on all grid levels). Fragmentation however is limited by grid resolution. As stated before, this limit is in the inertial range for all our simulations. In this range, the number density of turbulent vortices of a size λ scales as λ^{-3} for single phase turbulence.[80-82] This observation supports that a quantity related to vortical inertial-range structures should exhibit universal scaling, where the scaling parameter κ=3/2, however, is an empirical finding.

If the grid was much finer than the Kolmogorov scale η the use of Euler equations would result in an unphysical amount of small scale energy (and small scale structures), since viscous dissipation is missing. In the present case, however, the identified value of $x_{ref,N}$ is three orders of magnitude larger than η. A cell size finer than $x_{ref,N}$ would result in higher impact rates than in the experiment, and thus too many collapsing vapor fragments. Thus it is plausible that $x_{ref,N}$ represents a physical limit for the fragmentation of vapor structures. As $x_{ref,N} >> \eta$ there is no direct dependence on viscosity.

A second simplification in our model is to neglect the discrete distribution of vapor and liquid at length scales less than Δx. This includes neglecting effects of surface tension. A turbulent eddy with size L most likely breaks a bubble with diameter d when $L \approx d$.[83] Eddies with $L >> d$ lead to translation of the bubble rather than breakup.[83] A largest stable bubble size can be estimated from the Weber-number $We = (\rho \cdot u(L)^2 \cdot d)/s \approx 1$, where s is surface tension, ρ is density and $u(L)$ is a characteristic velocity of an eddy with size L. For incompressible isotropic turbulence, $u(L)$ scales as $u(L) = (\varepsilon \cdot L)^{1/3}$.[84] A estimate for the dissipation rate $\varepsilon \approx u_0^3/L_0$.[84] For $L = d$, We is unity at $d \approx 4 \cdot 10^{-6}$ m, which is approximately one order of magnitude larger than η. This means that surface tension limits the formation of smaller vapor fragments in a range where viscosity still is insignificant.

The scaling for collapse pressure (Eq. (4.9)) compensates the grid-dependence of the pressure that is detected in the cell the collapse occurs. It is important to note, that the pressure scaling is only applied to the collapse-detector data. For quantifying $x_{ref,p}$, one would need spatially resolved information about collapse pressures from the experiment, e.g. an equivalent to the collapse detector, or a pressure sensor, that spatially resolves the impact load. To our knowledge, however, such data are not available.

A characteristic length scale of an impact load on the material is assumed to be smaller than the diameter of a pit (i.e., $< 200 \cdot 10^{-6}$ m). We choose the value $x_{ref,p} = x_{ref,N} = 181 \cdot 10^{-6}$ m, as this corresponds to a cell size where impact load spectra on the sensor agree for simulation and experiment. The comparison between collapse rates (from the collapse detector) and pitting rates (from the experiment), FIG. 5.17, shows analogies between scaled collapse pressures and pit-sizes. Even if the level of the scaled collapse pressures may change when a proper calibration of $x_{ref,p}$ is found, these relations remain, as the rate-scaling is not affected.

5.7 Influence of Thermodynamic Modelling

To investigate the influence of thermodynamic modelling, calculations have been performed with the barotropic model described is section 3.3.2. Numerical setup (see section 5.1) and boundary conditions (see Table VI) remain unchanged. Compared to the previous calculations about half the physical time is simulated. Parameters of the computations are summarized in Table IX.

Table IX: Parameters of the barotropic computations.

Grid	coarse	medium	fine
Numerical time-step	$6.4 \cdot 10^{-8}$ s	$3.1 \cdot 10^{-8}$ s	$1.5 \cdot 10^{-8}$ s
Simulated physical time – 10 bar	≈ 1.2 s	≈ 0.19 s	≈ 0.019 s
Simulated physical time – 20 bar	≈ 1.2 s	≈ 0.19 s	≈ 0.019 s
Simulated physical time – 30 bar	≈ 1.3 s	≈ 0.16 s	≈ 0.019 s

Evaluation of simulation data shows that taking the energy equation into account does not have a decisive influence for the present test case. Characteristic frequencies in the temporal evolution of vapor volume (FIG. 5.19) and the time signal of the innermost pressure sensor (FIG. 5.20) remain unchanged. Output of the collapse detector are presented in FIG. 5.21. Load spectra collapse for barotropic calculations and calculations with full thermodynamic treatment. Frequency spectra and load spectra of both thermodynamic models are in good agreement for higher frequencies and higher event rates respectively. For low frequencies and low event rates scatter slightly increases.

5.8 Conclusion

The preceding chapter presents a grid resolution study of cavitating flows. Grid convergence is observed for the overall cavitation dynamics by comparison of flow topology, frequency spectra of time-dependent quantities, and location of collapse events. Agreement of the predicted dynamics with the experiment is demonstrated by comparison of frequency spectra of experimental and numerical pressure sensors. Additionally, collapse locations in the simulation agree with erosion endangered areas in the experiment. The good agreement with the experiment confirms that inertia drives the shedding mechanism which dominates the flow field and motivates an inviscid flow model.

Although large-scale cavitation structures are resolved, generation of small scale cavitation structures with grid refinement as consequence of the inviscid model is observed, as expected. A scaling law that removes resolution effects is proposed for the predicted rate of events. The scaling law contains the ratio of a characteristic length scale of the numerical grid, x_{char}, and a reference length scale $x_{ref,N}$. The latter introduces a limiting length scale for the fragmentation of vapor structures and is calibrated by comparing impact load spectra on experimental and corresponding numerical pressure sensors. With scaling law applied and $x_{ref,N}$ calibrated, the quantitative agreement between experimental and numerical pressure sensors demonstrates that realistic impact load spectra can be derived even from coarsely resolved data. The calibrated value of $x_{ref,N}$ suggests that the limiting length scale for fragmentation is not connected to viscosity in the present case.

Finally, comparison of barotropic calculations with calculations with full thermodynamic treatment show that the thermodynamic modelling does not notably influence the predicted flow and load spectra.

In conclusion, the homogeneous mixture approach is suitable for predicting the impact load spectrum and by that the erosive potential of a cavitating flow. This holds even if only macroscopic vapor structures are resolved and actual vapor bubbles are highly under-resolved.

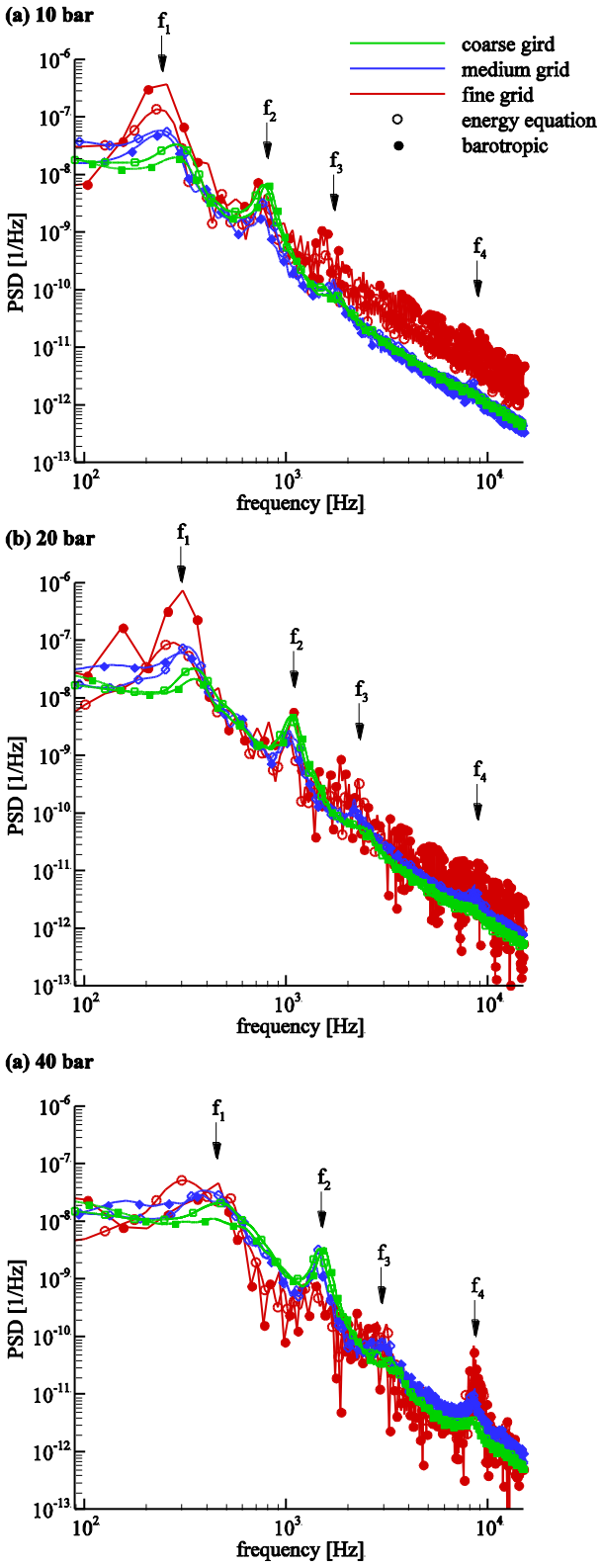

FIG. 5.19. Frequency spectra of the vapor volume fraction integrated over the computational domain for all three grids. (a) 10 bar. (b) 20 bar. (c) 40 bar. Closed symbols represent barotropic modelling and open symbols full thermodynamic modelling, respectively.

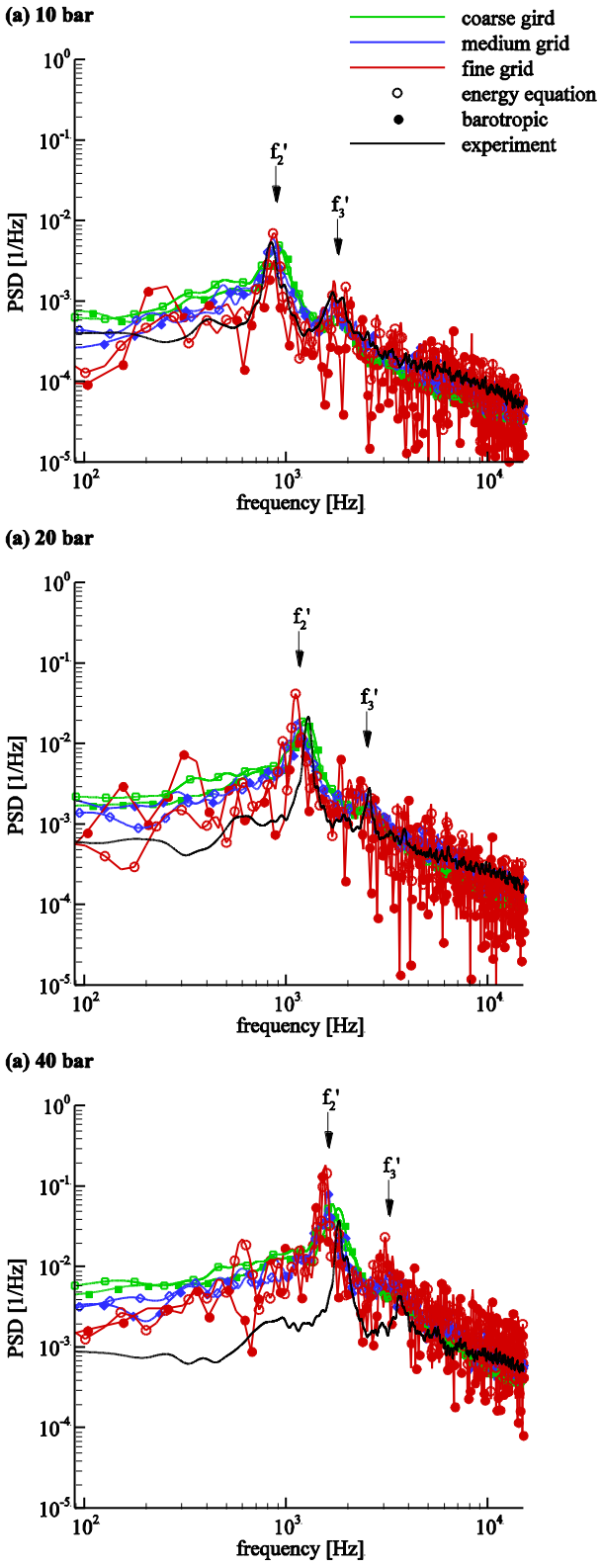

FIG. 5.20. Frequency spectra of the experimental pressure sensor and the numerical pressure sensors for all three grids. (a) 10 bar. (b) 20 bar. (c) 40 bar. Closed symbols represent barotropic modelling and open symbols full thermodynamic modelling, respectively.

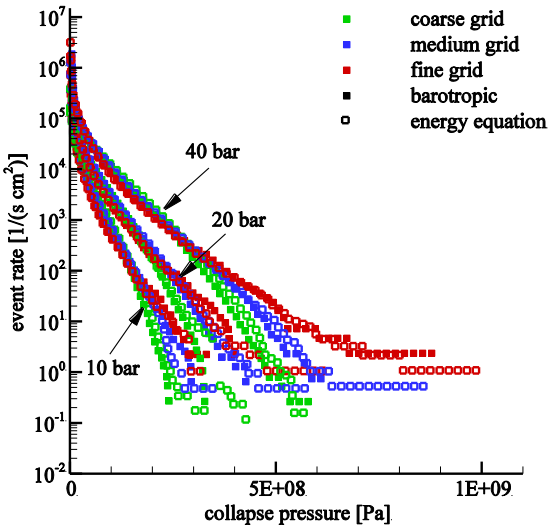

FIG. 5.21. Cumulative scaled rate of collapse events per time and area (Eq. 5.7) against the scaled collapse pressure p_{scale} (Eq. (4.9)) for $x_{ref} = 181 \cdot 10^{-6}$ m. Closed symbols represent barotropic modelling and open symbols full thermodynamic modelling, respectively. Reference area is the pitted area on the lower wall (see FIG. 5.1 (b)). All detected collapses events are taken into account.

6 Estimation of Incubation Times

The impact load spectrum defines the erosive potential of a cavitating flow. However, a flow with a given erosive potential may or may not cause damage, depending on the material. Thus, collapse rates and locations alone do not give information about the probability of erosion damage, but have to be considered in relation to the erosion resistance of the material.

In the following, an analytical material model is utilized. The original model has been used to estimate incubation times based on impact load spectra determined experimentally with pitting test.[35] The analogy of pitting rates and collapse rates shown in chapter 5.5.2 motivates adapting the model for numerically determined collapse spectra. The resulting framework is applied to the axisymmetric nozzle flow introduced in chapter 5.

6.1 Method

A framework for numerical erosion prediction is introduced in this section. First, the material model is introduced in section 6.1.1 and 6.1.2. Section 6.1.3 explains how to derive the impact load spectrum at a solid boundary from information in the entire fluid domain. In section 6.1.4 an approach to extrapolate the load spectrum at large time scales from information at short time scales is introduced. Finally, 6.1.5 summarizes the material thresholds of the materials under consideration.

6.1.1 Energy Absorbed by Material During Impact

The following section summarizes an analytical material model for the prediction of incubation times and erosion rates of ductile materials which can undergo work hardening. The model has originally been proposed by Karimi *et al.*[33] and was adapted by Berchiche *et al.*[34] and Franc *et al.*[35]. In this work we build on the implementation of Franc *et al.*[35]. In the following the material model is described as presented in Ref. 35.

At first we consider a single load on a material surface. The model involves two simplifications: First, the stress σ on the material surface is considered uniform over the impact area S. Outside of S the stress is zero. Second, the temporal evolution of the load, typically characterized by a high amplitude and a short duration resulting in strong gradients in time, is not taken into account.

To evaluate the damaging effect of an impact, the stress σ is compared to characteristic threshold-values of the material, namely the yield strength σ_Y and the ultimate tensile strength σ_U. For the amplitude of σ, the model distinguishes three cases[35]

- $\sigma \leq \sigma_Y$: the stress on the surface is lower than the yield stress of the material. Thus, elastic behavior is dominant and no plastic deformation occurs. An impact with $\sigma \leq \sigma_Y$ causes no damage.
- $\sigma_Y < \sigma \leq \sigma_U$: the stress on the surface is higher than the yield strength of the material, but lower than the ultimate strength. A single impact leads to a plastic deformation and work hardening in the material, but does not cause material failure.
- $\sigma > \sigma_U$: the stress on the surface is higher than the ultimate strength of the material. A single impact leads to plastic deformation and work hardening in the material, and additionally causes material failure on the material surface.

The surface strain is connected to surface stress by a Ludwik type equation[85]

$$\varepsilon(\sigma) = \left(\frac{\sigma - \sigma_Y}{K} \right)^{\frac{1}{n}} \quad \text{, for} \quad \sigma > \sigma_Y \,. \tag{6.1}$$

Although Eq. 6.1 is valid for $\sigma \leq \sigma_U$, it is extrapolated for $\sigma > \sigma_U$.[35]

The material is now exposed to a single load. Prior to loading, the stress is zero everywhere inside the material. A load $\sigma_0 > \sigma_Y$ leads to a plastic strain ε_0 on the material surface, see FIG. 6.1 (a). Subjacent layers in the material are affected by this dislocation. The strain profile inside the material $\varepsilon(x)$ can be modelled by the expression[35]

$$\varepsilon(x) = \varepsilon_0 \left(1 - \frac{x}{l} \right)^{\theta} \tag{6.2}$$

where x is the coordinate inside the material normal to the surface, l is the thickness of the hardened layer and θ is a material constant. FIG. 6.1 (b) shows the strain profile in the material. ε decrease with distance from the surface and is zero for $x=l$. The maximum thickness of the hardened layer L is reached when the surface strain is equal to the ultimate strain ε_U and is a material property. The maximum thickness L is connected to l by[35]

$$\frac{\varepsilon_0}{\varepsilon_U} = \left(\frac{l}{L} \right)^{\theta} \tag{6.3}$$

The energy absorbed per unit volume by a material layer is given by the integral $\int \sigma \, d\varepsilon$. For the surface layer this corresponds to the area ABCD in FIG. 6.1 (a). For a distance to the surface x', the corresponding strain ε' and stress σ' are plotted. The energy absorbed by this layer corresponds to given by ABC'D'. Integration over all layers that got strained during the impact gives the total energy W that is absorbed by the material when exposed to the stress σ_0

$$W = \int_{x=0}^{l} \left(\int_{\varepsilon=0}^{\varepsilon(x)} \sigma \, d\varepsilon \right) S \, dx . \tag{6.4}$$

Together with Eq. 6.1 and 6.3, integration leads to[35]

$$W = \varepsilon_0(\sigma_0) SL \left(\frac{\varepsilon_0(\sigma_0)}{\varepsilon_U} \right)^{1/\theta} \frac{\sigma_Y + \beta K \varepsilon_0(\sigma_0)^n}{1+\theta} = f(\sigma_0, S, material\ consts.), \tag{6.5}$$

$$\text{with} \quad \beta = \frac{1+\theta}{(1+n)(1+\theta+n\theta)} . \tag{6.6}$$

Eq. 6.5 shows that the absorbed energy is a function of the amplitude of the load σ, the surface that load acts on S, and material constants.

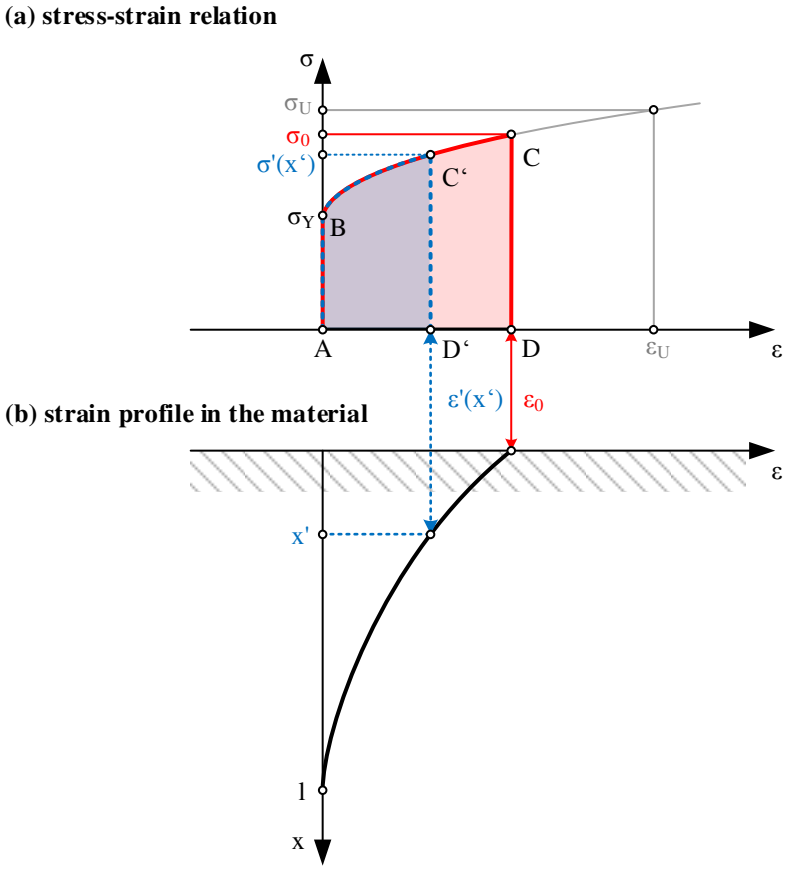

FIG. 6.1. Material response to a single load. (a) Stress strain relation. (b) Stress profile inside the material. Red lines correspond to stress and strain on the superficial material layer, blue lines to a subjacent material layer at distance x' from the surface. Adapted from Ref. 35. Copyright 2009 by ASME.

It is assumed that the absorbed energy is independent of the state of the material, i.e., if the material is virgin, or has undergone work hardening by previous loads. Thus, the energy W_2 absorbed from two successive loads with the amplitude σ_1 is

$$W_2 = 2W_1(\sigma_1)\,. \tag{6.7}$$

With every load that acts on the material, the depth of the hardened layer l growths, as shown in FIG. 6.2. The first load σ_1 leads to a strain ε_1 on the surface of the material. Inside the material, strain decreases down to zero at $x=l_1$. After the second impact with the same amplitude, the surface strain increases to ε_2 and the strain profile is translated into the material up to $x=l_2$. Eq. 6.5 defines ε_2 as a function of W_2.

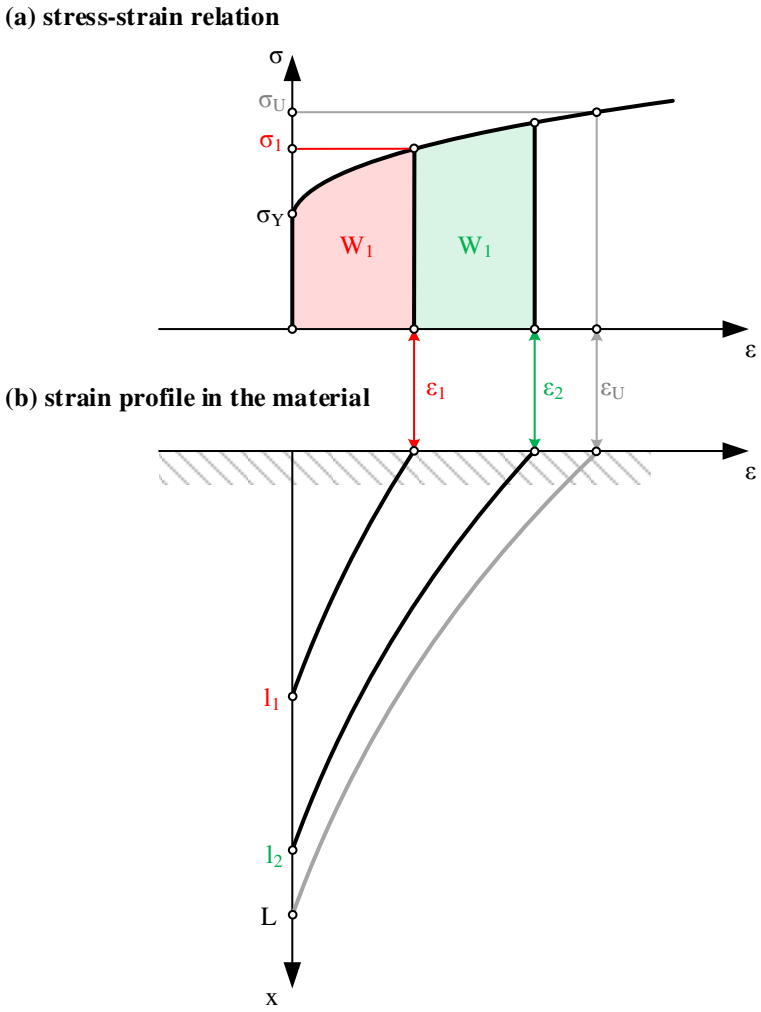

FIG. 6.2. Material response to two successive loads with surface stress σ_1 and absorbed energy W_1. (a) Stress strain relation. (b) Stress profile inside the material. Adapted from Ref. 35. Copyright 2009 by ASME.

6.1.2 Estimation of Incubation Time

In the following, the area S will be treated as a constant for all impacts. This is an assumption at this point and will be motivated in chapter 6.1.3. Through Eq. 6.5 every load amplitude σ can now be connected to an energy absorbed by the material, see FIG. 6.3 (a). According to the model assumptions, the energy is zero for $\sigma \leq \sigma_Y$ and growths with increasing σ. If the number of loads N together with the

amplitude of each load occurring in the area A and within a time interval Δt is known, the energy transmitted into the material per unit time and unit area $\dot{W}$ can be computed as

$$\dot{W} = \frac{1}{A\Delta t}\sum_{n=1}^{N} W_n(\sigma_n)\,. \tag{6.8}$$

In this work, the temporal rate of loads will be characterized by a functional correlation of an impact load spectrum (see chapter 6.1.4). In FIG. 6.3 (b) an example of a cumulative impact load spectrum is plotted (green line). We assume the cumulative rate of events $\dot{N}(\sigma)$ decays exponentially with σ as

$$\dot{N} = \dot{N}_0 \exp\left(-\frac{\sigma}{\sigma_0}\right). \tag{6.9}$$

Here $\dot{N}_0$ is a characteristic rate of events and p_0 is a characteristic amplitude. Note that the unit of $\dot{N}(\sigma)$ and N_0 is events per unit time and unit area. Combining the energy of a single load and the rate of events gives the energy transmitted into the material per unit time and unit area at a given amplitude, $\dot{W}(\sigma)$ (red line). No energy is transmitted per time by events with $\sigma \leq \sigma_Y$, regardless of the temporal rate. For loads close to σ_Y, the increase of $W(\sigma)$ is dominant compared to the decrease of $\dot{N}(\sigma)$ and consequently $\dot{W}(\sigma)$ rises. For high loads, the exponential decay of $N(\sigma)$ becomes dominant and $\dot{W}(\sigma)$ converges to zero. The local maximum corresponds to an optimum in terms of transmitted energy.

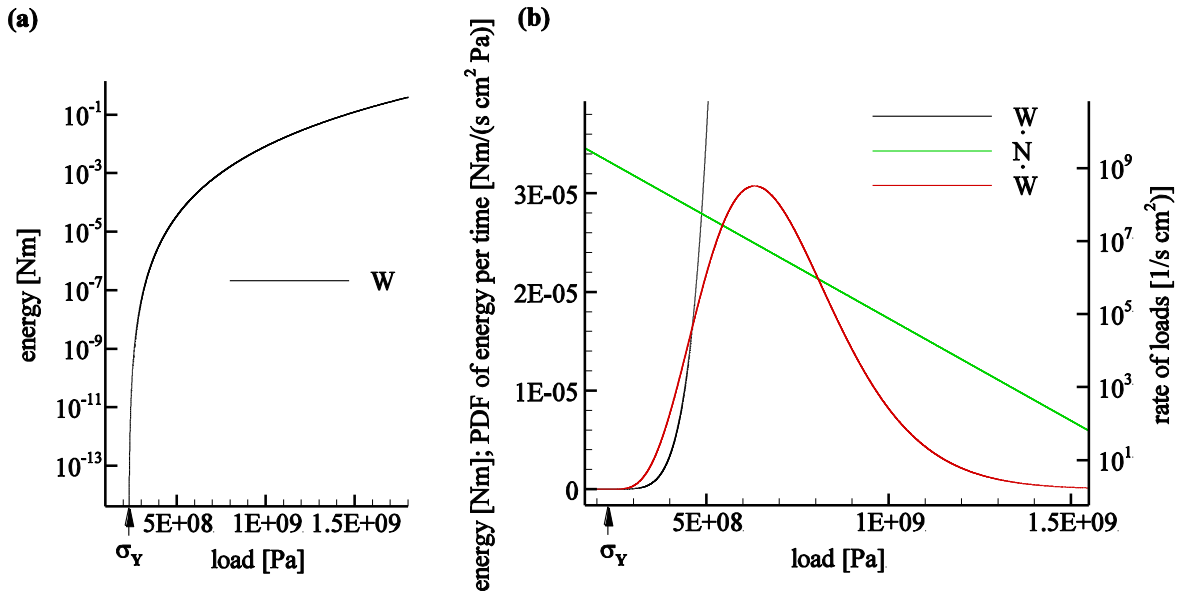

FIG. 6.3. (a) Energy of a single load W. (b) W together with typical impact load spectrum $\dot{N}$ and the PDF of the energy transmitted by a load-strength per unit time and unit area $\dot{W}$.

The energy transmitted by the whole spectrum per unit time and unit area can be computed by integrating

$$\dot{W} = \int_{\sigma_Y}^{\sigma_{\max}} W(\sigma) \frac{d\dot{N}(\sigma)}{d\sigma} d\sigma \,. \tag{6.10}$$

The upper boundary for integration σ_{max} corresponds to the highest load that occurs and will be discussed in chapter 6.1.4.

No material failure is expected as long as the strain on the surface is smaller than the ultimate strain, $\varepsilon<\varepsilon_U$. The superficial material layer starts to fail when $\varepsilon=\varepsilon_U$. This defines the end of the incubation period. The energy absorbed by the material until this point can be calculated using Eq. 6.5 for $\varepsilon=\varepsilon_U$. Expressed as energy per unit area, the incubation energy W_{inc} computes

$$W_{inc} = \varepsilon_U L \frac{\sigma_Y + \beta K \varepsilon_U^n}{1+\theta} \,. \tag{6.11}$$

With the energy transmitted into the material per time and area, $\dot{W}$, (Eq. 6.8 or Eq. 6.10) the incubation time t_{inc} then is given by

$$t_{inc} = \frac{W_{inc}}{\dot{W}} = \frac{f(material consts.)}{f(p_0, N_0, material consts.)} \,. \tag{6.12}$$

For a given material, t_{inc} depends only on p_0 and $\dot{N}_0$, which define the load profile. FIG. 6.4 (a) shows iso-lines of t_{inc} depending on the two parameters. The marked points A and B define two combinations of p_0 and $\dot{N}_0$ that lead to the same incubation time. The corresponding cumulative load spectra and energy intake per unit time and unit area are plotted in FIG. 6.4 (b). While in case A most energy is provided by comparatively weak loads with high rates, energy is transmitted by comparatively strong events with lower rates in case B. In the following two chapters, the extraction of p_0 and $\dot{N}_0$ from simulation data will be discussed.

6.1.3 Determination of Erosion Aggressiveness from Numerical Data

In the original model, the aggressiveness of the cavitating flow is obtained experimentally, characterized by the mean amplitude of a load $\bar{\sigma}$, the mean surface of a load $\bar{S}$, and the temporal rate of loads $\dot{N}$.[35] All three parameters are obtained from pitting tests. The amplitude of a single load is estimated from the depth of the corresponding pit, the surface the load acts on is defined by the pit diameter. Averaging procedure is arithmetic for $\bar{S}$ and based on energy considerations for $\bar{\sigma}$.[35]

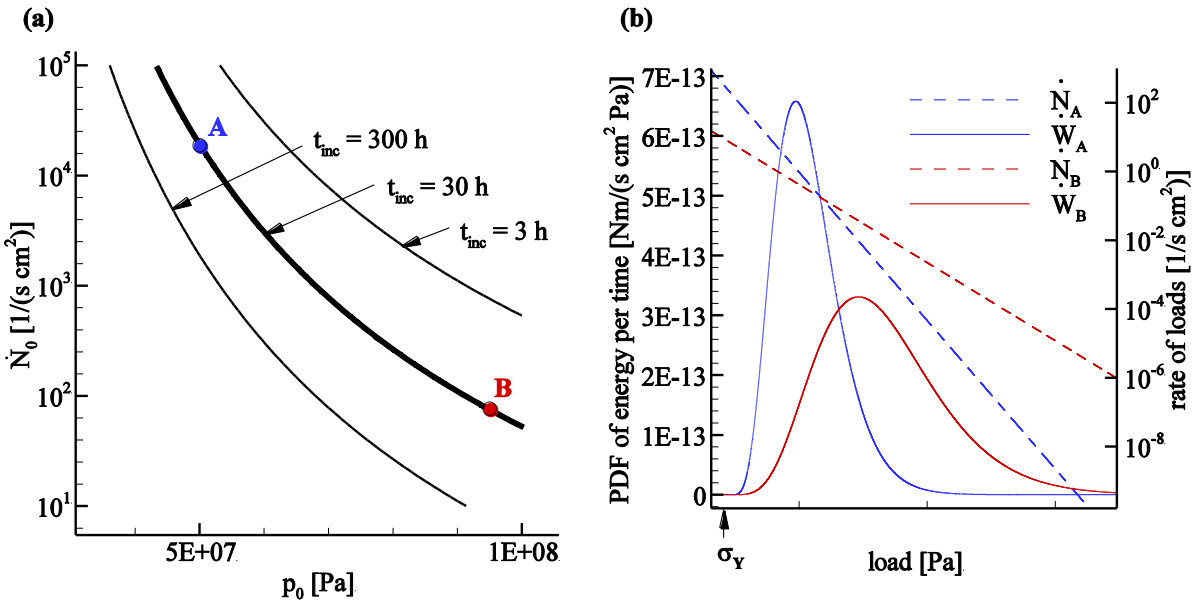

FIG. 6.4. (a) Iso-lines of incubation time in dependence of the load spectrum defined by p_0 and N_0. (b) Load spectra and PDF of energy per unit time and unit area for A and B in (a). Material is SS-316L (see chapter 6.1.5).

In this work the aggressiveness is derived from numerical simulations. We use data acquired by the collapse detector. Instead of a representative mean load, the whole load spectrum is taken into account. As shown in chapter 5, scaling laws are applied to the event rate and the collapse pressure, Eq. 4.9 and Eq. 5.7 respectively. With application of Eq. 4.9, the intensity of a collapse event is evaluated at the distance $x_{ref,p}$ from the collapse center in the entire fluid domain, see FIG. 6.5. To evaluate the intensity at a solid boundary at a distance d we extend the scaling law

$$p_{project} = \frac{\sqrt[3]{V_{cell}}}{\max(x_{ref,p}, d)} p_{collapse} = \sigma \,. \tag{6.13}$$

The resulting projected collapse pressure $p_{project}$ is taken as an estimate for the stress σ which is induced on the material surface.

Both scaling laws incorporate a reference length scale. In section 5.5.1, $x_{ref,N} = 181 \cdot 10^{-6}$ m was identified for the current flow problem. $x_{ref,p}$ could not be calibrated with the experimental data available. In the following we use $x_{ref,p} = x_{ref,N}$ as a model assumption.

Impact load spectra are evaluated locally in individual control volumes. The volumes are ring-shaped and have a constant thickness of 2mm, see FIG. 6.6 (a). Thus, for the collapse spectrum at e.g. r=27mm, collapse events with 26mm<r<28mm are taken into consideration. FIG. 6.6 (b) and (c) shows resulting local impact load spectra for different radial positions.

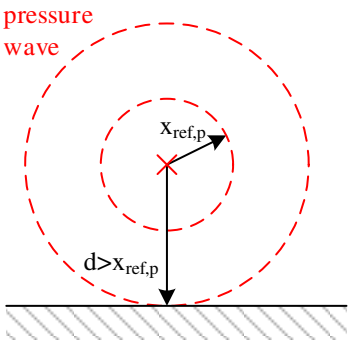

FIG. 6.5. Sketch of a collapse-induced pressure wave near a wall.

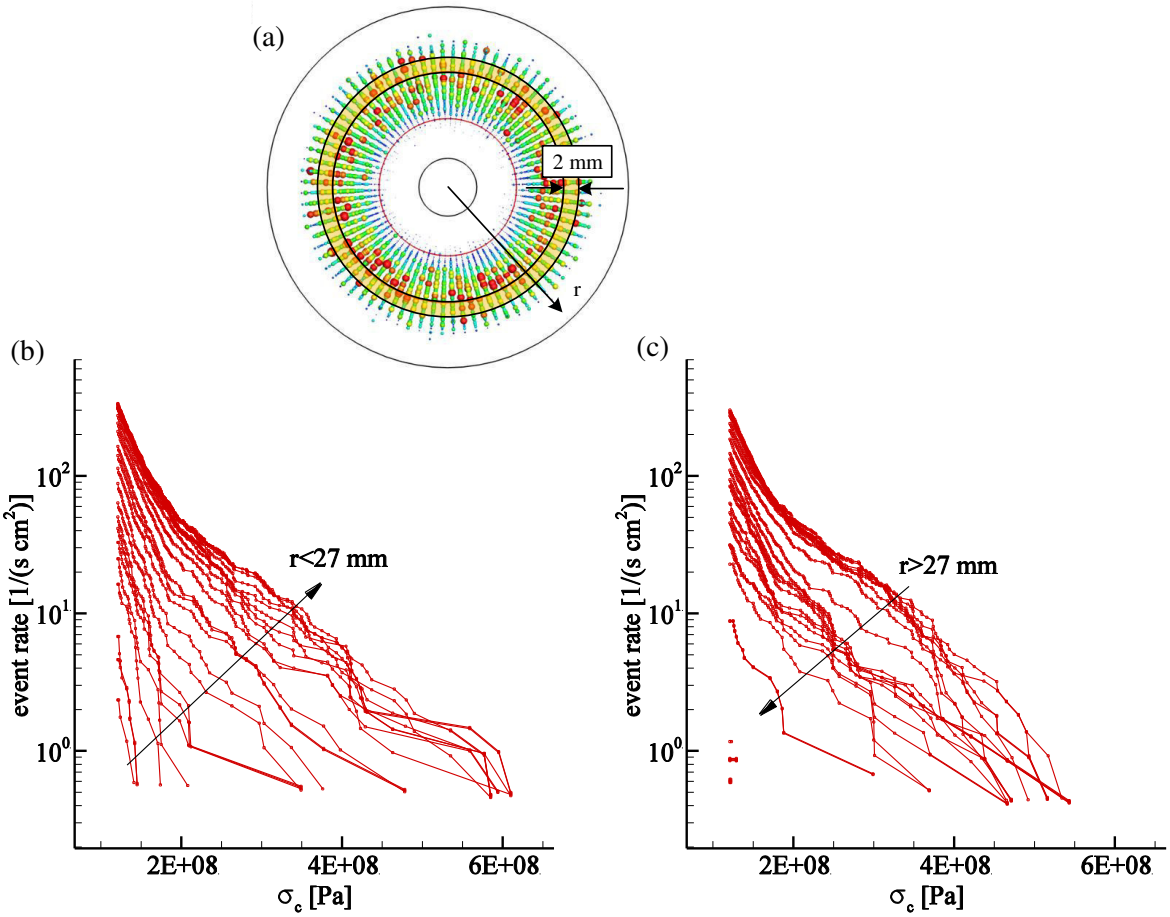

FIG. 6.6. (a) Sketch of control volumes for evaluating collapse events. (b) and (c): resulting local impact load spectra for individual control volumes.

6.1.4 Extrapolation of Impact Load Spectra to Larger Timescales

FIG. 6.7 shows a typical numerically acquired local impact load spectrum acquired after approximately 10s simulated physical time on the coarse grid (green scatter). Additionally, the PDF of

the transmitted energy $\dot{W}(\sigma)$ is plotted (red scatter). The spectrum decays exponentially and is extrapolated for higher loads by a fitting function (green line)

$$\dot{N}(\sigma) = \dot{N}_0 \exp\left(-\frac{\sigma}{\sigma_0}\right), \tag{6.14}$$

where $\dot{N}_0$ is a characteristic rate and σ_0 is a characteristic intensity. The corresponding energy per unit time and unit area (red line) illustrates that the spectrum computed by the simulation (red scatter) covers only a part of the energy-transmitting range of collapse strengths. To account for this, we use the exponential fit as input for the material. The fitting algorithm is based on least squares.

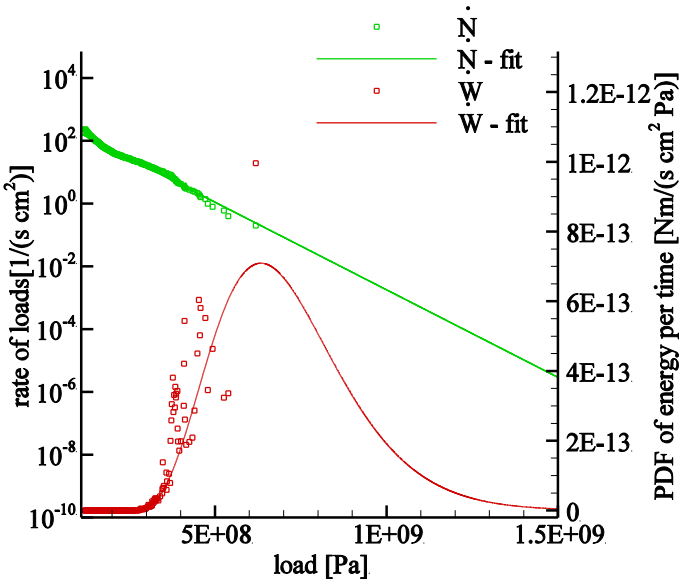

FIG. 6.7. Example of impact load spectrum (green) and PDF of transmitted energy per unit time and unit area (red). Scatter: simulation data after 10s physically simulated time. Lines: fit.

Obviously, a collapse-induced load cannot have an infinitely high amplitude. Therefore it seems reasonable to introduce a maximum intensity σ_{max} and corresponding minimum rate $\dot{N}_{min}$. The cumulative rate Eq. 6.14 then reads[36]

$$\dot{N}(\sigma) = \dot{N}_0 \left[\exp\left(-\frac{\sigma}{\sigma_0}\right) - \exp\left(-\frac{\sigma_{\min}}{\sigma_0}\right)\right], \tag{6.15}$$

or recast as a function of $\dot{N}_{min}$

$$\dot{N}(\sigma) = \dot{N}_0 \left[\exp\left(-\frac{\sigma}{\sigma_0}\right) - \frac{\dot{N}_{\min}}{\dot{N}_0}\right]. \tag{6.16}$$

It is not trivial to obtain a reliable value for σ_{max} or $\dot{N}_{min}$, as from a mathematical point of view an infinitely long analysis interval would be necessary. The lowest rates observed in pitting tests in the experiment are between ≈ 0.05 and 0.005 1/(s cm^2). Lowest rates in the simulation are limited by the simulation time. Finally, extrapolating the spectrum to $\sigma_{max} \to \infty$ can be interpreted as conservative estimate for the incubation time.

6.1.5 Material Thresholds

Materials parameters are acquired by strain test and nano-indentation tests. Experiments have been performed using stainless steel 316 L (SS-316L),[35] duplex stainless steel 2205 (SS-A2205),[36,79] aluminum alloy 7075 (Al-7075),[36,79] and a Nickel Aluminum Bronze (NAB).[9,36] Corresponding material thresholds are listed in Table X and Table XI.

Table X: Material parameters from strain tests.

material	SS-316L[35]	SS-A2205[79]	Al-7075[79]	NAB[9]
σ_Y [N/m^2]	$4.0 \cdot 10^8$	$2.3 \cdot 10^8$	$5.3 \cdot 10^8$	$3.55 \cdot 10^8$
σ_U [N/m^2]	$10.2 \cdot 10^8$	$7.9 \cdot 10^8$	$6.53 \cdot 10^8$	$6.83 \cdot 10^8$
K [N/m^2]	$9.0 \cdot 10^8$	$9.1 \cdot 10^8$	$4.47 \cdot 10^8$	$12.1 \cdot 10^8$
n [-]	0.5	1/3.2	1/1.98	1/2.07

Table XI: Material parameters form nano-indentation tests.

	SS-316L[35]	SS-A2205[36]	Al-7075[36]	NAB[36]
L [m]	$200 \cdot 10^{-6}$	$1250 \cdot 10^{-6}$	$690 \cdot 10^{-6}$	$1070 \cdot 10^{-6}$
Θ [-]	5	2.2	2.0	2.8

6.2 Numerical Setup for Fluid Simulation

We simulate the setup introduced in chapter 5.1. Information about incubation times are available for two operating conditions: 20 bar and 40 bar system pressure. Boundary conditions are summarized in Table XII. Note, that compared to the calculations presented in chapter 5, the operating conditions in the experiment and consequently the boundary conditions in the simulation slightly differ for the 20 bar case (taken from Ref. 35). The barotropic equation of state introduced in section 3.3.2 is chosen as thermodynamic closure.

We perform a grid study for the 20 bar case, which we denote as reference configuration. Computational grids are identical to the setup analyzed in chapter 5. As discussed before, the computational cost to cover the same physical time interval increases by a factor of 16 per refinement level (8 times the number of cells and half the time step size). Usually this can be compensated by distributing the computation on multiple CPUs. While the applied code allows parallel computation in space, parallelization in time is not possible. Thus, the decreasing time step acts as a limit when computing long time intervals on high resolutions.

To bypass this limit, we utilize the grid sequencing technique as sketched in FIG. 6.8. The simulation is started from initialization and advanced in time on the coarsest resolution. After a developed solution is established, the flow field is interpolated onto the next finer resolution. Here, again the flow exhibits a transient, which has to be computed before a developed solution is established. The length of the interval is, however, significantly shorter compared to when starting from the initialization at the finer grid. Afterwards, statistical data can be collected on both grids. As the coarse grid advances in time faster, the interpolation routine can be repeated for later time instants, which have not been reached on the finer grid. Thus, several computations on the finer grid level can be run in parallel. The technique was used for the fine grid resolution in this investigation, but can also be applied to cover several grid levels.

Table XII: Boundary conditions.

operating condition	20 bar	40 bar
u_{in} [m/s]	1.05	1.37
p_{out} [bar]	10.1	18.9

Table XIII: Analyzed physical time interval.

	coarse	medium	fine
20 bar case	≈ 10.6 s	≈ 0.86 s	≈ 0.12 s
40 bar case	≈ 10.5 s	-	-

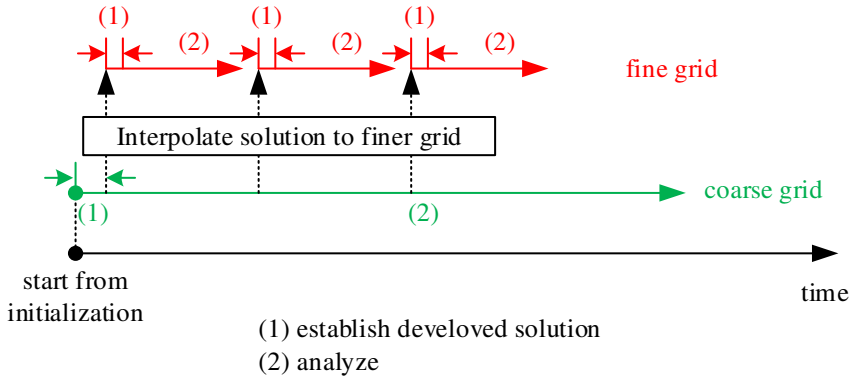

FIG. 6.8. Grid sequencing technique.

6.3 Results

In the following, the numerically estimated incubation times are presented. The first part contains a grid study for the reference case (20 bar system pressure and material SS-316L) from Ref. 35. In the second part, the operating condition is changed to a higher system pressure and a variation of three different materials is discussed.

6.3.1 20 bar case – SS-316L

For every radial position, a numerical impact load spectrum is derived from the collapse events recorded during flow simulation. In FIG. 6.10 (a), the temporal evolution of an impact load spectrum on the coarse grid is shown for r = 33 mm. For every radial position, the spectra are characterized by a characteristic load σ_0 and a characteristic rate $\dot{N}_0$. The time evolution of the two parameters is shown in FIG. 6.10 (b)-(f). For longer simulation time intervals lower rates are captured and the determination of σ_0 and $\dot{N}_0$ is based on a bigger dataset. Consequently, scatter decreases with time for combinations of σ_0 and $\dot{N}_0$, which correspond to the lowest incubation times (marked for the longest interval, FIG. 6.10 (f)).

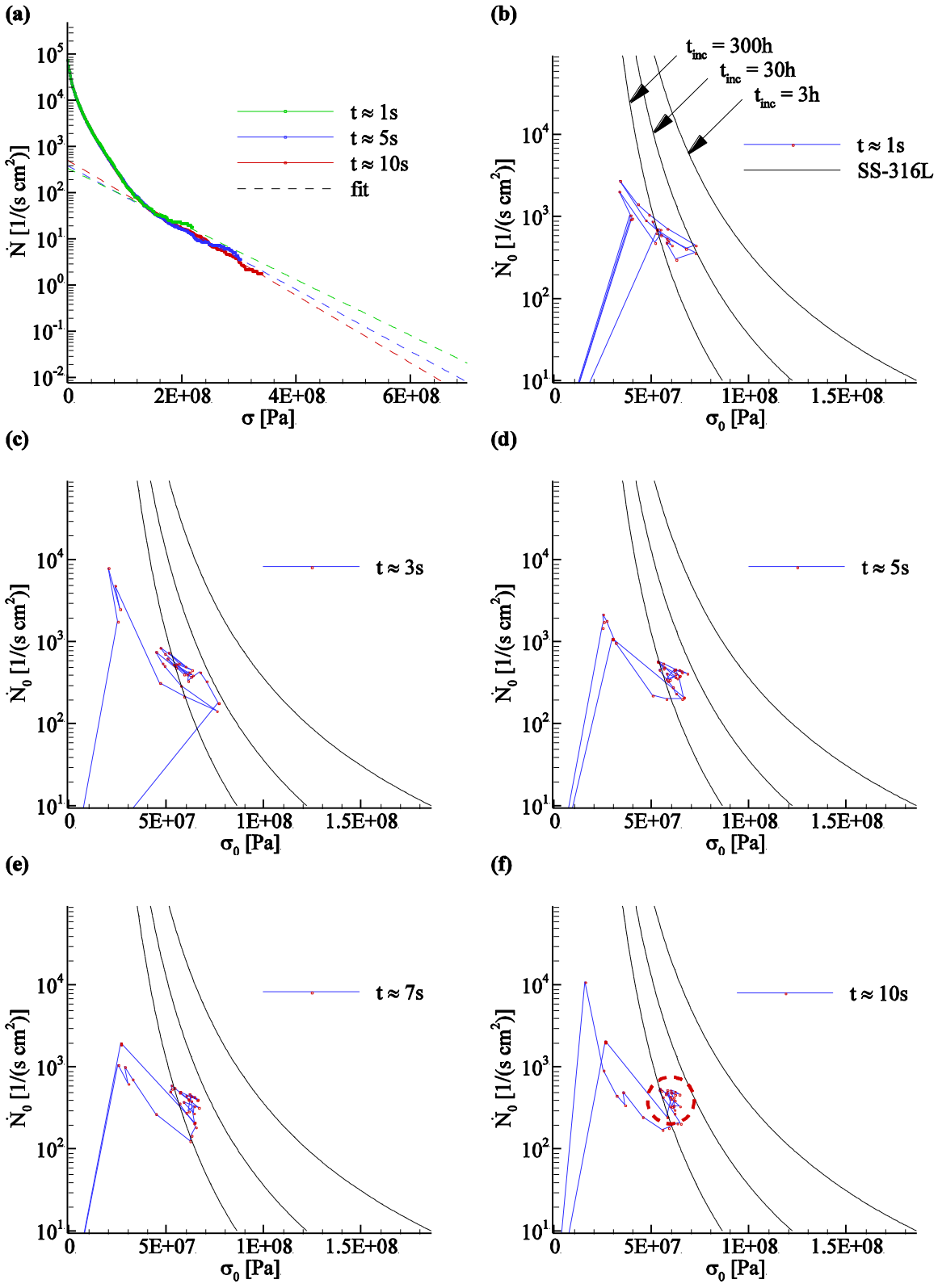

FIG. 6.9. (a) Impact load spectra after different time intervals on the coarse grid at $r = 33$ mm. Only load amplitudes that occurred at least 10 times are taken into account. (b)-(f) Temporal evolution of $\dot{N}_0$ and σ_0 for radii 19 mm < r < 42 mm on the coarse grid. Iso-lines of incubation time correspond to the material SS-316L. With simulation time, lowest values for t_{inc} converge (marked in (f))

FIG. 6.10 shows σ_0 and $\dot{N}_0$ for different numerical grids. For a higher resolution, scatter increases due to the shorter simulated time interval. All grids, however, scatter around values which corresponds to an incubation time of 3-300 h.

The radial distributions of predicted incubation times are presented in FIG. 6.11. All graphs show a global minimum between 20 mm and 40 mm. Superimposed to this global behavior is local scatter, which increases with grid resolution and decreases with simulated time. The lowest predicted incubation times are $t_{inc,coarse}$ = 108 h, $t_{inc,medium}$ = 59 h, $t_{inc,fine}$ = 4.9 h and lie within an order of magnitude from the experimental value (30h). The position of the lowest predicted incubation time corresponds to the position where first material damage is expected. Compared to the experiment ($r \approx 25$ mm) the value is overestimated on all grid levels ($r_{dmg,coarse}$ = 33 mm, $r_{dmg,medium}$ = 35.5 mm, $r_{dmg,fine}$ = 34.5 mm).

The lowest predicted incubation time is of special interest as a design variable. FIG. 6.12 shows the evolution of the lowest incubation time with the simulated physical time interval in a double-logarithmic plot. The simulated time interval covers grid-dependent interval-lengths. The figure shows a converging behavior towards a value around 100 h, which is slightly higher than the experiment. The plot demonstrates that the grid-dependency of the predicted incubation time observed in FIG. 6.11 is most likely due to the difference in the simulated time interval for each grid level.

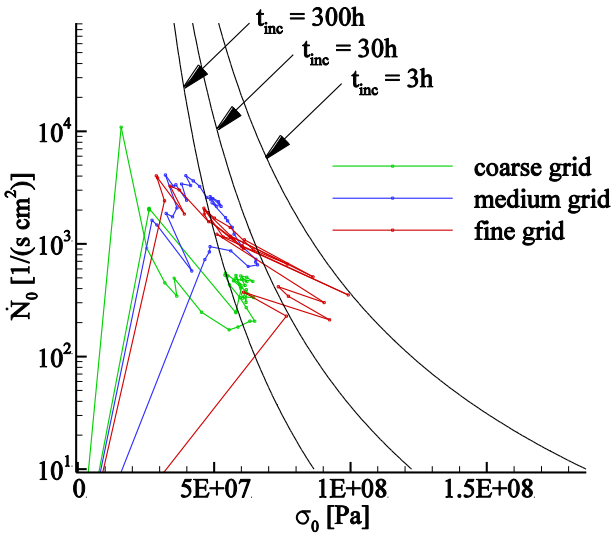

FIG. 6.10. $\dot{N}_0$ and σ_0 for radii 19 mm < r < 42 mm for different spatial resolutions. Simulated time interval varies for grid resolutions: $\Delta t_{coarse} \approx$ 10s, $\Delta t_{medium} \approx$ 0.86 s, $\Delta t_{fine} \approx$ 0.12 s.

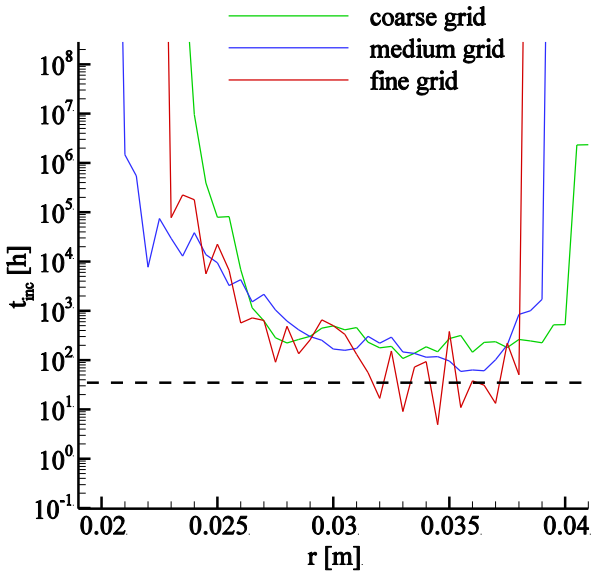

FIG. 6.11. Predicted incubation times for different spatial resolutions. Simulated time interval varies for grid resolutions: $\Delta t_{coarse} \approx 10$s, $\Delta t_{medium} \approx 0.86$ s, $\Delta t_{fine} \approx 0.12$ s. The dashed line represents the incubation time in the experiment (30h). The lowest predicted incubation times are $t_{inc,coarse}$ = 108 h, $t_{inc,medium}$ = 59 h, $t_{inc,fine}$ = 4.9h.

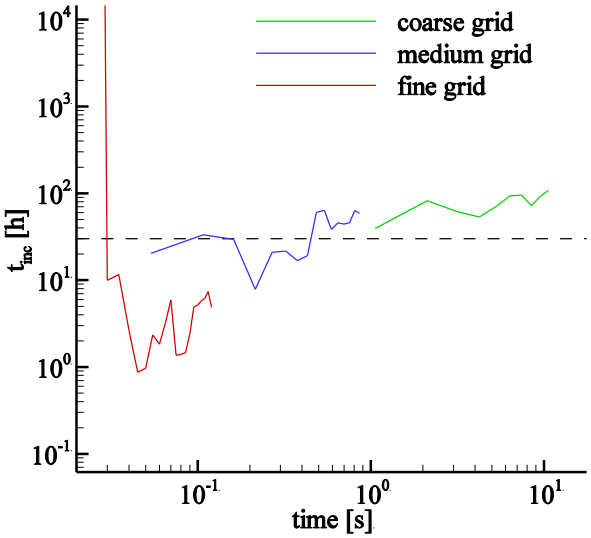

FIG. 6.12. Time evolution of lowest predicted incubation time for different spatial resolutions. The dashed line represents the incubation time in the experiment (30h).

6.3.2 40bar case – Variation of Material

For the higher system pressure of 40 bar, experiments with three different materials are available.[86] The erosive potential of the flow is determined numerically on the coarse grid. Incubation times are then estimated with the acquired impact load spectra for different material thresholds. FIG. 6.13 shows values of σ_0 and $\dot{N}_0$ representing the impact load spectra at different radial positions. Parameter combinations

representing the lowest incubation times lie in an interval between the experimental incubation time and approximately one order of magnitude lower.

The distributions of predicted incubation times over the radius are presented in FIG. 6.14. The lowest predictions are $t_{inc,SS}$ = 3.8 h, $t_{inc,Al}$ = 0.6 h, $t_{inc,NAB}$ = 1.4 h and lie approximately one order of magnitude below the experimental values. The predicted positions of first damage is r = 33 mm for all materials.

The time evolution of the lowest predicted incubation time, FIG. 6.15, shows faster convergence compared to the 20 bar case because of a higher shedding frequency and thus more statistical data. Although absolute values are overestimated, the relative offset is captured according to the experiment.

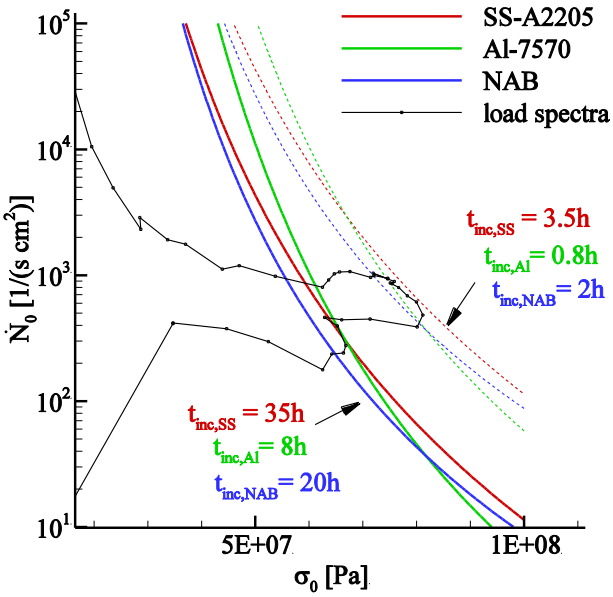

FIG. 6.13. $\dot{N}_0$ and σ_0 for radii 19 mm < r < 42 mm. Solid iso-lines of incubation time correspond to the values from the experiment (t_{SS} = 35 h, t_{Al} = 8 h, t_{NAB} = 12 h), dashed iso-lines correspond to one order of magnitude lower incubation times.

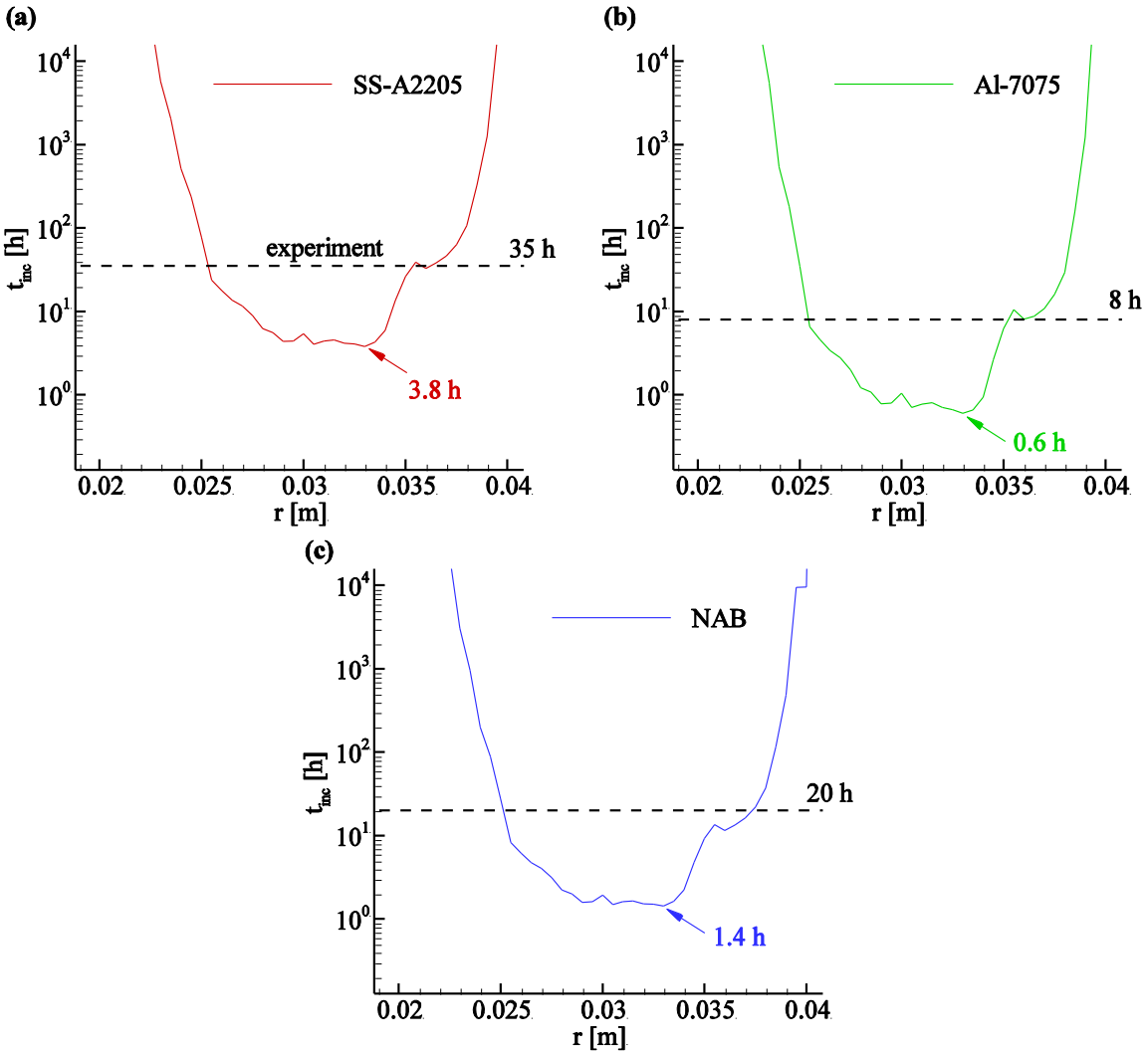

FIG. 6.14. Predicted incubation times for different materials. (a) SS A2205 (b) Al 7075 (c) NAB. Dashed lines correspond to incubation times in the experiment. Lowest predicted incubation times are $t_{inc,SS}$=3.8 h, $t_{inc,Al}$=1.4 h, $t_{inc,NAB}$=8h. The position of the lowest incubation time is r_{dmg}=33 mm for all materials.

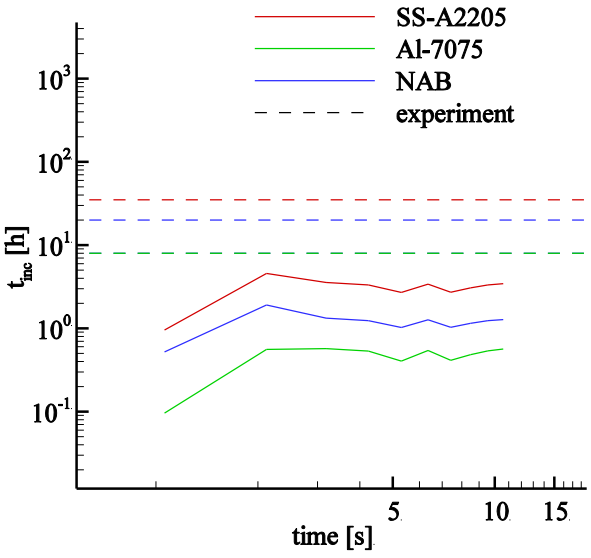

FIG. 6.15. Time evolution of lowest predicted incubation time for different materials. Dashed lines correspond to the incubation times in the experiment.

6.4 Conclusion

With the developed material model, reasonable incubation times can be derived from impact load spectra obtained with numerical simulations. The potential of the approach was demonstrated for two different operating conditions and four different materials. In particular, the relative difference between different materials for one operating conditions was predicted. The proposed method is a tool to evaluate the erosive potential of a flow as a design variable which can be used within the development process of new products.

Some limitations remain. The load spectra acquired in the fluid simulation are scaled by two scaling laws which contain two reference length scales, $x_{ref,N}$ and $x_{ref,p}$, that need to be identified. For $x_{ref,N}$, temporally resolved information on the load spectra is needed. While calibration was performed in chapter 5 for the present testcase, it can not be assumed that the determined value applies to other setups in general. For calibration of $x_{ref,p}$, spatially resolved information about the load spectrum is needed, which is not available for the present testcase. Although spatially resolved information of the load spectrum of a cavitating flow might be a demanding task in general due to limited sensor size, promising advances have been reported, e.g. in Ref. 87. With a proper calibration of $x_{ref,p}$, quality of predictions might further improve.

Another limiting factor is the long analysis interval that needs to be computed by the fluid simulation. Extrapolating load spectra to bigger timescales based on information of smaller time intervals is a promising approach when the behavior of the spectra is known. Furthermore, the material model itself contains some simplifications like static material values or disregarding the spatial distribution of a single load. Here, promising progress has been reported in Ref. 36. Finally, the applied material model is restricted to materials that undergo work hardening.

7 Solved and Free Gas Content

Most technical liquids contain gas, which can either be solved, or unsolved in the form of microbubbles. Free gas content can noticeably affect the behavior of a cavitating flow, e.g. by influencing compressibility of the liquid phase, or by damping single collapses. Both effects can affect the erosive potential of the flow. To model these effects accurately in numerical simulations it is mandatory to know the amount and distribution of gas in the system.

It is known that gas can get solved in a liquid or released from a liquid, depending on pressure, at a phase boundary by diffusion. Iben *et al.*[30] additionally showed a strong coupling of cavitation and degassing. In the following chapter this coupling is investigated.

7.1 Testcases and Experimental Data

Interaction of cavitation and degassing has been investigated experimentally for two nozzle geometries in Refs. 30 and 31. Both setups consist of an axisymmetric inlet and nozzle, see FIG. 7.1. Diameter ratio of inlet and nozzle, as well as the geometry downstream of the nozzle differ in both setups. Case A has a ratio of 10:1 and an axisymmetric geometry after the nozzle which has a bigger diameter than the inlet. Case B has a ratio of 20:1 and a rectangular outlet cross section, which has a smaller diameter than the inlet. Additionally, the nozzle of case B is twice as long as the nozzle of case A.

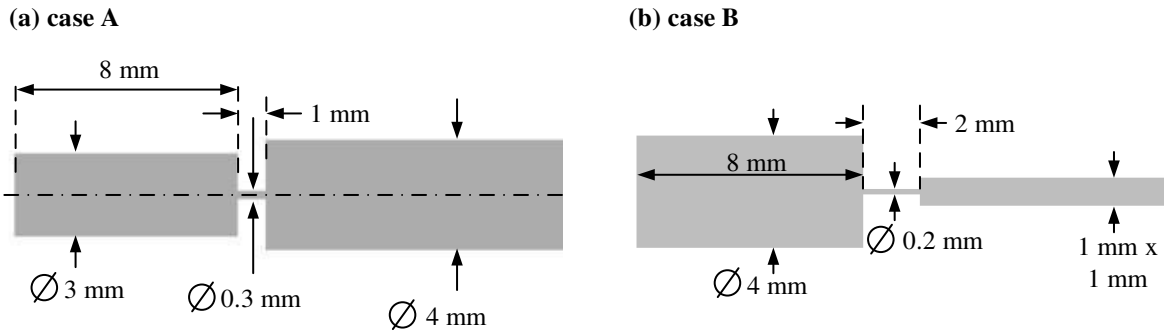

FIG. 7.1. Sketch of the experimental setups. (a) Case A. (b) Case B.

For both setups, the inlet pressure, the pressure downstream of the nozzle, and the massflow are available from the experiment. Additionally, solved gas content before the nozzle and free gas content downstream of the nozzle were measured. Measurement procedures are summarized in Ref. 31 While in case A properties downstream of the nozzle are measured downstream of the whole setup, in case B measurements are available at 100 mm (position 1), 300mm (position 2), and 500 mm (position 3) downstream of the nozzle exit.

Operating conditions are chosen as follows. The massflow is kept constant during the experiment, while the outlet pressure is decreased until the nozzle cavitates and is choked. Further decreasing the outlet pressure leaves the inlet pressure approximately constant. For both setups, measurements are available featuring inlet pressures of 75 bar, 50 bar, 25 bar, and 15 bar. For each inlet pressure various outlet pressures have been investigated. In the following, experimental findings and especially the role of diffusion are discussed before presenting numerical results.

7.1.1 Role of Diffusion

For case B the amount of free gas was measured at position 1 and position 2, see FIG. 7.2. For all operating conditions, a larger amount of free gas is measured at position 1. In the following, analytical considerations will show that the underlying physical mechanism is solution of free gas by diffusion. In a second step, the free gas content directly downstream of the nozzle is estimated.

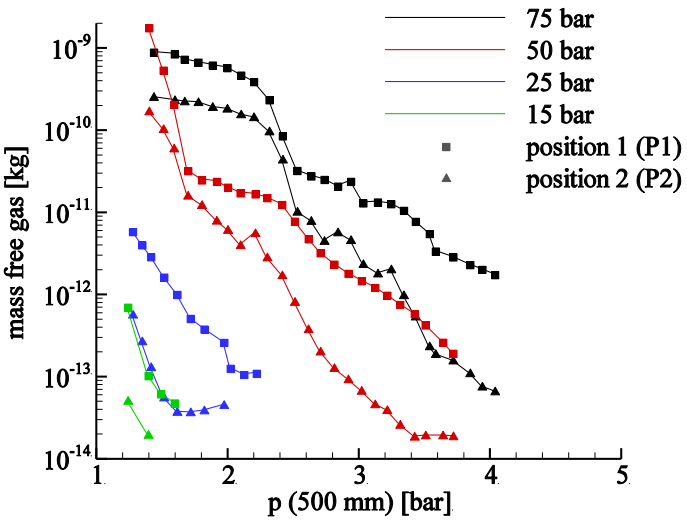

FIG. 7.2. Mass of free gas 100 mm (position 1) and 300 mm (position 2) downstream of the nozzle exit plotted as function of outlet pressure. Color indicates inlet pressure; symbols indicate position of gas measurement.

The mass Δm_4 of free gas that is solved in a liquid through diffusion depends on the driving concentration difference Δc, the interfacial area A, the time interval Δt, and a diffusion constant D (see e.g. Ref. 88)

$$\Delta m_4 = D \cdot \Delta c \cdot A \cdot \Delta t \,. \tag{7.1}$$

The concentration difference Δc can be expressed by the difference of static and saturation pressure $p_{sat,gas}$. In the experiment, the fluid is saturated with gas at an ambient pressure of $p_{atm} \approx 1$ bar. The

corresponding mass fraction of gas is $\varepsilon_{g,tot}$. Downstream of the nozzle, the saturation pressure at position 1, $p_{sat,gas}(p1)$ is

$$p_{sat,gas}(p1) = p_{atm}\frac{\varepsilon_{g,tot} - \varepsilon_4(p1)}{\varepsilon_{g,tot}}, \tag{7.2}$$

where ε_1(p1) is the mass fraction of free gas at position 1. A simple approximation for the pressure and the free gas content between position 1 and 2 is the arithmetic mean of the two known values. Thus, Δc is

$$\Delta c = \Delta p = \frac{p(p1) + p(p2)}{2} - p_{atm}\frac{\varepsilon_{tot} - \frac{\varepsilon_4(p1) + \varepsilon_4(p2)}{2}}{\varepsilon_{g,tot}}. \tag{7.3}$$

The arithmetic mean of the cumulative gas bubble surfaces at position 1 and 2 are an estimate for the interfacial area A.

$$A = \frac{A(p1) + A(p2)}{2}. \tag{7.4}$$

The time interval Δt is proportional to the massflow rate $\dot{m}$ and is given by

$$\Delta t \propto \frac{1}{\dot{m}}. \tag{7.5}$$

The proportionality constant (1/(density x diameter x length)) is considered by D. Finally, the mass of free gas at position 2 can be estimated as

$$m_4(p2) = m_4(p1) - \Delta m_4. \tag{7.6}$$

The obtained values for $m_4(p2)$ are compared to measurements from the experiment for different diffusion constants D. FIG. 7.3. shows results of the estimation for a constant D where estimated and experimental $m_4(p2)$ agree best.

At 75 bar and 50 bar inlet pressure, FIG. 7.3. (a) and (b), results of estimated and measured $m_4(p2)$ collapse for moderate outlet pressures. For low outlet pressures Δm_4 is underestimated. However, the optical bubble detection in the experiment has the highest uncertainty in this regime.[31] For high outlet pressures Δm_4 is overestimated. This might be due to an overestimation of the interfacial area as complete solution of single bubbles is not taken into account in the arithmetic mean in Eq. 7.4.

The simple analytical estimation shows, that the offset in the free gas content between position 1 and 2 can be explained by diffusion. As diffusion is not modelled in the simulation, the same approach is used to estimate the free gas content directly downstream of the nozzle (0 mm). The mass of free gas that gets solved between the nozzle and position 1 is again calculated with Eq. 7.1. No quantities directly downstream of the nozzle are known in the experiment. Eq. 7.3 and 7.4 thus become

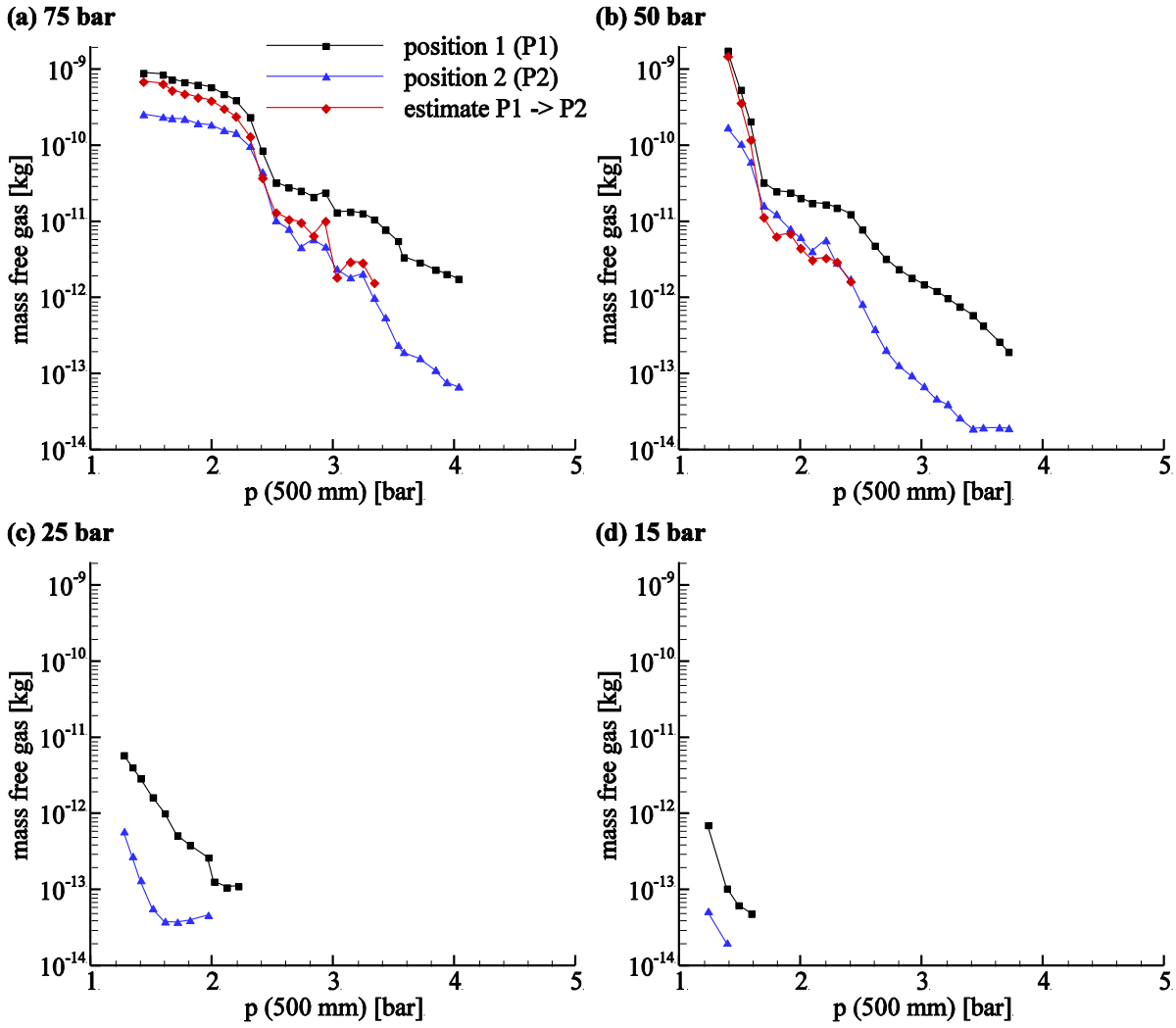

FIG. 7.3. Mass of free gas at 100 mm (position 1) and 300 mm (position 2) downstream of the nozzle depending of the downstream pressure. (a) – (d): variation of inlet pressure. Data points where all gas has been solved do not appear in the log-scale ($m_4(p2)$=0).

$$\Delta c = p(p1) - p_{atm}\frac{\varepsilon_{g,tot} - \varepsilon_4(p1)}{\varepsilon_{g,tot}}, \tag{7.7}$$

and

$$A = A(p1). \tag{7.8}$$

The distance between nozzle exit and position 1 corresponds to half the distance from position 1 to position 2, thus

$$\Delta t_{nozzle->p1} = 0.5\,\Delta t_{p1->p2}. \tag{7.9}$$

The mass of free gas downstream of the nozzle finally is

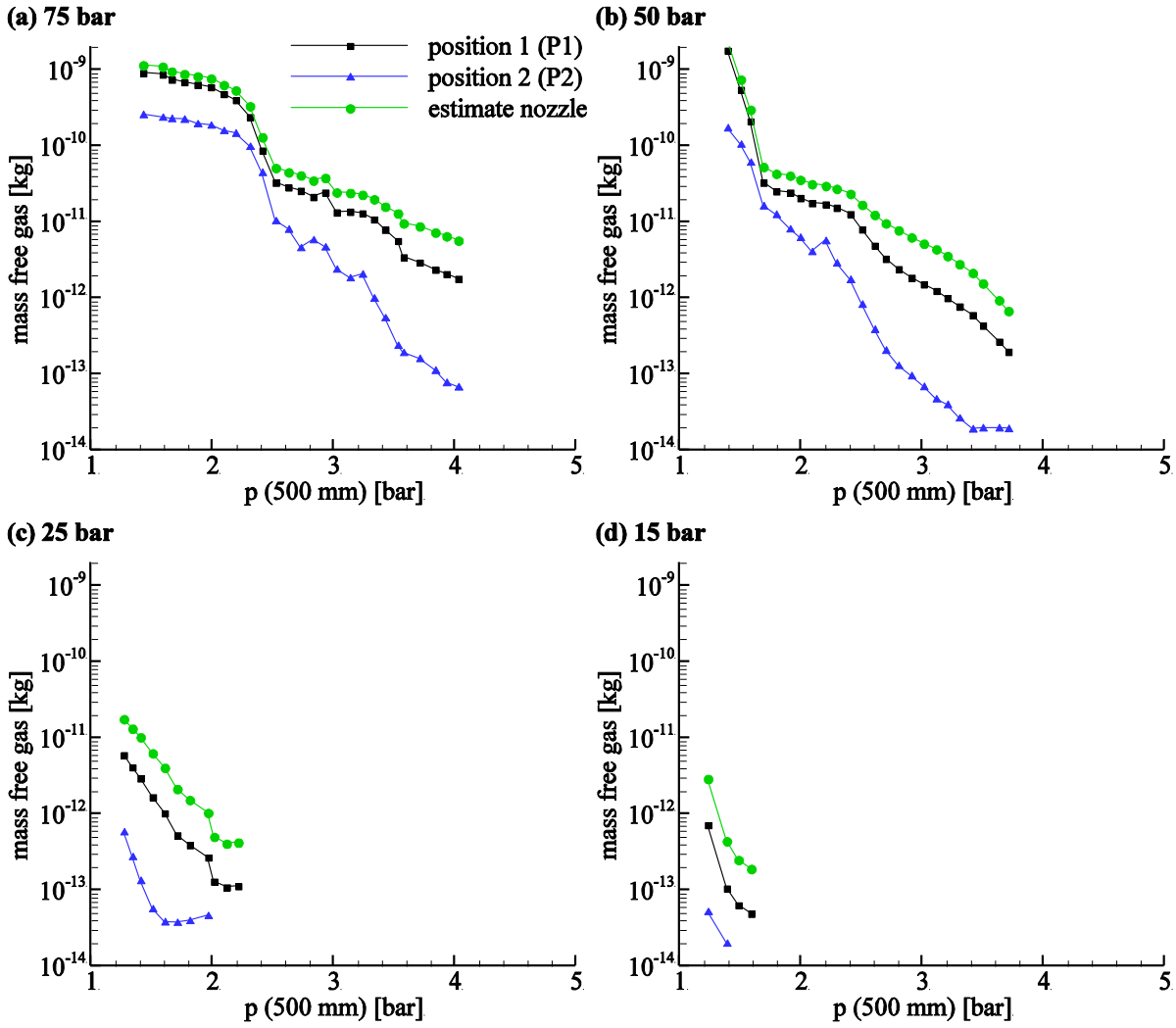

FIG. 7.4. Mass of free gas directly downstream of the nozzle and 100 mm (position 1) and 300 mm (position 2) depending of the downstream pressure for case B. (a) – (d): variation of inlet pressure. Data points where all gas has been solved do not appear in the log-scale ($m_4(p2)$=0).

$$m_4(nozzle) = m_4(p1) + \Delta m_4 . \tag{7.10}$$

Values from this analytical calculation are compared to simulation data, see FIG. 7.4. For case A, measurements of free gas are available at a single location 500 mm downstream of the nozzle. An estimation of the amount of free gas directly downstream of the nozzle is thus not possible. Pressure levels are comparable to case B, while the cross section downstream of the nozzle is larger. Consequently, the flow velocity is lower and free gas solves in the liquid over a longer time period. Compared to case B, simulations of case A are thus expected to overpredict the free gas content.

7.1.2 σ-Similarties

The cavitation number σ for nozzle flows was previously defined as

$$\sigma = \frac{p_{in} - p_{ref}}{p_{in} - p_{out}}, \tag{7.11}$$

where p_{in} und p_{out} are the static pressure before and downstream of the nozzle and p_{ref} is a reference pressure. For cavitating flows p_{ref} usually corresponds to the vapor pressure p_{sat}. For flows with a dominating effect of gas diffusion, the value of p_{ref} can be chosen as the pressure at which the liquid is saturated with solved gas. For the present case, p_{ref} is $p_{ref} = p_{atm} \approx 1$ bar.[30]

Case A shows similarity of the free gas content downstream of the nozzle for $\sigma(p_{atm})$, FIG. 7.5. (a). For FIG. 7.5 (b) no similarity is observed. This is an indication that diffusion has a stronger influence on the free gas content behind the nozzle, than cavitation. Case B shows a similar behavior, see FIG. 7.6. However, only the free gas content directly after the nozzle for three inlet pressures shows a strong similarity.

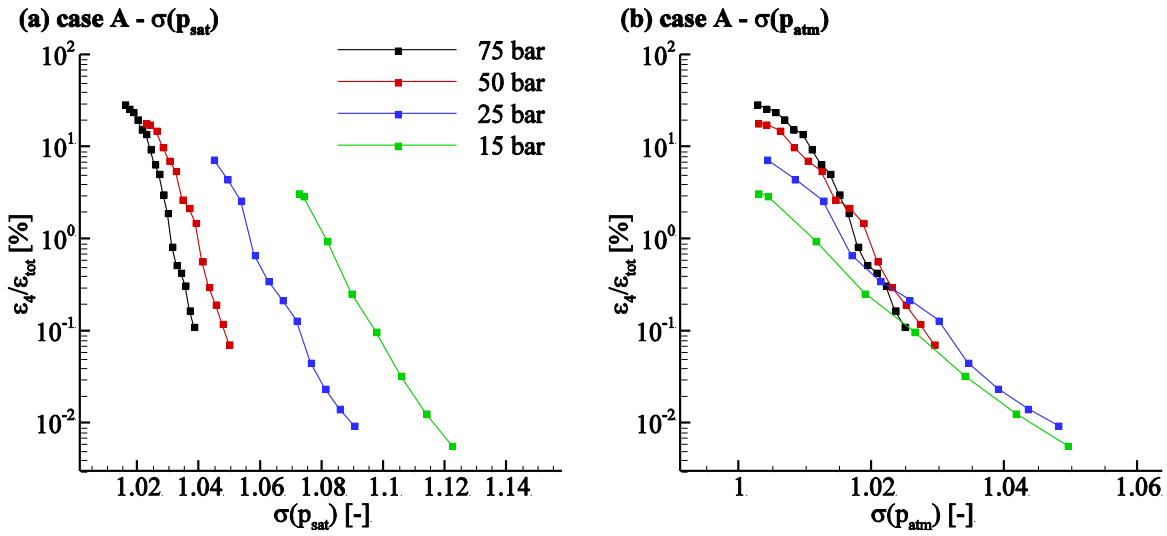

FIG. 7.5. Dimensionless free gas content $\varepsilon_4/\varepsilon_{g,tot}$ 500 mm downstream of the nozzle for case A depending on cavitation number σ. (a) $\sigma(p_{sat})$. (b) $\sigma(p_{atm})$.

7.2 Numerical Setup

For case A the entire setup is asymmetric with a diameter ratio of inlet to nozzle 10:1. The diameter downstream of the nozzle is larger than upstream. Diameter variations downstream of the nozzle are adapted from the experiment. The radially divergent gap and the adjacent reservoir are added to ensure that no vapor regions reach the outlet boundary. FIG. 7.7 shows the computational domain. We apply the thermodynamic model introduced in section 3.3.3. Parameters of the model are summarized in Table XIV.

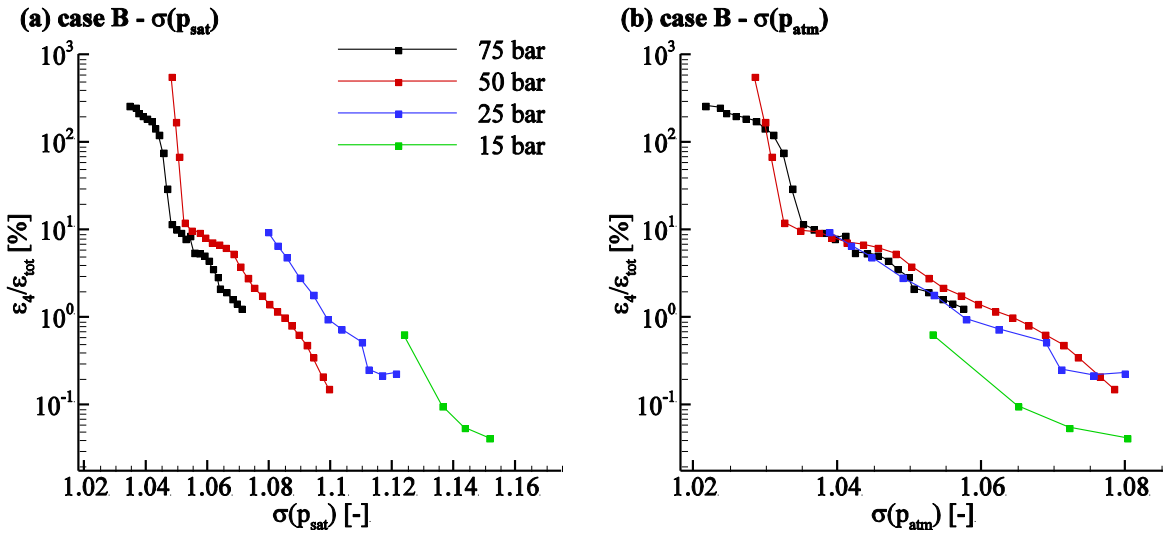

FIG. 7.6. Dimensionless free gas content $\varepsilon_4/\varepsilon_{g,tot}$ directly downstream of the nozzle for case B depending on cavitation number σ. (a) $\sigma(p_{sat})$. (b) $\sigma(p_{atm})$.

Table XIV: Parameters of the thermodynamic model.

	case A	case B
ρ_l	826 kg/m^3	819 kg/m^3
ρ_v	0.12 kg/m^3	0.017 kg/m^3
c_l	1363 m/s	1363 m/s
c_m	1.64 m/s	0.1 m/s
T_{ref}	293 K	293 K
$\varepsilon_{g,tot}$	$1.9713 \cdot 10^{-4}$	$1.69 \cdot 10^{-4}$
R_G	287.1 J/(kg·K)	287.1 J/(kg·K)

As inlet boundary conditions we prescribe a parabolic velocity profile that matches the experimental massflow rate. At the outlet, an asymptotic pressure boundary is prescribed. Parameters of all calculations are summarized in Table XV. One computation took about 40 hours on 233 CPUs (9320 CPUh).

For case B, inlet and nozzle are asymmetric with a diameter ratio of inlet to nozzle 20:1. The cross section downstream of the nozzle is rectangular and smaller than the inlet. As in case A, the radially divergent gap is added to ensure that no vapor regions reach the outlet boundary. FIG. 7.8 shows the computational domain.

Analogous to case A, the boundary conditions at the inlet and outlet are a parabolic velocity profile and an asymptotic pressure boundary, respectively. Parameters of all calculations are summarized in Table XVI. One computation took about 40 hours on 196 CPUs (7840 CPUh).

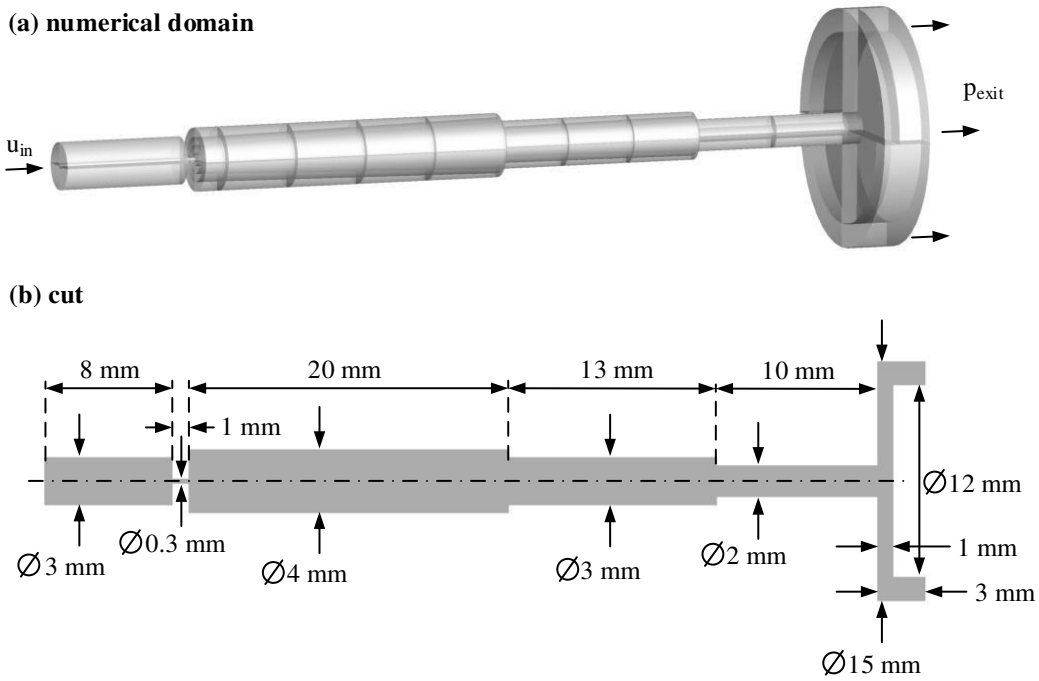

FIG. 7.7. Computational domain of case A. (a) Perspective view. (b) Cross-section.

Table XV: Parameters for calculations of case A.

inlet pressure [bar]	mass flow rate [kg/s]	outlet pressure [bar]	$\varepsilon_4(t=0)/\varepsilon_{g,tot}$ [%]	F [-]
75	$5.18 \cdot 10^{-3}$	2.3	0.832	1
75	$5.18 \cdot 10^{-3}$	2.8	0.1118	1
50	$4.24 \cdot 10^{-3}$	2.0	0.575	1
50	$4.24 \cdot 10^{-3}$	2.4	0.0719	1
25	$3.01 \cdot 10^{-3}$	1.7	0.131	1
25	$3.01 \cdot 10^{-3}$	2.1	0.00944	1
15	$2.27 \cdot 10^{-3}$	1.36	0.0988	1
15	$2.27 \cdot 10^{-3}$	1.66	0.00570	1

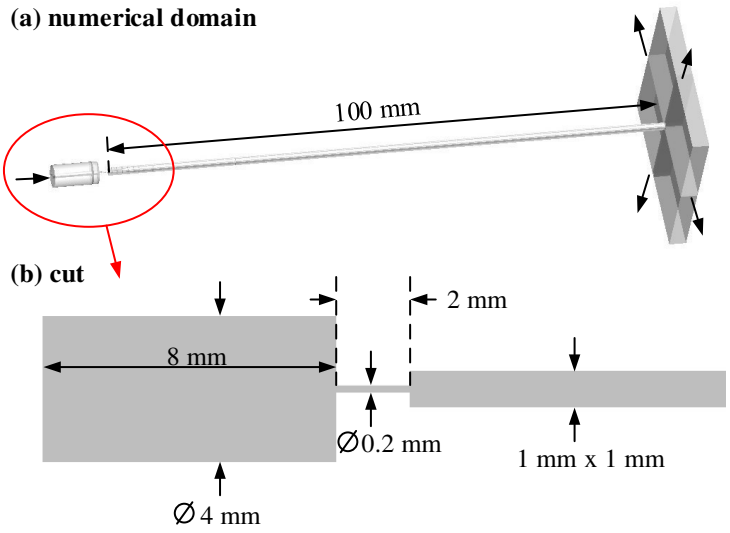

FIG. 7.8. Computational domain of case B. (a) Perspective view. (b) Cross-section.

Table XVI: Parameters for calculations of case B.

inlet pressure [bar]	mass flow rate [kg/s]	pressure at 500mm [bar]	outlet pressure [bar]	$\varepsilon_4(t=0)/\varepsilon_{g,tot}$ [%]	F [-]
75	$2.33 \cdot 10^{-3}$	2.7	3.67	5.83	5000
75	$2.33 \cdot 10^{-3}$	3.14	4.07	9.28	5000
75	$2.33 \cdot 10^{-3}$	3.57	4.5	0.773	1
75	$2.33 \cdot 10^{-3}$	4.03	4.95	0.398	1
50	$1.9 \cdot 10^{-3}$	1.8	2.59	5.84	5000
50	$1.9 \cdot 10^{-3}$	3.31	4.07	0.177	1
50	$1.9 \cdot 10^{-3}$	3.71	4.47	0.0445	1
25	$1.33 \cdot 10^{-3}$	2.01	2.58	0.0286	1
25	$1.33 \cdot 10^{-3}$	2.21	2.78	0.0259	1
15	$0.976 \cdot 10^{-3}$	1.48	1.91	0.0139	1
15	$0.976 \cdot 10^{-3}$	1.59	2.01	0.0108	1

In the experiment, the entire setup is initially filled with liquid and all gas is solved. Measurements are performed after a transient when a stable free gas content downstream of the nozzle has established. Numerical tests showed, that the time interval needed to establish this stable solution is much larger than the interval needed to perform the simulation of actual interest. To make computations more efficient, free gas content measured in the experiment is chosen as initial condition after the nozzle in the simulation, see FIG. 7.9. Initially, the velocity field is at rest and the static pressure is set to the pressure of the outlet boundary condition.

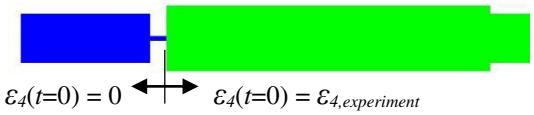

FIG. 7.9. Initial values of the free gas content $\varepsilon_4(t=0)$.

7.3 Results

The following section summarizes the numerical results. First flow dynamics are analyzed, then values of free gas predicted by the model are discussed and compared to experimental finding.

7.3.1 Flow Dynamics

FIG. 7.10 and FIG. 7.11 show snapshots of vapor and gas regions for different inlet pressures of cases A and case B respectively. For both setups, the nozzle is choked in all operating conditions, which results in a stable cavitation sheet covering the nozzle walls and extending over the entire nozzle length (supercavitation). Downstream of the nozzle, a cavitating shear layer develops at the jet boundary. In contrast to the nozzle flow, vapor structures in the shear layer are highly transient. The stream wise extent of the cavitating part of the shear layer depends on massflow rate and outlet pressures. Regions of high gas volume fraction are located in the vicinity of vapor structures due to the low static pressure. Gas is released in the sheet cavity in the nozzle and in the cavitating part of the shear layer, see FIG. 7.12. The liquid core passes the nozzle with all gas still solved.

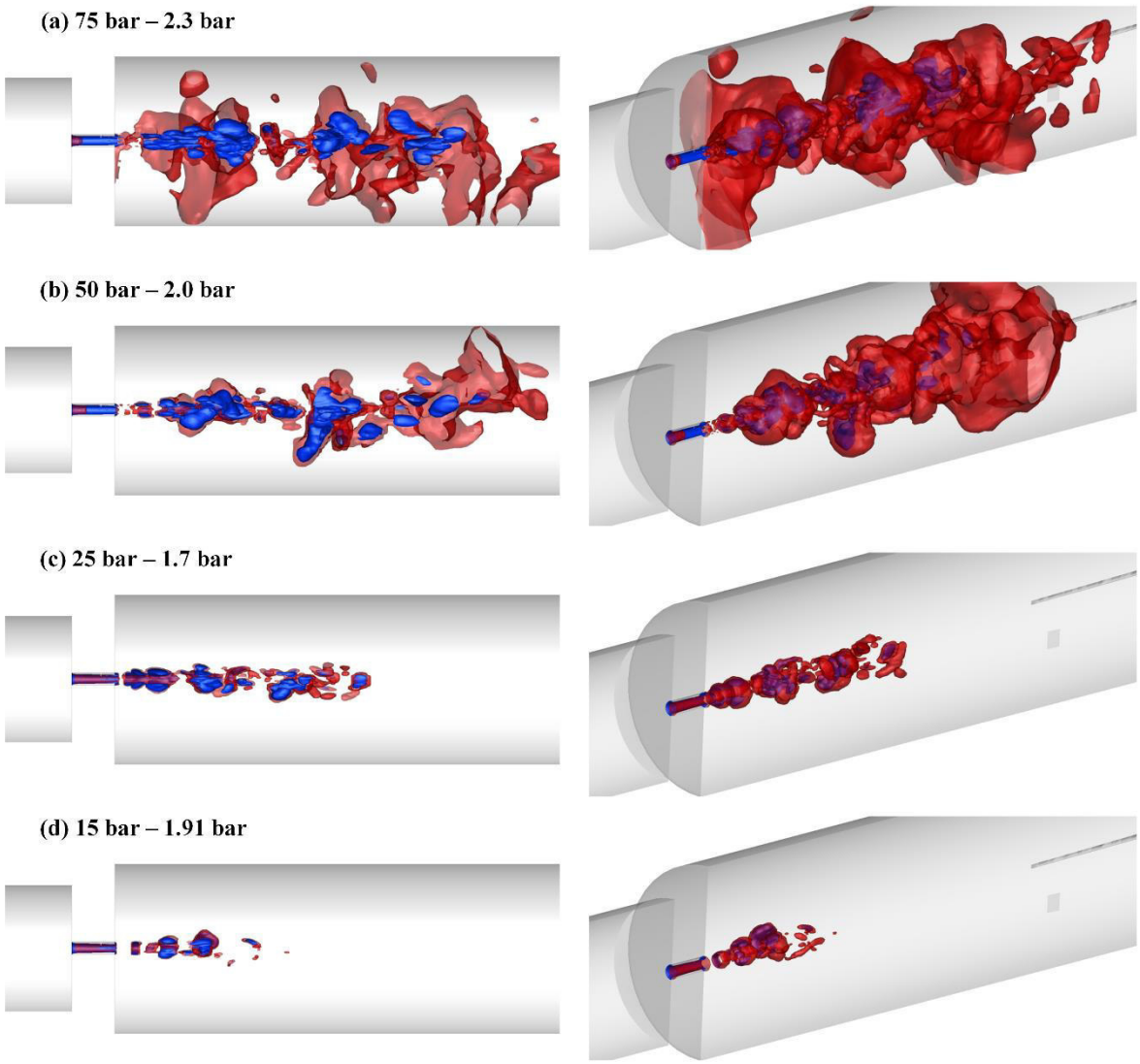

FIG. 7.10. Instantaneous vapor and gas structures of case A, F=1. Blue iso-surfaces show volume fraction vapor (α>0.1) and red iso-surfaces show volume fraction of free gas (β_4>0.001). (a) – (d): variation of operating conditions. Left: side view, front half of the channel is not shown. Right: perspective view.

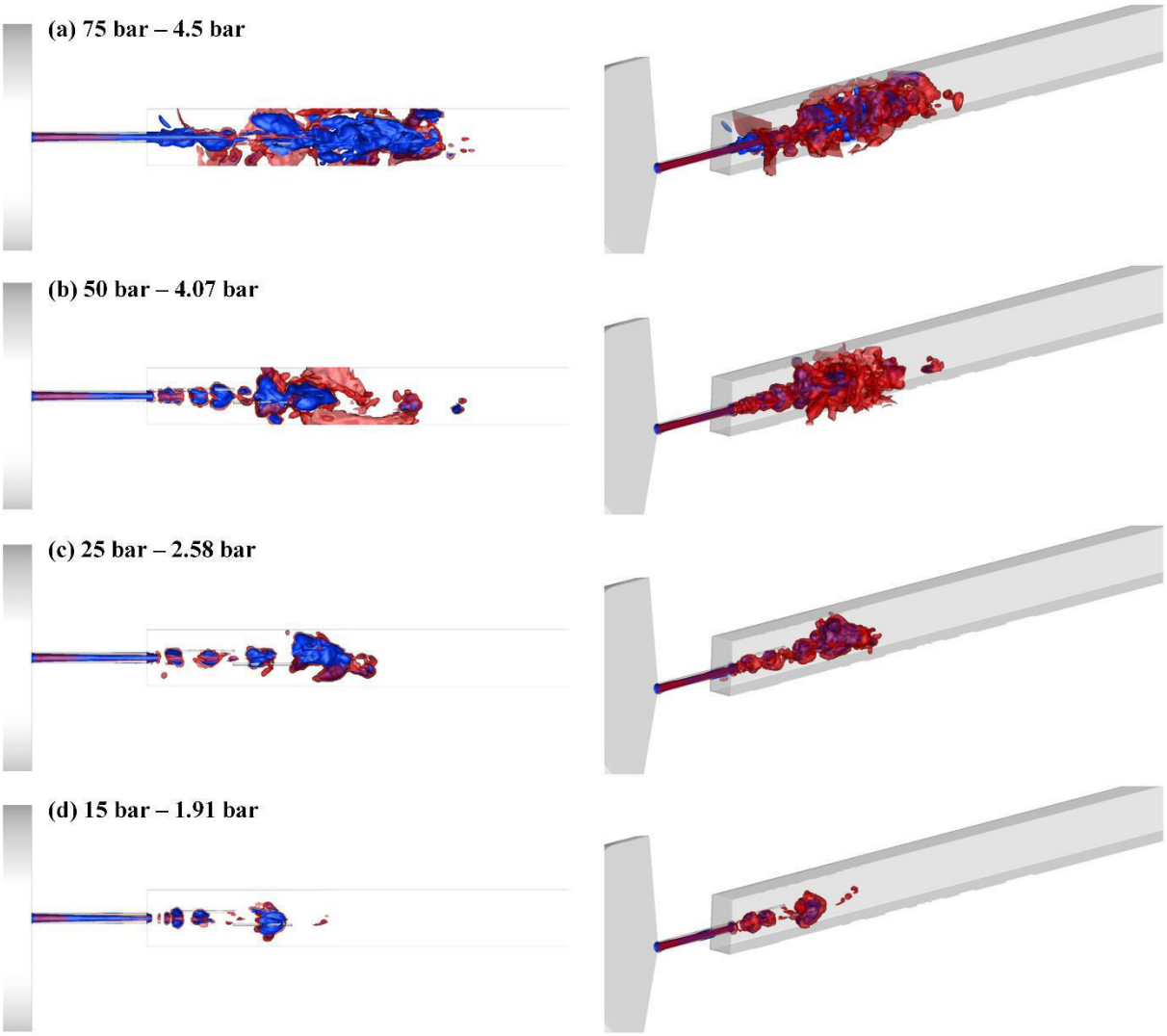

FIG. 7.11. Instantaneous vapor and gas structures of case B, F=1. Blue iso-surfaces show volume fraction vapor (α>0.1) and red iso-surfaces show volume fraction of free gas (β_4>0.001). (a) – (d): variation of operating conditions. Left: side view, front half of the channel is not shown. Right: perspective view.

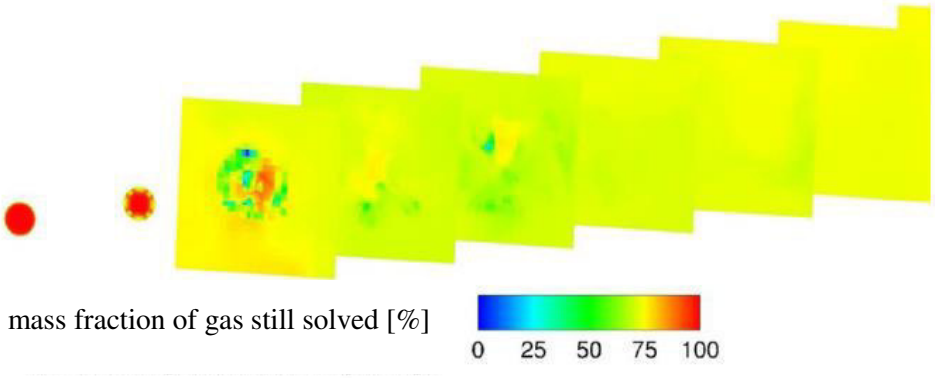

FIG. 7.12. Amount of gas still solved in the liquid in axial cut-planes. p_{in}=75 bar, p_{exit}=3.96 bar, F=5000.

7.3.2 Release of Solved Gas through Cavitation

In the experiment, the free gas content is determined optically. In the simulation, the mass of gas Δm_4, which is released by the model in each timestep Δt, is monitored as

$$\Delta \dot{m}_4 = \frac{\Delta m_4}{\Delta t} . \tag{7.12}$$

The mass fraction of free gas downstream of the nozzle x_4 then is the ratio of the temporal mean of $\Delta \dot{m}_4$ and the massflow through the system $\dot{m}$

$$\varepsilon_4 = \frac{\overline{\Delta \dot{m}_4}}{\dot{m}} . \tag{7.13}$$

7.3.3 Case B – F=1

Table XVII summarizes values of ε_4 downstream of the nozzle, FIG. 7.13 shows the influence of outlet pressure. The influence of the outlet pressure (slope in FIG. 7.13) is underestimated considerably compared to the experiment. For high outlet pressures the simulation agrees with estimates for ε_4 directly downstream of the nozzle in the experiment for 15bar, 25bar, and 50bar inlet pressure. All simulated operating conditions show a self-similar behavior in terms of $\sigma(p_{sat})$. This is a consequence of the coupling of release of solved gas and cavitation in the applied model.

Table XVII: Simulation results of case B.

inlet pressure [bar]	outlet pressure [bar]	F [-]	$\varepsilon_4/\varepsilon_{g,tot}$ [%]
75	4.5	1	0.411
75	4.95	1	0.362
50	4.07	1	0.239
50	4.47	1	0.209
25	2.58	1	0.140
25	2.78	1	0.121
15	1.91	1	0.0873
15	2.01	1	0.0800

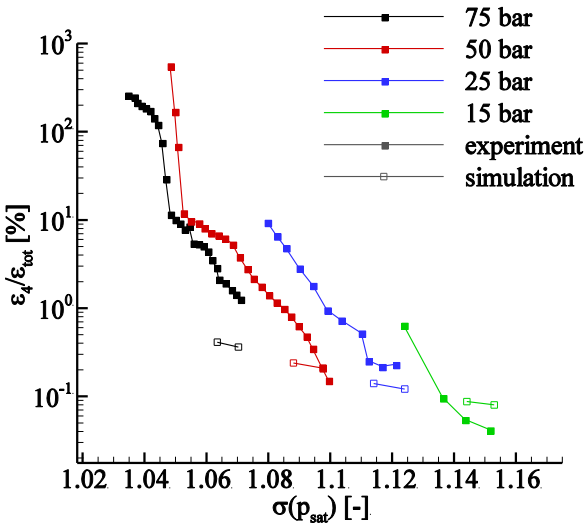

FIG. 7.13. Dimensionless free gas content $\varepsilon_4/\varepsilon_{g,tot}$ for case B as a function of the cavitation number $\sigma(p_{sat})$.

7.3.4 Case A – F=1

Table XVIII summarizes values of ε_4 downstream of the nozzle, FIG. 7.14 shows the influence of cavitation number $\sigma(p_{sat})$. Analogous to case B, the influence of the outlet pressure (slope in FIG. 7.14) is underestimated considerably compared to the experiment. In the experiment, the free gas content is measured 500 mm downstream of the nozzle and no estimate for the gas contend directly at the nozzle outlet is available. Thus, the simulation predicts higher values of ε_4 for the highest outlet pressures than the experiment. Again, due to the coupling of release of solved gas and cavitation, simulation results show self-similar behavior in terms of $\sigma(p_{sat})$.

Table XVIII: Simulation results of case A.

inlet pressure [bar]	outlet pressure [bar]	F [-]	$\varepsilon_4/\varepsilon_{g,tot}$ [%]
75	2.3	1	0.360
75	2.8	1	0.297
50	2.0	1	0.272
50	2.4	1	0.224
25	1.7	1	0.152
25	2.1	1	0.110
15	1.36	1	0.102
15	1.66	1	0.0812

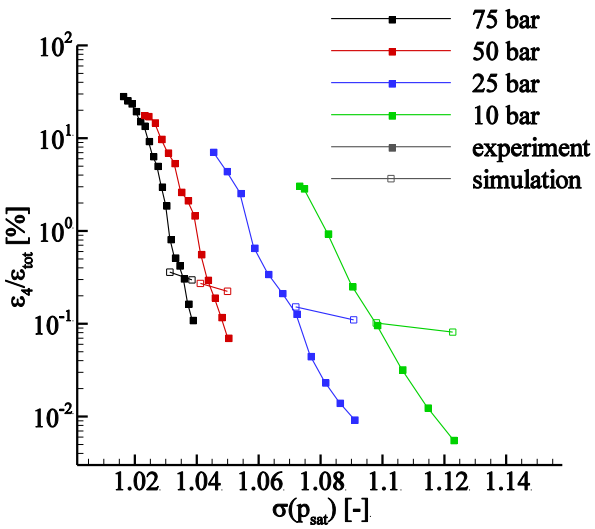

FIG. 7.14. Dimensionless free gas content $\varepsilon_4/\varepsilon_{g,tot}$ for case A depending on cavitation number $\sigma(p_{sat})$.

7.3.5 Case B – F = 5000

Table XIX summarizes values of ε_4 downstream of the nozzle, FIG. 7.15 shows the influence of outlet pressure for calculations with F=500 and F=1 from section 0. The three simulated operating conditions show that with a high value of F, large amounts of free gas ($\varepsilon_4/\varepsilon_{g,tot}$ >30%) can be generated. Although the modelling is not physically correct for $F\neq1$, a physical interpretation will be given in the following section.

Table XIX: Simulation results of case A, F=5000.

inlet pressure [bar]	outlet pressure [bar]	F [-]	$\varepsilon_4/\varepsilon_{g,tot}$ [%]
75	3.67	5000	36.7
75	4.07	5000	35.9
50	2.59	5000	34.1

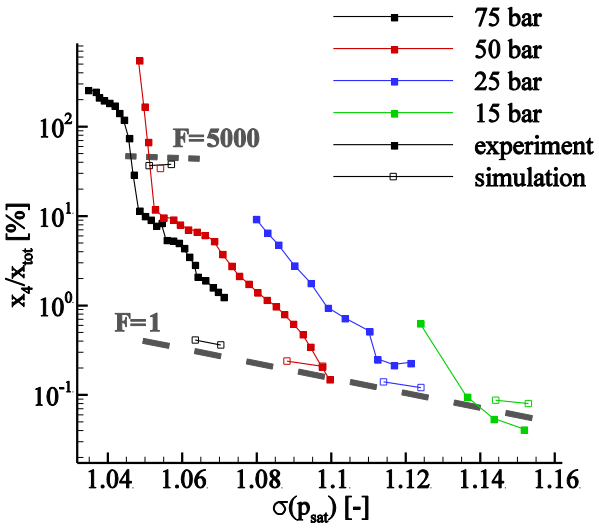

FIG. 7.15. Dimensionless free gas content $\varepsilon_4/\varepsilon_{g,tot}$ for case B depending on outlet pressure.

7.4 Discussion

Three physical processes that can change the free gas content, have been introduced in chapter 3.3.3.

(a) When a given volume of liquid is evaporated, the gas solved in that volume is released. This process is modeled in the simulation.

(b) Solved gas gets released from the liquid by diffusion at an interfacial area between liquid and gas or liquid and vapor, if the static pressure is lower than the saturation pressure of gas in the liquid (see Eq. 7.3).

(c) Free gas gets solved in the liquid by diffusion at an interfacial area between liquid and gas or liquid and vapor, if the static pressure is higher than the saturation pressure of gas in the liquid (see Eq. 7.3).

The domain can thus be divided into three regimes, see FIG. 7.16

1) cavitating nozzle flow: The static pressure is close to vapor pressure, thus process (c) does not occur. High average velocities and short characteristic length scales (nozzle length) result in short time scales. Interfacial area is mainly generated by the supercavitating sheet- cavity in the nozzle. Process (a) is dominant compared to process (b).

2) Cavitating part of the outlet: The static pressure is still close to vapor pressure. Low average velocities and bigger length scales lead to (compared to 1)) longer time scales. A large interfacial

area is generated by bubbly mixture of gas, vapor, and liquid. Process (b) is dominant compared to process (a).

3) Non-cavitating part of the outlet. The static pressure is assumed to be close to the outlet pressure, which is higher than saturation pressure. Low average velocities and bigger length scales (compared to 2)) lead to even longer time scales. Process (c) is dominant.

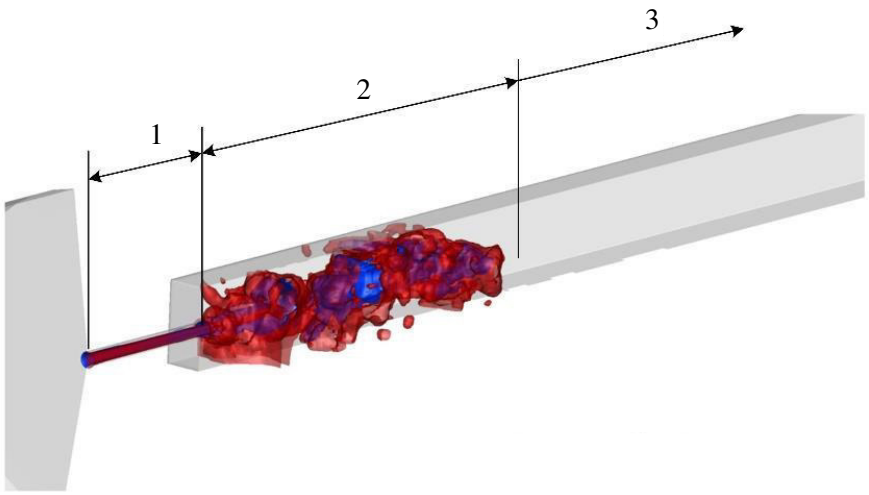

FIG. 7.16. Snapshot of case B, 75 bar – 4.5 bar, F=1. Blue iso-surfaces show volume fraction vapor (α>0.1) and red iso-surfaces show volume fraction of free gas (β_4>0.001). 1: Cavitating nozzle flow. 2: Cavitating part of the outlet. 3: Non-cavitating part of the outlet.

Case B

When the free gas content is determined downstream of the nozzle, process (c) always plays a role. For further discussion, we assume that the influence of process (c) is fully captured in the analytical estimation of section 7.1.1. For high outlet pressures and associated small amounts of vapor in the outlet region, regime 3) becomes small (process (b) insignificant) and process (a) is dominant. As only process (a) is modelled in the simulation, agreement with experiment is good only at high outlet pressures (FIG. 7.13). Decreasing the outlet pressure at constant inlet pressure leads to increased vapor generation in the outlet region and to a larger regime 2). Thus, process (b) becomes more dominant. As process (b) is not modelled, the influence of the outlet pressure (slope in FIG. 7.13) is not reproduced by the simulation.

Case A

The interpretation of case B applies to case A as well. As the gas content in the experiment is only measured at a single location, the influence of process (c) can however not be estimated quantitatively. Qualitatively, neglecting process (c) leads to an overestimation of the gas content at high outlet pressures compared to the experiment, as observed in FIG. 7.14.

Case B – F=5000

By choosing a high value for F, a high a large amount of gas gets generated as soon as liquid evaporates. This can be interpreted as upper estimate for the influence of process (b) in regions 1) and 2). However, it has to be emphasized, that the modelling is physically not correct, as no influence of concentration difference, time, and interfacial area is taken into account, see Eq. 7.1.

For low outlet pressures, high free gas contents ($\varepsilon_4/\varepsilon_{g,tot}$ >30%) are generated. This is the same order of magnitude as the highest gas contents measured in the experiment. The entire range of ε_4 measured in the experiment (O(0.1%) – O(10%)) can thus be represented as a combination of process (a) and (b). A correct modelling of process (b) should therefore enable the simulation to capture the influence of the outlet pressure more accurately. This, however, will require information about interfacial area, e.g. number-density distributions of bubbles in the simulation.

7.5 Conclusion

Degassing of a liquid can be strongly amplified by cavitation. Vapor liquid mixtures in hydrodynamic cavitation are characterized by a low static pressure (close to vapor pressure) and, in case of bubbly mixtures, a huge interfacial area. This favors degassing due to diffusion (process (b)). Additionally, solved gas is released when the liquid evaporates (process (a)).

The proposed gas model shows reasonable results for high exit pressures but fails to reproduce the experiment for lower exit pressures. In the investigated nozzle geometries a cavitating shear layer develops downstream of the nozzle in most of the investigated operating conditions. For lower exit pressures bigger parts of the regime directly downstream of the nozzle are occupied with reverse flow of gas-liquid-vapor mixtures. This is assumed to be the reason why the amount of free gas is dominated by diffusion for lower exit pressures. In geometries that do not promote large backflow regimes (e.g. the flow investigated in chapter 5), process (a) can be investigated more isolated. To do this, however, further experimental data is required.

8 Summary and Final Conclusion

Shocks and instantaneous pressure-peaks due to collapses of vapor clouds result in dynamic loads on material surfaces that may lead to material damage. The numerical simulation of these processes requires fully compressible modeling of the fluid and sufficient temporal resolution, which leads to time-steps of the order of nanoseconds. Provided that characteristic flow details (mean cavity length, shedding frequency, collapse positions, intensities, and rates) are reasonably predicted, the simulation already contains all necessary information about the erosive potential of the flow.

Grid-resolution studies show grid convergence for overall cavitation dynamics by comparison of flow topology, collapse characteristics, frequency spectra of time-dependent quantities, and location of collapse events. Agreement of the predicted dynamics with experiments is demonstrated by comparison of frequency spectra of experimental and numerical pressure sensors. Additionally, collapse locations in the simulation agree with erosion endangered areas in the experiment. This confirms that inertia drives the flow and motivates an inviscid flow model.

Although main cavitation structures are resolved, we find the expected generation of small scale cavitation structures with successive grid refinement as consequence of the inviscid model. A scaling law that removes resolution effects is proposed for the predicted rate of events. The scaling law contains the ratio of a characteristic length scale of the numerical grid, x_{char}, and a reference length scale $x_{ref,N}$. The latter introduces a limiting length scale for the fragmentation of vapor structures and is calibrated by comparing impact load spectra on experimental and corresponding numerical pressure sensors. With $x_{ref,N}$ calibrated and scaling law applied, the quantitative agreement between experimental and numerical pressure sensors demonstrates that realistic impact load spectra can be derived, even from coarsely resolved data. The calibrated value of $x_{ref,N}$ suggests that the limiting length scale for fragmentation is not connected to viscosity in the present case.

We introduce a numerical algorithm to detect single collapse events of isolated vapor structures (collapse detector). To remove resolution effects of the detected collapse pressure, we apply a second scaling law that contains the ratio of a characteristic length scale of the numerical grid, x_{char}, and a reference length scale $x_{ref,p}$. With both scaling laws applied, the analogy of numerically detected collapse rates and experimentally observed pitting rates shows that the application of the proposed collapse detector enables the extraction of reasonable erosion-related information from simulation data. While $x_{ref,p}$ can not be calibrated with the available experimental data, these analogies remain, as only the absolute pressure of a collapse event is affected by calibration, but not the rate of events.

For the investigated test case, we conclude that the erosive potential of the cavitating flow can be predicted with the applied method, provided that the spatial resolution can be chosen such that $x_{char} = x_{ref,N}$. With a coarser spatial resolution (i.e., $x_{char} > x_{ref,N}$) the erosive potential can still be estimated, given that the characteristic length scale $x_{ref,N}$ is known. In the presented case, $x_{ref,N}$ does not notably depend

on the operating condition, we assume, however, that it is not a universal quantity. Further investigations indicate that the proposed scaling laws apply to cavitation dynamics that are governed by a shedding instability, see Appendix 10.2 and Budich *et al.*[89]. The determination of the full range of validity and a calibration of $x_{ref,p}$ requires further experimental and numerical efforts.

When the erosive potential of the flow is known, resulting incubation times can be derived for different materials by application of the material model of Franc.[35] Values of predicted incubation times are within one order of magnitude compared to experimental findings. The proposed framework thus allows for a quantitative identification of potential erosion damage. Since in addition underlying dynamics of the flow are resolved, effective countermeasures can be developed already during the design process.

Including free and solved gas content in the physical model confirms a strong interaction of gas and cavitation. For the investigated nozzle geometries, this interaction is, however, dominated by diffusion, which gets enhanced by a significant increase of interfacial area provided by bubbles in low pressure backflow regimes downstream of the nozzle. This interaction might be less dominant in external flows that do not promote stable backflow regimes, but should be considered in the simulation of internal flows.

9 Outlook and Recommendations for Future Work

The presented work provides several starting points for future research.

9.1 Impact Load Spectrum, Scaling Laws, and Calibration of $x_{ref,p}$ and $x_{ref,N}$

In the context of erosion prediction, the load spectrum in the fluid domain has to be reduced to a load spectrum on a wall. There are, however, applications, where information about the collapse spectrum in the entire fluid domain is favorable. In chemical engineering high pressures and high temperatures in the late stage of a collapse are used to initiate chemical reactions or for decontamination of liquids, see Ref. 49 for an overview. In food science, cavitating nozzles are used for the homogenization of emulsions like milk.[90] In these applications, numerical simulation and possibly optimization of the collapse spectrum in the fluid domain could be a powerful tool.

In this work, two scaling laws for the collapse spectrum have been validated for cavitating flows which are dominated by a shedding mechanism. As it cannot be assumed that these laws apply to all forms of cavitation in general, further work is needed to investigate the scaling behavior. Due to its technical relevance, vortex cavitation in shear layers is one interesting example.

The value of $x_{ref,N}$ is interpreted as a limiting length scale for the fragmentation of vapor structures. The exact physical mechanism could not be identified reliably in this work. The next step in this direction should be to find a calibration of $x_{ref,N}$ for different setups where information about impact load spectra are available. Suitable experiments have been performed, e.g., by Steller[91] and Momma *et al.*[78] A possibility to assess the role of surface tension is to investigate a series of operating conditions with constant cavitation number similar to the axisymmetric flow in chapter 5, but over a bigger variation of system pressures. For very low system pressures, the influence of surface tension should generally increase.

To investigate the scaling behavior in general, additional information about the history of a collapsing vapor structure can be acquired by the collapse detector. This information should include the time history of the vapor volume of the structure, $\alpha(t)$, and information about fragmentation, i.e., if a fragment separates from the structure, or if two structures merge. With this information it should be possible to determine if there is possibly a range where fragmentation is self-similar. With this information available, it is possible to explain the observed scaling behavior.

As discussed before, spatially resolved information about the load spectrum is needed for calibration of $x_{ref,p}$. Spatially resolving a collapse-induced load is a demanding task in general due to limited sensor size. Regarding a pressure sensor with spatial resolution, promising developments have been reported by Dimitrov *et al.*[87] and Dimitrov.[92] A different approach is followed by Roy *et al.*[93,94] and Pöhl *et al.*,[95] who attempt to reconstruct the load on the wall by comparison of pitting tests and finite element computations of the material.

9.2 Numerical Prediction of Cavitation Erosion

The presented framework for numerical prediction of cavitation erosion has been validated for different operating conditions for a single setup and for different materials. Due to the limited available database, operating condition and material could not be varied independently. A next step should thus be to extend the experimental database, or to apply the proposed framework to a new configuration. Additionally, investigations of higher system pressures and different flow media are of interest. Suitable experiments of cavitating micro channels have been reported, e.g., in Refs. 23,96.

A second task is to improve the model itself. This can be achieved, e.g., by taking into account the temporal evolution and spatial distribution of a load, as well as material properties that account for high temporal strain rates. Some of these issues have recently been addressed in Ref. 36. Finally, the current model applies only for ductile materials which can undergo work hardening. Brittle materials or coatings need additional modelling considerations.

9.3 Interaction of Cavitation and Gas Content

In most of the investigated operation conditions, the free gas content was dominated by diffusion in the cavitating backflow region downstream of the nozzle. To separate the different physical processes influencing the gas content, a setup that does not promote large backflow regimes is of interest. To incorporate diffusion into the numerical model, information about the interfacial area needs to be available. This is the case for Euler-Lagrangian cavitation models, see, e.g., Refs. 18 and 16. Additionally, different gas and liquid combinations with different solvability can be investigated. Finally, investigating the influence of free gas content on cavitation erosion is another possible direction for future research.

10 Appendix

10.1 Definition of Cloud Setup

Table XX holds the coordinates of the center and the radius of each individual bubble of the cloud investigated in chapter 4.

Table XX: Bubble distribution of the cloud.

Nr.	x [mm]	y [mm]	z [mm]	radius [mm]
1	9.31013431	13.41981378	12.72457594	1.63624359
2	9.90428904	8.98685510	11.51941094	0.86392241
3	6.63869405	9.88268204	10.55752172	1.59665163
4	5.75660571	8.40636524	7.29754222	1.45149453
5	11.67094237	12.13077176	13.13413322	0.76363996
6	11.15937760	10.72685863	8.41538732	0.74734474
7	7.60691271	10.95296511	6.59357277	1.61891813
8	4.25215115	12.71961023	12.10785764	1.58355356
9	13.08692089	10.51215418	11.57488832	1.31877382
10	8.80500894	9.60062838	8.57763731	0.81658481
11	10.52094855	14.46107566	8.46126837	1.30779512
12	11.59689113	7.46184712	12.20537889	1.38059933
13	9.82484104	7.74703938	9.27449400	0.91108137
14	5.26915452	7.86243090	11.47930793	0.78295419
15	14.56235754	7.88199274	8.78220674	1.45480056
16	11.93244027	10.86922096	5.84527942	1.58622576
17	9.33278975	10.73245524	11.14358050	0.77326020
18	8.94661596	7.46244975	6.17584921	1.19994668
19	10.99278930	11.95661427	10.28629910	0.94090813
20	16.29699230	10.38693558	10.33113983	1.13221951
21	12.05795705	9.06569667	8.27027087	0.97219081
22	9.56700294	11.44851470	14.81455627	0.98881842
23	9.21805048	12.55611303	8.13031445	0.75895169
24	10.28855252	5.13298073	13.29711056	1.15175120
25	7.81880301	6.51833477	8.90288313	0.92471090
26	8.05349201	9.67676387	13.08943659	0.99477397
27	11.02406910	5.81731877	7.70883624	1.51791234
28	8.10442826	5.03762126	6.83178999	0.98190953
29	12.51692937	7.56374821	5.58375388	0.75963946
30	8.49232537	7.21603152	10.98148530	1.21299489
31	9.29033427	4.98865293	9.89135762	0.94351445
32	12.42228281	7.18675189	9.57690137	0.73018878
33	7.77193739	14.50179990	10.23322111	1.19076015
34	8.62042705	7.04300378	14.29099587	0.85417799
35	10.96342817	7.98651255	6.69125843	0.73570805
36	15.29406202	7.66222721	12.99384797	1.14983509

37	6.44823992	12.08008042	8.95344853	0.71685491
38	14.84250554	13.41349524	8.26374635	0.79586918
39	14.35584551	12.09980720	6.97742607	0.97857929
40	13.94764686	10.54009640	8.49810344	0.96520082
41	14.63822722	5.61838835	5.74427634	1.03191817
42	6.84198111	7.03592353	15.72777629	1.17446042
43	7.07152337	4.11771640	12.31624782	0.70003519
44	12.22314417	2.32647844	14.68216300	1.00540386
45	15.82805216	15.39419889	9.14686352	0.83747946
46	14.43739474	18.50965738	8.90984591	1.08955973
47	14.95811045	13.06576133	10.02714198	0.70266581
48	6.40103221	18.02918851	13.35858047	0.92340262
49	6.58143073	14.16336596	4.86743744	0.87460335
50	5.24163656	12.58844078	2.94701319	0.82284505
51	10.52259088	3.35671104	16.51577592	0.87618351
52	15.40614665	13.49713415	3.45033925	1.04709531
53	14.42838818	3.42929751	10.33699334	0.71990820
54	1.00000000	11.30655795	11.12899095	0.83889130
55	11.03804618	14.22180444	14.55417514	0.86622530
56	8.53875071	11.40412882	9.85513628	0.76916602
57	11.42908096	13.43859613	1.40939713	0.72283636
58	2.75798142	11.44274294	17.54000425	0.86712908
59	19.00000000	7.38112085	10.88032693	0.70404040
60	12.91621834	14.07285869	3.12370665	0.76416868
61	3.01231578	6.52472286	12.50667185	0.71702460
62	1.00000000	10.08858711	4.65656108	0.93204813
63	11.00793540	17.25340009	9.05875134	0.82249226
64	10.54038972	8.66032273	4.35942559	1.15747685
65	10.61536908	12.33314544	17.01141715	0.70022273
66	11.09957039	15.71916342	4.28448223	0.85187135
67	13.97931099	15.88187695	9.69623923	0.74180786
68	11.74188301	4.43603441	1.99261121	0.76769825
69	11.25144973	8.14318895	17.39794314	0.95786326
70	4.95016700	13.76514554	8.50065529	1.14425885
71	12.86271781	2.08203070	9.68411371	0.76103801
72	14.52448040	12.87130058	11.75089628	0.70001946
73	5.78978986	4.99575056	14.25952971	0.91752501
74	12.69941270	14.26664710	9.30704581	0.70026348
75	1.66619383	15.35844505	1.34156730	0.99213810
76	5.57390586	15.08757293	12.02566028	0.71830823
77	15.98615766	16.11878932	6.60873860	0.89080248
78	7.81918645	5.56066722	12.96621144	0.90656261
79	2.35681564	6.29713431	16.68343186	0.90517217
80	5.59671015	5.03735244	8.40270489	0.82554950
81	6.59490556	9.23319854	17.24433124	0.70943366
82	13.32131028	8.20498377	2.64400750	0.96998289

83	8.86733651	4.91820574	4.91983265	0.77418653
84	13.27520907	9.85700492	15.68616271	1.12370082
85	8.83802757	13.62333328	17.05017924	1.16181328
86	14.22148585	16.20279610	7.74425477	0.71015980
87	17.60858238	7.50436053	4.15093333	0.89057787
88	10.50474584	1.00000000	1.07845614	1.01749705
89	5.22505995	14.50506926	13.97064149	0.70487663
90	2.09040426	8.69434625	10.83302751	0.71867260
91	10.61215028	17.87552059	13.81361961	0.74971296
92	3.60741474	4.20346636	7.86536977	0.74635234
93	11.71016604	6.33366108	15.56469023	0.93851459
94	5.55429131	7.65306957	1.00000000	0.71055919
95	8.32713854	17.72238731	9.58098345	0.74214596
96	3.19776937	15.36933839	10.96886456	0.71495440
97	10.53402916	8.94071653	15.08698165	0.85931625
98	13.04857910	6.83587164	3.81938558	0.72192419
99	1.93857925	12.51589715	9.49064574	0.74167486
100	7.83385742	1.95111055	5.44895682	0.71295121
101	11.78686380	17.90877819	10.88891059	0.73562068
102	4.93859962	10.79142898	17.94124901	0.74647332
103	6.31795809	3.21921647	11.00095659	0.70008116
104	9.33284849	4.19000257	3.20127785	0.98068965
105	2.65723661	7.73414910	5.30286580	0.75122926
106	10.30622661	18.19087088	11.72634035	0.74420817
107	6.76426947	14.54792887	13.10603321	0.70908827
108	18.87753189	11.03863299	5.75415611	0.85449241
109	2.29801558	11.42986119	14.25291777	0.78324928
110	4.04103979	12.74582565	5.24062559	1.10207379
111	13.59753728	16.94645345	5.36551446	0.89581924
112	15.12925386	12.77415723	17.23383188	0.80393098
113	15.65906703	16.66221678	10.91535449	1.11359936
114	8.85167792	15.34955919	6.84117064	0.78032055
115	1.00000000	3.71516120	9.25342798	0.96240997
116	7.66479045	11.14801943	17.23318636	0.83362750
117	13.65145147	3.39625150	12.21048713	1.02534003
118	15.53988874	13.65817189	13.26854348	0.71511840
119	12.44308949	12.73986101	14.66904461	0.74249569
120	4.85784747	14.06344831	3.92521873	0.71245624
121	5.36775917	12.36337602	6.80721670	0.70014291
122	9.54191163	10.82206503	3.38208077	0.74801871
123	17.80179739	1.73631437	2.83873376	1.03901250
124	11.23703927	15.91128588	10.58584958	0.74580700
125	1.91928118	13.09908271	16.37882054	0.75122918

10.2 Scaling Behavior of Impact Load Spectra

The setup is a planar nozzle flow as shown in FIG. 10.1. The stagnation pressure before the nozzle is 300 bar. Two different static outlet pressures are investigated: 55 bar and 115 bar. The working fluid is diesel.

FIG. 10.2 shows load spectra of the collapse detector. When scaling is applied, spectra of different spatial resolutions collapse for both operating conditions.

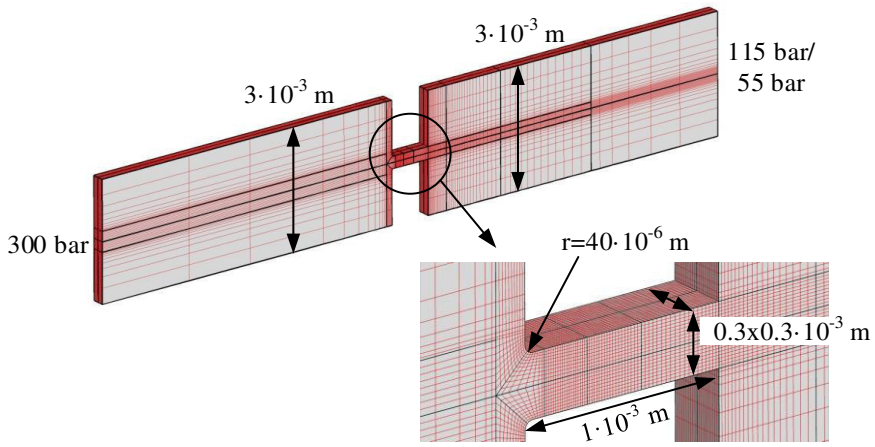

FIG. 10.1. Numerical setup.

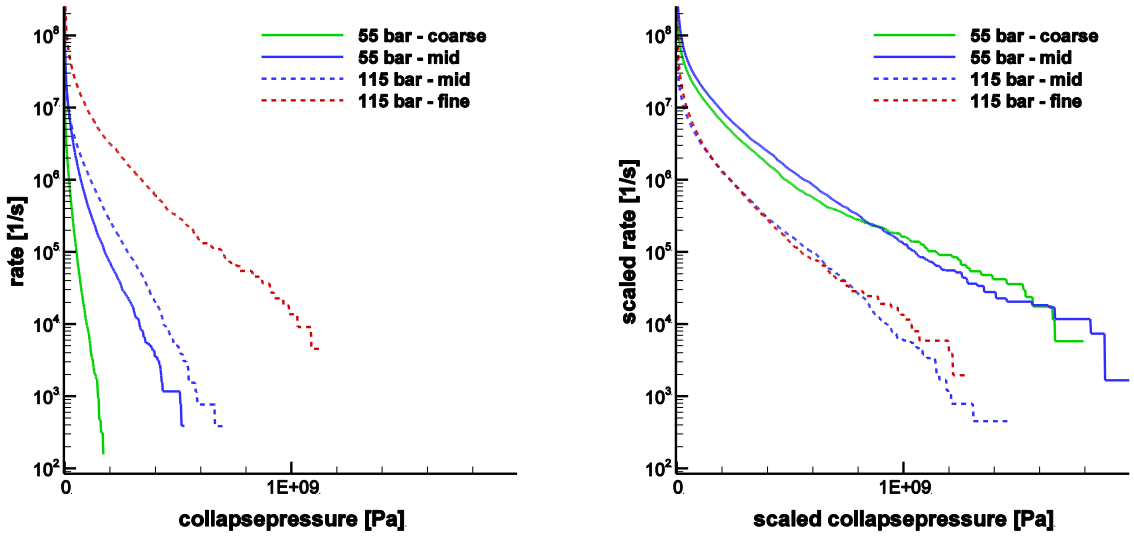

FIG. 10.2. Cumulative rate of collapse events determined by the collapse detector. Left: no scaling. Right: pressure and rate of events scaled. $x_{ref,N} = x_{ref,p} = 3.5\text{x}10^{-6}$ m (arbitrary chosen).

11 References

[1] Brennen, C. E. (2013). *Cavitation and bubble dynamics*, Cambridge University Press.

[2] Franc, J.-P. and J.-M. Michel (2006). *Fundamentals of cavitation*, Springer.

[3] Arndt, R. E. (1981). "Cavitation in fluid machinery and hydraulic structures." *Annual Review of Fluid Mechanics* **13**(1): 273-326.

[4] Brennen, C. E. (1994). *Hydrodynamics of Pumps* Concepts ETI Inc.

[5] Arndt, R. E. (2002). "Cavitation in vortical flows." *Annual Review of Fluid Mechanics* **34**(1): 143-175.

[6] Iyer, C. O. and S. L. Ceccio (2002). "The influence of developed cavitation on the flow of a turbulent shear layer." *Physics of Fluids (1994-present)* **14**(10): 3414-3431.

[7] O'Hern, T. J. (1990). "An experimental investigation of turbulent shear flow cavitation." *Journal of Fluid Mechanics* **215**: 365-391.

[8] Franc, J.-P., M. Riondet, A. Karimi and G. L. Chahine (2011). "Impact Load Measurements in an Erosive Cavitating Flow." *Journal of Fluids Engineering* **133**(12): 121301-121301.

[9] Jayaprakash, A., J.-K. Choi, G. L. Chahine, F. Martin, M. Donnelly, J.-P. Franc and A. Karimi (2012). "Scaling study of cavitation pitting from cavitating jets and ultrasonic horns." *Wear* **296**(1): 619-629.

[10] Hattori, S., T. Hirose and K. Sugiyama (2010). "Prediction method for cavitation erosion based on measurement of bubble collapse impact loads." *Wear* **269**(7–8): 507-514.

[11] PHILIPP, A. and W. LAUTERBORN (1998). "Cavitation erosion by single laser-produced bubbles." *Journal of Fluid Mechanics* **361**: 75-116.

[12] Tinguely, M., D. Obreschkow, P. Kobel, N. Dorsaz, A. De Bosset and M. Farhat (2012). "Energy partition at the collapse of spherical cavitation bubbles." *Physical Review E* **86**(4): 046315.

[13] Delale, C. F. (2012). *Bubble Dynamics and Shock Waves*, Springer.

[14] Bensow, R. E. and G. Bark (2010). "Simulating cavitating flows with LES in openfoam". *5th European Conference on Computational Fluid Dynamics*, Lisbon, Portugal.

[15] Bensow, R. E. and G. Bark (2010). "Implicit LES Predictions of the Cavitating Flow on a Propeller." *Journal of Fluids Engineering* **132**(4): 041302-041302.

[16] Yakubov, S., B. Cankurt, M. Abdel-Maksoud and T. Rung (2013). "Hybrid MPI/OpenMP parallelization of an Euler–Lagrange approach to cavitation modelling." *Computers & Fluids* **80**(0): 365-371.

[17] ANDRIOTIS, A., M. GAVAISES and C. ARCOUMANIS (2008). "Vortex flow and cavitation in diesel injector nozzles." *Journal of Fluid Mechanics* **610**: 195-215.

[18] GIANNADAKIS, E., M. GAVAISES and C. ARCOUMANIS (2008). "Modelling of cavitation in diesel injector nozzles." *Journal of Fluid Mechanics* **616**: 153-193.

[19] Schmidt, S. J., I. H. Sezal and G. H. Schnerr (2006). "Compressible simulation of high-speed hydrodynamics with phase change". *ECCOMAS CFD 2006: Proceedings of the European Conference on Computational Fluid Dynamics*, Egmond aan Zee, The Netherlands, Delft University of Technology; European Community on Computational Methods in Applied Sciences (ECCOMAS).

[20] Schnerr, G. H., I. H. Sezal and S. J. Schmidt (2008). "Numerical investigation of three-dimensional cloud cavitation with special emphasis on collapse induced shock dynamics." *Physics of Fluids (1994-present)* **20**(4): 040703.

[21] Schmidt, S., G. Schnerr and M. Thalhamer (2009). "Inertia controlled instability and small scale structures of sheet and cloud cavitation". *Proc. of the 7th International Symposium on Cavitation*, Ann Arbor, Michigan, USA, Curran Associates Inc.

[22] Schmidt, S., I. Sezal, G. Schnerr and T. Matthias (2008). "Riemann Techniques for the Simulation of Compressible Liquid Flows with Phase-Transistion at all Mach Numbers - Shock and Wave Dynamics in Cavitating 3-D Micro and Macro Systems". *46th AIAA Aerospace Sciences Meeting and Exhibit*, Reno, Nevada, USA, American Institute of Aeronautics and Astronautics.

[23] Skoda, R., U. Iben, A. Morozov, M. Mihatsch, S. J. Schmidt and N. A. Adams (2011). "Numerical simulation of collapse induced shock dynamics for the prediction of the geometry, pressure and temperature impact on the cavitation erosion in micro channels". *Warwick WIMRC 3rd International Cavitation Forum*, Warwick, UK.

[24] Boorsma, A. and S. Whitworth (2011). "Understanding the Details of Cavitation". *Second International Symposium on Marine Propulsors*, Hamburg, Germany.

[25] Gavaises, M. (2008). "Flow in valve covered orifice nozzles with cylindrical and tapered holes and link to cavitation erosion and engine exhaust emissions." *International Journal of Engine Research* **9**(6): 435-447.

[26] Kjeldsen, M. and R. Arndt (2009). "Blade load dynamics in cavitating and two phase flows". *Proceedings of the 7th International Symposium on Cavitation - CAV2009*, Ann Arbor, Michigan, USA, Curran Associates Inc.

[27] Brandner, P., Y. Lecoffre and G. Walker (2007). "Design considerations in the development of a modern cavitation tunnel". *16th Australasian Fluid Mechanics Conference*, Crown Plaza, Gold Coast, Australia.

[28] Brandner, P. and G. Walker (2001). "A waterjet test loop for the Tom Fink cavitation tunnel". *International Conference on Waterjet Propulsion III,* , Royal Institution of Naval Architects, Gothenburg, Sweden.

[29] Battistoni, M., D. J. Duke, A. B. Swantek, F. Z. Tilocco, C. F. Powell and S. Som (2015). "EFFECTS OF NONCONDENSABLE GAS ON CAVITATING NOZZLES." *Atomization and Sprays* **25**(6).

[30] Iben, U., F. Wolf, H.-A. Freudigmann and W. H. J. Fröhlich (2014). "Optical measurements of gas bubbles in oil behind a cavitating micro-orifice flow." *Experiments in Fluids* **56.6**: 1-10.

[31] Freudigmann, H., U. Iben and P. Pelz (2015). "Air release measurements of V-oil 1404 downstream of a micro orifice at choked flow conditions". *Journal of Physics: Conference Series*, IOP Publishing.

[32] Van Terwisga, T., P. Fitzsimmons, Z.-r. Li and E. J. Foeth (2009). "Cavitation erosion—a review of physical mechanisms and erosion risk models". *Proc. 7th Int. Sym. Cavitation, CAV2009*, Ann Arbor, Michigan, USA.

[33] Karimi, A. and W. Leo (1987). "Phenomenological model for cavitation erosion rate computation." *Materials Science and Engineering* **95**: 1-14.

[34] Berchiche, N., J.-P. Franc and J.-M. Michel (2002). "A cavitation erosion model for ductile materials." *Journal of Fluids Engineering* **124**(3): 601-606.

[35] Franc, J.-P. (2009). "Incubation Time and Cavitation Erosion Rate of Work-Hardening Materials." *Journal of Fluids Engineering* **131**(2): 021303.

[36] Kim, K.-H., G. Chahine, J.-P. Franc and A. Karimi (2014). *Advanced Experimental and Numerical Techniques for Cavitation Erosion Prediction*, Springer.

[37] Mihatsch, M. S., S. J. Schmidt and N. A. Adams (2015). "Cavitation erosion prediction based on analysis of flow dynamics and impact load spectra." *Physics of Fluids (1994-present)* **27**(10): 103302.

[38] Brennen, C. E. (2011). "An introduction to cavitation fundamentals". *Warwick WIMRC 3rd International Cavitation Forum*, Warwick, UK.

[39] Tong, R., W. Schiffers, S. Shaw, J. Blake and D. Emmony (1999). "The role of 'splashing'in the collapse of a laser-generated cavity near a rigid boundary." *Journal of Fluid Mechanics* **380**: 339-361.

[40] JOHNSEN, E. and T. COLONIUS (2009). "Numerical simulations of non-spherical bubble collapse." *Journal of Fluid Mechanics* **629**: 231-262.

[41] Lauer, E., X. Y. Hu, S. Hickel and N. A. Adams (2012). "Numerical investigation of collapsing cavity arrays." *Physics of Fluids (1994-present)* **24**(5): 052104.

[42] Franc, J. and J. Michel (1985). "Attached cavitation and the boundary layer: experimental investigation and numerical treatment." *Journal of Fluid Mechanics* **154**: 63-90.

[43] Le, Q., J. P. Franc and J. M. Michel (1993). "Partial Cavities: Global Behavior and Mean Pressure Distribution." *Journal of Fluids Engineering* **115**(2): 243-248.

[44] Sezal, I. H. (2009) "Compressible dynamics of cavitating 3-D multi-phase flows." Dissertation, Lehrstuhl für Aerodynamik, Technische Universität München, Munich.

[45] Steller, J., A. Krella, J. Koronowicz and W. Janicki (2005). "Towards quantitative assessment of material resistance to cavitation erosion." *Wear* **258**(1–4): 604-613.

[46] Patella, R. F., J.-L. Reboud and A. Archer (2000). "Cavitation damage measurement by 3D laser profilometry." *Wear* **246**(1–2): 59-67.

[47] Hattori, S. and E. Nakao (2001). "Cavitation erosion mechanisms and quantitative evaluation based on erosion particles." *Wear* **249**(10–11): 839-845.

[48] Asi, O. (2006). "Failure of a diesel engine injector nozzle by cavitation damage." *Engineering Failure Analysis* **13**(7): 1126-1133.

[49] Shah, Y. T., A. Pandit and V. Moholkar (1999). *Cavitation reaction engineering*, Springer.

[50] Brennen, C. E. (2006). "A Review of Cavitation Uses and Problems in Medicine". *WIMRC Forum*, Warwick, UK, International Manufacturing Centre of the University of Warwick.

[51] Coussios, C. C. and R. A. Roy (2008). "Applications of acoustics and cavitation to noninvasive therapy and drug delivery." *Annual Review of Fluid Mechanics* **40**: 395-420.

[52] Ohl, C.-D., M. Arora, R. Dijkink, V. Janve and D. Lohse (2006). "Surface cleaning from laser-induced cavitation bubbles." *Applied Physics Letters* **89**(7): 074102.

[53] Song, W., M. Hong, B. Lukyanchuk and T. Chong (2004). "Laser-induced cavitation bubbles for cleaning of solid surfaces." *Journal of applied physics* **95**(6): 2952-2956.

[54] Dumouchel, C., N. Leboucher and D. Lisiecki (2013). "Cavitation and primary atomization in real injectors at low injection pressure condition." *Experiments in Fluids* **54**(6): 1-17.

[55] Sou, A., S. Hosokawa and A. Tomiyama (2010). "CAVITATION IN NOZZLES OF PLAIN ORIFICE ATOMIZERSWITH VARIOUS LENGTH-TO-DIAMETER RATIOS." *Atomization and Sprays* **20**(6): 513-524.

[56] Payri, F., V. Bermúdez, R. Payri and F. J. Salvador (2004). "The influence of cavitation on the internal flow and the spray characteristics in diesel injection nozzles." *Fuel* **83**(4–5): 419-431.

[57] Warnock, J. E. (1947). "Cavitation in Hydraulic Structures: A Symposium: Experiences of the Bureau of Reclamation." *Transactions of the American Society of Civil Engineers* **112**(1).

[58] Wrona, F. (2005) "Simulation von kavitierenden Strömungen in Hochdrucksystemen." Dissertation, Institut fur Aerodynamik und Gasdynamik, Universität Stuttgart,

[59] Tomita, Y. and A. Shima (1986). "Mechanisms of impulsive pressure generation and damage pit formation by bubble collapse." *Journal of Fluid Mechanics* **169**: 535-564.

[60] Okada, T., Y. Iwai, H. Ishimaru and N. Maekawa (1994). "Measurement and Evaluation of Cavitation Bubble Collapse Pressures." *JSME international journal. Ser. A, Mechanics and material engineering* **37**(1): 37-42.

[61] Endo, K., T. Okada and Y. Baba (1969). "Fundamental Studies on Cavitation Erosion." *Bulletin of JSME* **12**(52): 729-737.

[62] Toro, E. F. (2009). *Riemann solvers and numerical methods for fluid dynamics: a practical introduction*, Springer Science & Business Media.

[63] Koren, B. (1993). *A robust upwind discretization method for advection, diffusion and source terms*, Centrum voor Wiskunde en Informatica Amsterdam.

[64] Egerer, C. P., S. Hickel, S. J. Schmidt and N. A. Adams (2014). "Large-eddy simulation of turbulent cavitating flow in a micro channel." *Physics of Fluids (1994-present)* **26**(8): 085102.

[65] Saurel, R., P. Cocchi and P. B. Butler (1999). "Numerical study of cavitation in the wake of a hypervelocity underwater projectile." *Journal of Propulsion and power* **15**(4): 513-522.

[66] Schmidt, E. and U. Grigull (1989). *Properties of water and steam in SI-units 4 enlarged ed.*, Springer.

[67] The International Association for the Properties of Water and Steam (IAPWS), http://www.iapws.org/.

[68] Mihatsch, M. (2010) "Numerische Simulation kompressibler kavitierender Strömungen mit barotropen und nicht-barotropen thermodynamischen Modellen." Semesterarbeit, Lehrstuhl für Aerodynamik, Technische Universität München, München.

[69] Verein Deutscher Ingenieure (VDI-GVC) (2002), "VDI-Wärmeatlas: Berechnungsblätter für den Wärmeübergang," Springer.

[70] Mihatsch, M. (2010) "Numerische Simulation kavitierender Strömungen sowie Entwicklung und Bewertung strömungsmechanischer Erosionsindikatoren." Diplomarbeit, Lehrstuhl für Aerodynamik, Technische Universität München, München.

[71] Adams, N. A. and S. J. Schmidt (2013). "Shocks in cavitating flows". In *Bubble Dynamics and Shock Waves*, Springer**:** 235-256.

[72] Mihatsch, M. S., S. J. Schmidt, M. Thalhamer and N. A. Adams (2013). "Numerical prediction of erosive collapse events in unsteady compressible cavitating flows". In *MARINE 2011, IV International Conference on Computational Methods in Marine Engineering*, Springer**:** 187-198.

[73] Schmidt, S. J., M. S. Mihatsch, M. Thalhamer and N. A. Adams (2014). "Assessment of erosion sensitive areas via compressible simulation of unsteady cavitating flows". In *Advanced Experimental and Numerical Techniques for Cavitation Erosion Prediction*, Springer**:** 329-344.

[74] Mihatsch, M., S. J. Schmidt, M. Thalhamer, N. A. Adams, R. Skoda and U. Iben (2011). "Collapse Detection in Compressible 3-D Cavitating Flows and Assessment of Erosion Criteria". *WIMRC 3rd International Cavitation Forum*, Warwick, UK.

[75] Mihatsch, M. S., S. J. Schmidt, M. Thalhamer and N. A. Adams (2012). "Quantitative Prediction of Erosion Aggressiveness through numerical Simulation of 3-D Unsteady Cavitating Flows". *Proc. of the 8th International Symposium on Cavitation*, Singapore.

[76] Gavaises, M., F. Villa, P. Koukouvinis, M. Marengo and J.-P. Franc (2015). "Visualisation and les simulation of cavitation cloud formation and collapse in an axisymmetric geometry." *International Journal of Multiphase Flow* **68**: 14-26.

[77] Lee, M., S. Hong, G. Kim, K. Kim, C. Rhee and W. Kim (2006). "Numerical correlation of the cavitation bubble collapse load and frequency with the pitting damage of flame quenched Cu–9Al–4.5 Ni–4.5 Fe alloy." *Materials Science and Engineering: A* **425**(1): 15-21.

[78] Momma, T. and A. Lichtarowicz (1995). "A study of pressures and erosion produced by collapsing cavitation." *Wear* **186**: 425-436.

[79] Franc, J.-P., M. Riondet, A. Karimi and G. L. Chahine (2012). "Material and velocity effects on cavitation erosion pitting." *Wear* **274**: 248-259.

[80] Ghasempour, F., R. Andersson and B. Andersson (2014). "Multidimensional turbulence spectra–Statistical analysis of turbulent vortices." *Applied Mathematical Modelling* **38**(17): 4226-4237.

[81] Hibiki, T. and M. Ishii (2000). "One-group interfacial area transport of bubbly flows in vertical round tubes." *International Journal of Heat and Mass Transfer* **43**(15): 2711-2726.

[82] Ghasempour, F., R. Andersson, B. Andersson and D. J. Bergstrom (2014). "Number density of turbulent vortices in the entire energy spectrum." *AIChE Journal* **60**(11): 3989-3995.

[83] Higuera, F. (2004). "Axisymmetric inviscid interaction of a bubble and a vortex ring." *Physics of Fluids (1994-present)* **16**(4): 1156-1159.

[84] Pope, S. B. (2000). *Turbulent flows*, Cambridge university press.

[85] Kalpakjian, S., S. R. Schmid and E. Werner (2011). *Werkstofftechnik*, Pearson Deutschland GmbH.

[86] J.-P. Franc, personal communication (2013).

[87] Dimitrov, M., P. Pelz, A. Lyashenko, A. Tehrani and E. Dörsam (2014). "Measurement system by printed thin pressure sensor array". *9th International Fluid Power Conferenc*, Aachen, Germany, IFK, Aachen.

[88] Cussler, E. L. (2009). *Diffusion: mass transfer in fluid systems*, Cambridge university press.

[89] Bernd Budich, Steffen J. Schmidt and N. A. Adams (2015). "Numerical Simulation of Cavitating Ship Propeller Flow and Assessment of Erosion Aggressiveness". *VI International Conference on Computational Methods in Marine Engineering, MARINE 2015*, Rome, Italy.

[90] Innings, F., E. Hultman, F. Forsberg and B. Prakash (2011). "Understanding and analysis of wear in homogenizers for processing liquid food." *Wear* **271**(9): 2588-2598.

[91] Steller, J. (1999). "International cavitation erosion test and quantitative assessment of material resistance to cavitation." *Wear* **233**: 51-64.

[92] Dimitrov, M. (2014). *Räumlich auflösende, dynamische Druckmesssysteme mit piezoelektrischen Foliensensoren*, Shaker.

[93] Roy, S. C., J.-P. Franc, C. Pellone and M. Fivel (2015). "Determination of cavitation load spectra–Part 1: Static finite element approach." *Wear* **344**: 110-119.

[94] Roy, S. C., J.-P. Franc, N. Ranc and M. Fivel (2015). "Determination of cavitation load spectra—Part 2: Dynamic finite element approach." *Wear* **344**: 120-129.

[95] Pöhl, F., S. Mottyll, R. Skoda and S. Huth (2015). "Evaluation of cavitation-induced pressure loads applied to material surfaces by finite-element-assisted pit analysis and numerical investigation of the elasto-plastic deformation of metallic materials." *Wear* **330-331**: 618–628.

[96] Žun, I., M. Perpar, B. Stražišar, E. Polutnik, M. Pečar, Z. Rek and D. Beader (2005). *PREVERO.: Experimental and CFD technology for PREventive reduction of diesel engine emissions caused by cavitation EROsion: confidential final technical report*, University of Ljubljana, Faculty of Mechanical Engineering, Laboratory for Fluid Dynamics and Thermodynamics.